Performance Evaluation of a MEMS-based Low-Pressure Micro-Resistojet (LPM)

Gabriel Alves Teixeira

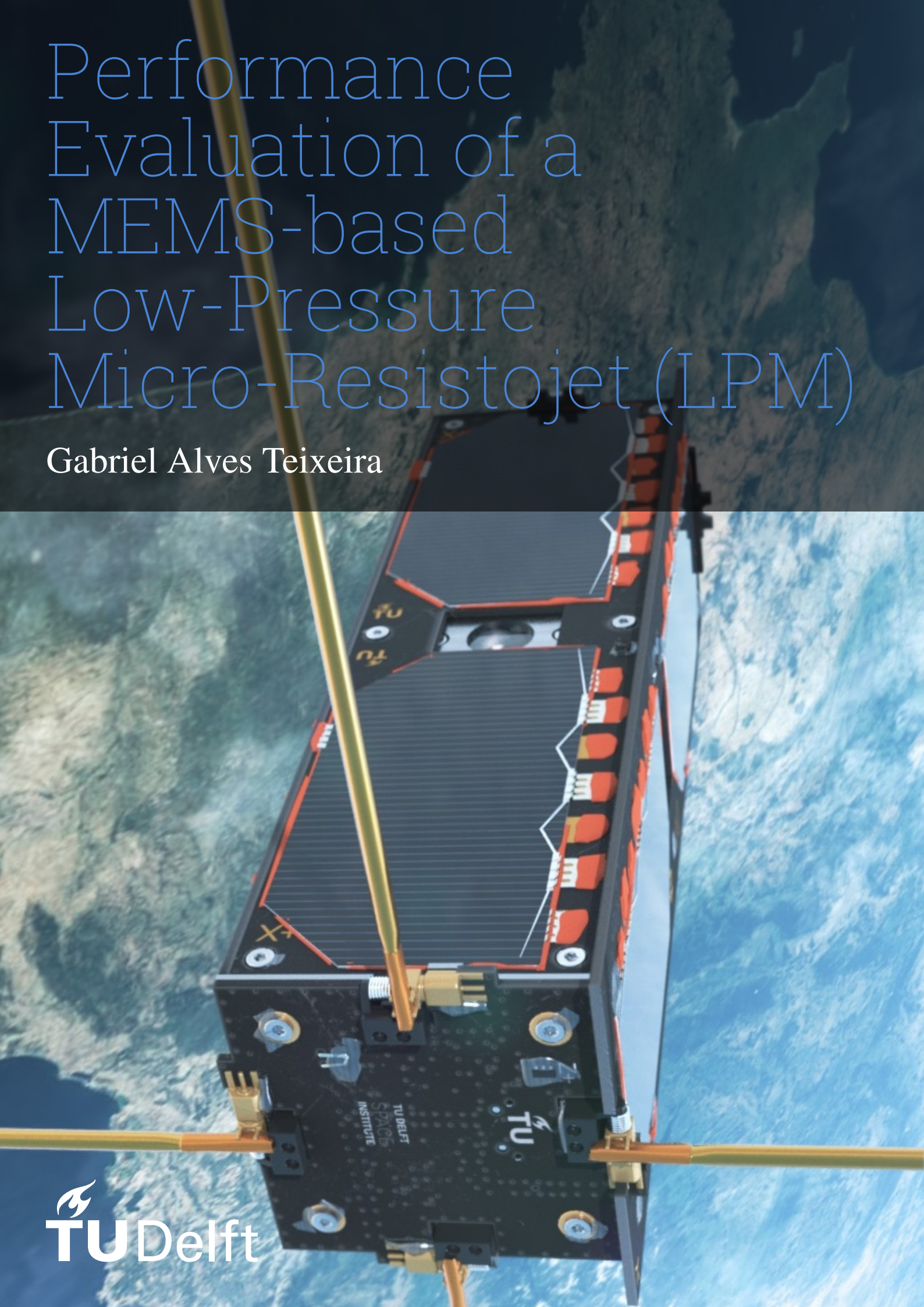

TU Delft

Performance Evaluation of a MEMS-based Low-Pressure Micro-Resistojet (LPM)

by

Gabriel Alves Teixeira

to obtain the degree of Master of Science

at the Delft University of Technology,

to be defended publicly on 12^{th} December, 2024 at 13:30.

Student number:	4820592	
Project duration:	February 14, 2024 – December 12, 2024	
Thesis committee:	Dr. A. Cervone,	TU Delft, Supervisor
	Dr. A. Menicucci,	TU Delft, Chair
	Ir. J. A. Melkert,	TU Delft, Independent Examiner
	Dr. ing. H.W. van Zeijl,	TU Delft, External Examiner

Cover: DelfiPQ by TU Delft

TU Delft

Preface

This report officially concludes my six years of studies at the Aerospace Engineering Faculty at the TU Delft. After nine months of intense, hard work, I am proud to present this report as my final Space Engineering MSc assignment. This was by far one of the most challenging projects, if not the most, that I have been a part of in my life. Regardless, if I could go back in time, I would undoubtedly chose the same project again. After almost five years of learning the theoretical principles, this practical project allowed my to learn everything I was missing to start a career in the field of designing, assembling and testing propulsion systems, and it also reminded me why I wanted to become an aerospace engineer in the first place.

It is assumed that the reader possesses basic electrical engineering knowledge, as well as space propulsion concepts, especially with regards to miniaturised systems. For the reader interested in 3D CAD modelling, 3D printing and prototyping, please refer to Chapter 3. If the electronics behind the system in question fascinate the reader, Chapter 5 is your go-to section. For those intrigued by the thrust testing of a satellite's propulsion system, don't hesitate to read Chapter 6.

I would like to thank my supervisor Dr. Angelo Cervone, without whom this report wouldn't exist. Our many meetings, both calm and extremely informative, always made me happy and secure about my own progress, even if that was not what I believed in walking through the door. Secondly, Dr. Henk van Zeijl, thank you for the countless hours spent fabricating the chips and replying to my emails, always with fresh ideas in mind. Finally, a word of appreciation to the two students that performed their thesis at the same time as me: Andrei Pârvulescu and Jules Vaes. Our time together in the workshop and the cleanroom certainly made those months more bearable.

Gabriel Alves Teixeira
Delft, November 2024

Summary

Over the past decade, the micro-satellite industry has grown exponentially. With an original goal of providing university students an opportunity to learn by working on real flight models to be launched into space, their range of applications has quickly adapted to spark the private sector's interest, from earth observation missions to communication networks. To enable this type of satellites to last longer in space and become even more cost-efficient, the miniaturisation of satellite propulsion systems has also gained a lot of traction as of late.

In close collaboration with the Else Kooi Laboratory (EKL) of the Faculty of Electrical Engineering, the Space Engineering (SpE) department at the TU Delft has been developing two types of electric micro-propulsion systems to be used in such satellites for well over a decade. The two systems in question, based on Micro Electro-Mechanical System (MEMS) technology, are named the Vaporizing Liquid Micro-Resistojet (VLM) and the Low Pressure Micro-Resistojet (LPM). Extensive studies, both theoretical and practical, have been performed on the former, however a large gap exists in terms of experimental data regarding the latter, the LPM. What sets the LPM apart is its ability to work under very low plenum pressures, in the order of 50 Pa, operating under the transitional flow regime in terms of molecular dynamics (i.e. $0.1 < Kn < 10$). With this in mind, the goal of this thesis project is to "*characterise the newest version of the TU Delft LPM in terms of its mechanical, electrical, and propulsive performance by developing an appropriate thruster interface and performing the necessary testing efforts*".

A new thruster interface, complying with typical micro-satellite requirements, has been designed and manufactured out of Teflon. This new interface allows for pressure measurements in the thruster plenum, as well as Kelvin resistance measurements, increasing the accuracy of the desired temperature control of the thruster chip itself. Furthermore, the fabrication of the new LPM chips has been characterised both mechanically and electrically, in terms of its actual dimensions, as well as its resistance and temperature coefficient of resistance (TCR). The chips have hence also been calibrated as temperature sensors, for a range of 40-140 °C. Finally, cold gas thrust tests were performed to analyse the propulsive performance of the chips. It was found that the two types of chip, named the Grid of Small Slots (GSS) and Grid of Holes (GH), produce a maximum thrust of 0.37 mN and 0.04 mN, respectively, when tested at plenum pressures of 300 Pa.

Contents

Nomenclature

Abbreviations

Abbreviation	Definition
Al	Aluminium
BoB	Breakout Board
CAD	Computer Aided Design
CR	Cleanroom
CVD	Chemical Vapour Deposition
DASML	Delft Aerospace Structures and Materials Lab
DMM	Digital Multimeter
DPQ	Delfi-PQ
DRIE	Deep Reactive Ion Etching
DSMC	Direct Simulation Monte Carlo
EKL	Else Kooi Laboratory
FMMR	Free Molecular Micro-Resistojet
GH	Grid of Holes
GLS	Grid of Large Slots
GPFS	General Purpose Feed System
GSS	Grid of Small Slots
IC	Integrated Circuit
KOH	Potassium Hydroxide
LPCVD	Low-Pressure Chemical Vapour Deposition
LPM	Low Pressure Micro-Resistojet
LVDT	Linear Variable Differential Transformer
MEMS	Micro Electromechanical System
Mo	Molybdenum
nNTS	nano-Newton Thrust Stand
OTS	Off-the-Shelf
PEVCD	Plasma-Enhanced Chemical Vapour Deposition
PLA	Polylactic Acid
PSU	Power Supply Unit
RF	Radio Frequency
RIE	Reactive Ion Etching
ROI	Region of Interest
SCCM	Standard Cubic Centimetre per Minute
SpE	Department of Space Engineering
TCR	Temperature Coefficient of Resistance
TEOS	Tetraethoxysilane

Abbreviation	Definition
Ti	Titanium
UV	Ultraviolet
VTDC	Variable-Turn Density Coil
WBS	Work Breakdown Structure

Latin Symbols

Symbol	Definition	Unit
A_e	Exit area	$[m^2]$
E	Energy	$[J]$
F_T	Thrust	$[N]$
g_0	Acceleration due to gravity	$[m/s^2]$
h	Enthalpy	$[J]$
h_e	Enthalpy at the microchannel exit	$[J]$
h_e	Enthalpy at the microchannel inlet	$[J]$
Kn	Knudsen number	[-]
k	Boltzmann constant	$[J/K]$
L	Characteristic length	$[m]$
m	Mass	$[kg]$
m_a	Mass of propellant particles	$[kg]$
$\dot{m}$	Mass flow	$[sccm]$
n	Number density	$[m^{-3}]$
P	Pressure	$[Pa]$
P_a	Ambient pressure	$[Pa]$
P_e	Exit pressure	$[Pa]$
P_0	Plenum pressure	$[Pa]$
$\boldsymbol{p}$	Momentum vector	$[kgm/s]$
$\dot{Q}$	Heat transfer rate	$[W]$
R	Resistance	$[\Omega]$
R_0	Resistance at the reference temperature	$[\Omega]$
$\boldsymbol{r}$	Position vector	[-]
T	Temperature	$[K]$
T_{int}	Internal temperature	$[K]$
T_{tr}	Translational kinetic temperature	$[K]$
T_w	Wall temperature	$[K]$
T_0	Plenum temperature	$[K]$
u	Velocity component in the X direction	$[m/s]$
u_e	Exit velocity in the X direction	$[m/s]$
$\boldsymbol{v}$	Velocity vector	$[m/s]$
v	Velocity component in the Y direction	$[m/s]$
v'	Thermal speed	$[m/s]$
$\bar{v'}$	Average thermal speed	$[m/s]$

Symbol	Definition	Unit
v_e	Exit velocity	$[m/s]$
w	Velocity component in the Z direction	$[m/s]$

Greek Symbols

Symbol	Definition	Unit
α	Transmission coefficient	[-]
γ	Specific heat ratio	[-]
Δ	Difference	[-]
ζ	Number of degrees of freedom	[-]
κ	Thermal conductivity	$[W/mK]$
λ	Molecular mean free path	$[m]$
ρ	Density	$[kg/m^3]$
ρ_r	Material resistivity	$[\Omega m]$
σ	Molecule collision cross-section	$[m^2]$
ϕ	Aspect ratio of the channel or slot	[-]
Ψ	Arbitrary physical quantity	[-]
$\dot{\Psi}$	Flux per unit area of an arbitrary physical quantity	[-]

List of Figures

List of Tables

1

Introduction

Initially thought to be used as educational platforms by a group of professors from Caltech and Stanford universities, in the last decade CubeSats and other micro-satellites have taken the space industry by storm. The standardisation of the market, coupled with the increased necessity for reliable and fast Earth Observation and other scientific data have led to an exponential increase in the micro-satellite industry over the last decade. Due to this, a new branch within satellite propulsion gained traction: micro-propulsion systems. Even though these micro-satellites are orders of magnitude cheaper than conventional satellites, it is of great interest to make them last longer in orbit, specially with the latest issues concerning space debris. This can only happen with advancements in the micro-propulsion community, constantly trying to decrease system mass and power consumption as most as possible without major loss of efficiency.

The Space Engineering (SpE) department of the Aerospace Faculty of the TU Delft is diving deeper and deeper into this very same objective. In close collaboration with the Else Kooi Laboratory (EKL), two MEMS based electric propulsion thrusters are currently in development and being worked on by several students in tandem: the Vaporizing Liquid Micro-Resistojet (VLM) and the Low Pressure Micro-Resistojet (LPM), the latter of which is the focus of this thesis. Out of the three types of LPM chip designed, only one was characterised in terms of its performance as a micro-satellite propulsion system. The main objective of this 9-month project is therefore to continue the development of the remaining chips and bring the design one step closer to a future flight demonstration.

This thesis report is structured as follows. Chapter 2 presents the literature study performed during the first two months of the project. Its goal is to fill any knowledge gap related to this emerging technology and hence derive the main research objective to be completed during the remainder of the project. Next, Chapter 3 presents the creation of the new LPM thruster interface, from requirement generation to prototyping and manufacturing of the final version. Chapter 4 then presents all of the experiments that are planned to be performed throughout the project. Furthermore, the mechanical characterisation of the chips, as well as the results from the electrical characterisation tests, are described in Chapter 5. Finally, the calibration procedures performed on the chosen thrust bench and the thrust test results for both chips are presented in Chapter 6, the report is concluded in Chapter 7, where the recommendations for

future students/researchers hoping to further advance the design of the LPM thruster are also included.

2

Literature Study

This chapter presents the literature study performed on the main topics pertaining to the new thruster developed by the TU Delft, the Low Pressure Micro-Resistojet, henceforth known as LPM (Guerrieri, Silva, Zeijl, et al., 2017). The aim of this chapter is to fill the knowledge gaps relating to this emerging technology by thoroughly analysing previous research and theory, with the ultimate goal of not only grasping the current state-of-the-art, but also refining the research objectives to be tackled for the remainder of the Thesis duration. For this goal to be accomplished to a high standard, several research questions have been posed to guide the process of reviewing the literature, as shown below:

Research Questions

- R.Q.1: *What are the main advantages of using the transition flow regime (with Knudsen numbers between 0.1 and 10) as opposed to continuum flow in the micro-resistojet?*
- R.Q.2: *What other green propellant(s) is/are more suitable than water in the current LPM design?*
- R.Q.3: *Is the addition of pressure regulators to such systems needed to ensure constant thrust profiles?*
- R.Q.4: *What are the main MEMS manufacturing technologies that have led the way to the design of the proposed micro-resistojet?*
- R.Q.5: *Given the conclusions arisen from the previous research questions, which research questions and objectives are suitable for the remainder of the thesis duration?*

The chapter starts by introducing the LPM and the current state-of-the-art, in Section 2.1. An overview of the working principles of the thruster, as well as theory of rarefied gas dynamics used to model such thrusters is then given in Section 2.2. This is followed by an investigation regarding the electro-thermal theory used in the LPM, in Section 2.3, and an in-depth description of the MEMS manufacturing technology used in its design, in Section 2.4. The chapter ends with an overview of typical micro-propulsion testing procedures, as seen in Section 2.5, and a conclusion, given in Section 2.6, where the answers to the research questions are summarised, and a new set of objectives and questions is posed for the remainder of the Thesis duration.

2.1. Low Pressure Micro-Resistojet

The LPM, short for Low Pressure Micro-Resistojet, is a micropropulsion system designed by the TU Delft (Guerrieri, Silva, Zeijl, et al., 2017) as an extension of the Free Molecular Micro-Resistojet (FMMR) first proposed by Ketsdever et al. (1998). As is the case with all resistojets, the propellant is fed from the propellant tank towards a plenum, where it is electrically heated by means of a heater (resistance) and expelled into outer space, generating thrust. What is unique about FMMRs is the fact that the propellant molecules do not need to be accelerated using converging-diverging nozzles, as simple, straight-geometry expansion slots will suffice (Cervone, 2022). The designed systems are made up of three distinct parts as shown in Figure 2.1: propellant storage, propellant feed and thruster. The propellant storage and feed system are trivial, comprising of a propellant tank, a fill and drain valve, a feed line, a filter (if desired) and a valve responsible for allowing the propellant gas to flow into the thruster. Upon entering the thruster assembly, the propellant gas goes through a plenum before entering a heater chip manufactured using Microelectromechanical system (MEMS) technology, where it is accelerated and expanded to outer space through the expansion slots. In principle, all propellant phases can be used in the system (liquid, gas or solid) (Cervone, 2022) as long as the propellant arrives at the plenum in its gas phase, by ensuring evaporation if stored in the liquid state, or sublimation if done so in the solid phase.

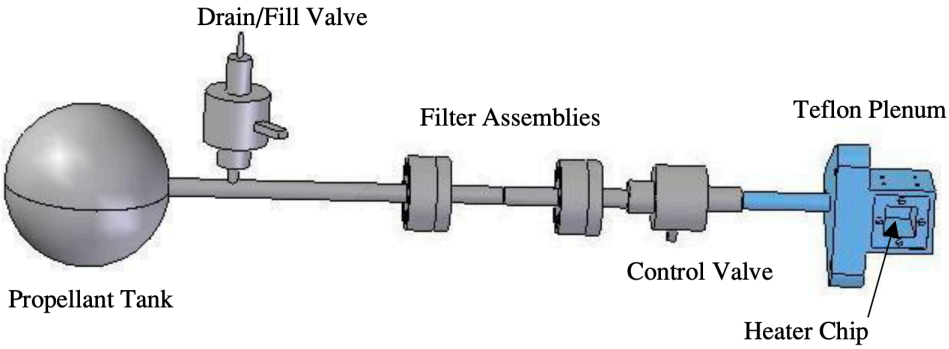

Figure 2.1: FMMR schematic showing the propellant storage and feed system in grey, and the thruster in blue (Ketsdever, Lee, & Lilly, 2005).

The first version of the FMMR thruster was already quite similar to current designs, with the main difference being that the polysilicon thin film heater and the expansion slots were decoupled, as shown in Figure 2.2. Figure 2.3 presents a more recent design, where the 19.2 x 19.2 mm^2 x 500 µm double sided silicon wafer heater chip combines both an updated heating element and 44 expansion slots each 100 µm wide x 5.375 mm long using advancements in MEMS technologies. Note that the heater elements and the expansion slots are now coupled. This change was realised with two objectives in mind. First, a decoupled structure between heater and slot lead to a decrease in propellant molecule energy, critical in terms of thrust and specific impulse. Having the slots themselves heated assures that the propellant molecules escape with as much velocity as possibly. Secondly, this design change allowed for the thruster chip to be even more compact, easing their compliance with the strict micro-satellite requirements typically seen.

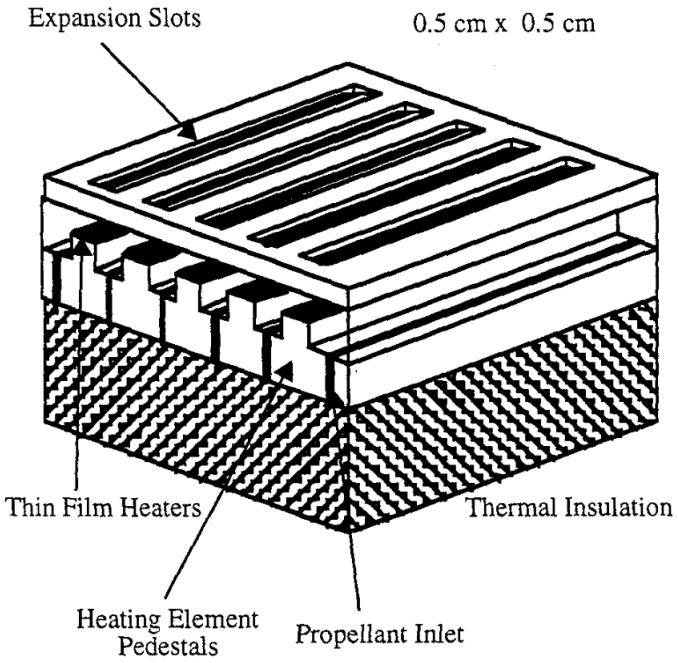

Figure 2.2: A 3D view of the first FMMR thruster proposed in Ketsdever et al. (1998), where the heater and the expansion slots are clearly decoupled.

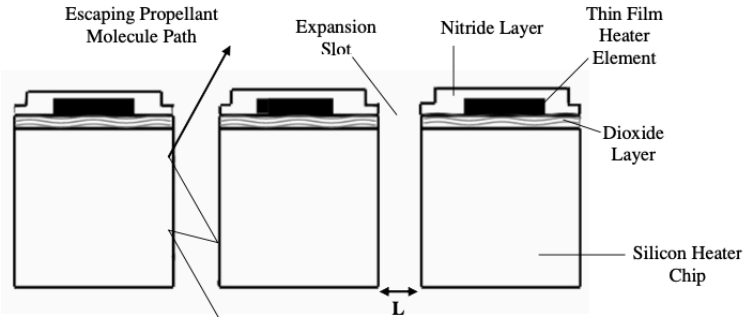

Figure 2.3: A 2D representation of the updated FMMR thruster by Ketsdever, Lee, and Lilly (2005), showing the expansion slots and the heater as one part.

As a means of reducing the total power consumption of the system, while increasing its efficiency, Palmer et al. (2013) designed a version of the FMMR where the heated structure is thermally insulated by a thick frame of silicon dioxide, as per Figure 2.4. They proved that it is possible for the heated island walls to maintain a temperature of around 270 °C while keeping the temperature of the surrounding silicon dioxide frame as low as 50 °C, showing that the heat loss of the system can be limited even further. On the other hand, Cervone et al. (2015) presented a complete conceptual design offering a different method of lowering the power consumption of such a system. Based on a propellant tank filled with a sublimating solid propellant (water in this case) at a pressure of 600 Pa, and an optimised expansion slot with a 15° divergence angle, the design is able to attain even lower thrust levels hence ensuring lower power consumption.

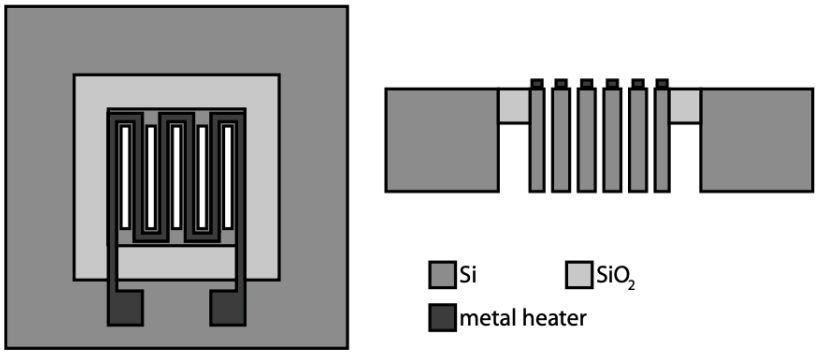

Figure 2.4: Schematic of the design by Palmer et al. (2013) showing the heating element surrounded by a silicon dioxide frame. A top view is shown on the left, whereas the figure on the right represents the design's cross section.

The effect of the shape and aspect ratio of the microchannel on the performance of the LPM was analysed by Guerrieri et al. (2016). They performed a sensitivity analysis on four different microchannel geometries using numerical simulations: a baseline rectangular channel and three others with different degrees and lengths of divergent sections, as seen in Figure 2.5. The main conclusion is that increasing the divergence angle leads to higher values of mass flow rate at the expense of heat transfer effectiveness. Nevertheless, it is shown that by varying the degree and length of the divergent section, it is possible to achieve a 480 % larger thrust with a mere decrease in I_{sp} of 5% and a decrease in power consumption of 66.7%.

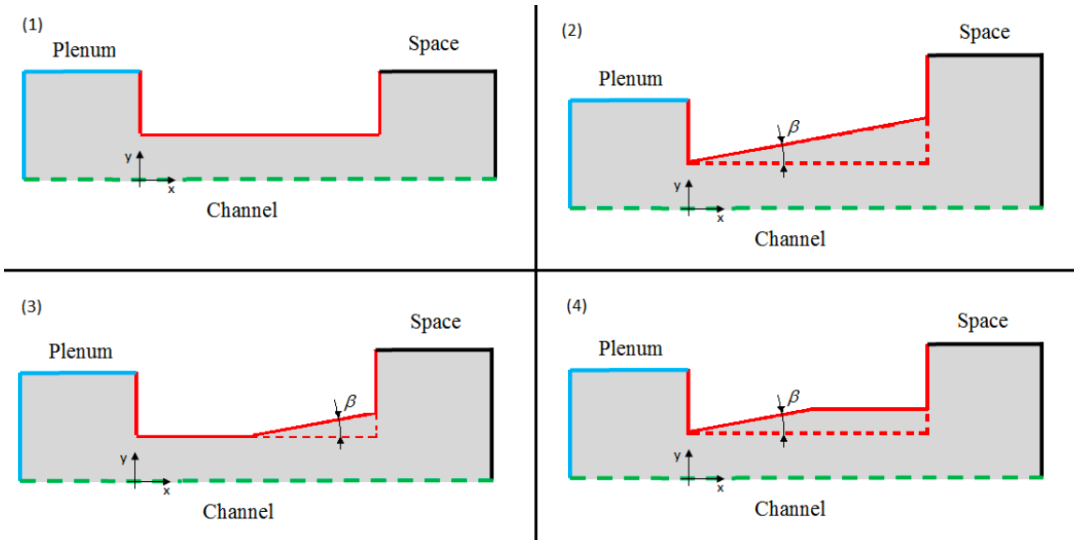

Figure 2.5: Schematic depiction of the four microchannels analysed by Guerrieri et al. (2016).

Guerrieri, Silva, Zeijl, et al. (2017) designed and manufactured three distinct heater chips with integrated temperature measurement, giving rise to the first LPM prototype fabricated in the TU Delft. All three were assessed in terms of their mechanical and electrical characterisation, whereas one was tested for its propulsive capacity by using Nitrogen gas as propellant, achieving thrust values of up to 1.4 mN. It was proven that the Molybdenum (Mo) heater was a good choice in terms of its high-temperature stability, allowing the temperature to be measured

quite accurately, and that the design has potential in fully operational conditions. Moreover, Guerrieri et al. (2018a) presents the first optimisation of the LPM with regards to two specific missions: a CubeSat mission requiring formation flight manoeuvres, and a PocketQube to be used as a flight demonstration platform. Suitable propellant tanks are discussed for both cases, and optimal chip areas are found, namely: 722.4 mm^2 for the CubeSat mission, and 593.8 mm^2 for the PocketQube. Finally, the latest LPM design was done by Singh (2023). In this design, shown in Figure 2.6, a decrease of 31% in volumetric space occupied by the LPM was achieved by bonding the interface parts rather than fastening, with only a 0.4% decrease in thrust (determined analytically) and the fabrication process was updated, reducing by 4% the number of steps required by utilising simpler processes.

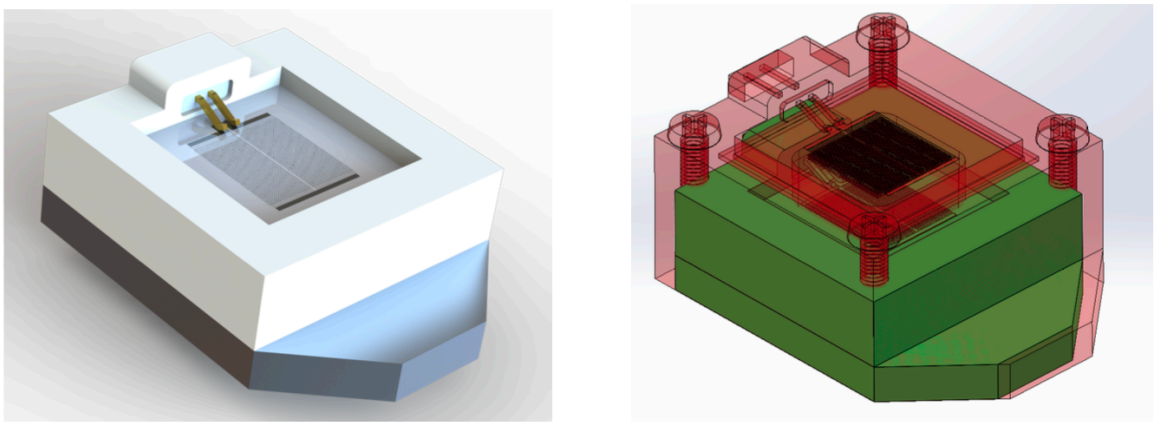

Figure 2.6: 3D model of the proposed LPM (left) and comparison (right) between the design by Guerrieri, Silva, Zeijl, et al. (2017) in red and Singh (2023) in green.

There are many features of the LPM that are advantageous for microsatellite operations over typical nozzle expansion systems: low system mass, low pressure operation, low power consumption and low propellant storage volume. As is the case with every propulsion system ever designed, a low pressure is always beneficial, as the lower the pressure, the lower the system complexity and mass. For example, the propellant leak rate, a typical point of concern regarding pressurised systems, can almost be neglected. The low pressure requirement also means that the thruster can operate on the propellant's vapour pressure, giving rise to yet another advantage: flexibility with the propellant storage phase (i.e. can be stored in the liquid or solid state). Last but not least, as mentioned above, the LPM does not require convergent-divergent nozzles, as simple geometry expansion slots will suffice. This presents quite a big advantage, as nozzle choking and blockage effects can be ignored, decreasing the overall single points of failure of the system. (Ketsdever, Lee, & Lilly, 2005)

2.2. Theoretical Background - Molecular Gas Dynamics

In general, a gas flow can be modelled as either a continuum or a rarefied flow. When modelling a gas flow at a macroscopic level, the flow is regarded as a "continuous medium" (Bird, 1994). The flow is said to be a continuum when the mean free path of a flow, or the average distance molecules travel between collisions, is much smaller than the characteristic length. In other words, molecules will collide with each other and with the boundary so often that a con-

tinuous distribution of the fluid properties can be assumed at any location in the flow. However, as written by Gad-el-Hak (2002), when considering the microscopic model, with much smaller geometries such as MEMS devices and "low-pressure applications such as high-altitude flying and high-vacuum gadgets", the mean free path is generally larger than the characteristic dimension, in which case the flow is said to be rarefied. The degree of rarefaction of a flow is measured by the Knudsen number, defined as the ratio between the two quantities described above as shown in Equation (2.1), where λ is the mean free path of the molecules, L is the characteristic length of the flow. It can also be described in terms of the pressure and temperature (Palmer et al., 2013), where k is the Boltzmann constant, T is the temperature, P is the pressure and σ is the molecule collision cross-section. Finally, Gad-el-Hak (2002) further describes the Knudsen number in terms of two of the most important dimensional parameters in the real of fluid mechanics: the Reynolds (i.e. the ratio between inertial and viscous forces) and Mach number (i.e. the ratio between the velocity of a flow and the speed of sound). In this final equation, γ is the specific heat ratio.

$$Kn = \frac{\lambda}{L} = \frac{kT}{\sqrt{2}\sigma PL} = \sqrt{\frac{\pi\gamma}{2}}\frac{M}{Re} \tag{2.1}$$

The LPM was designed to operate with Knudsen numbers ranging from 1 to 10 (1 < Kn < 10) in the plenum, that is, in the transitional flow regime as per Figure 2.7.

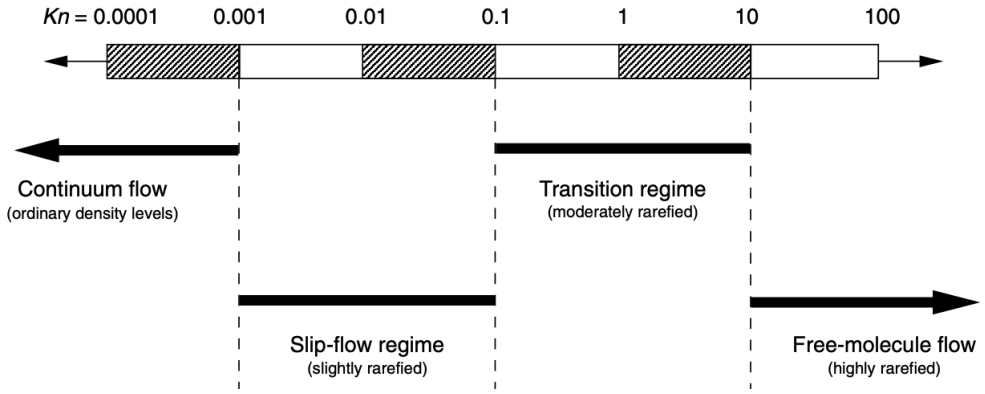

Figure 2.7: Flow regimes based on the Knudsen number (Gad-el-Hak, 2002).

2.2.1. Numerical Modelling

The conventional mathematical model used to perform simulations of fluids in the continuum regime is based on the Navier-Stokes equations. These are extensions of the Euler equations, which neglect the effect of viscosity. As the Kn number surpasses 0.1, the Navier-Stokes equations lose their validity, and the Boltzmann equation must be used. The relationship between the different numerical models and the Kn number can be seen in Figure 2.8. (Bird, 1994)

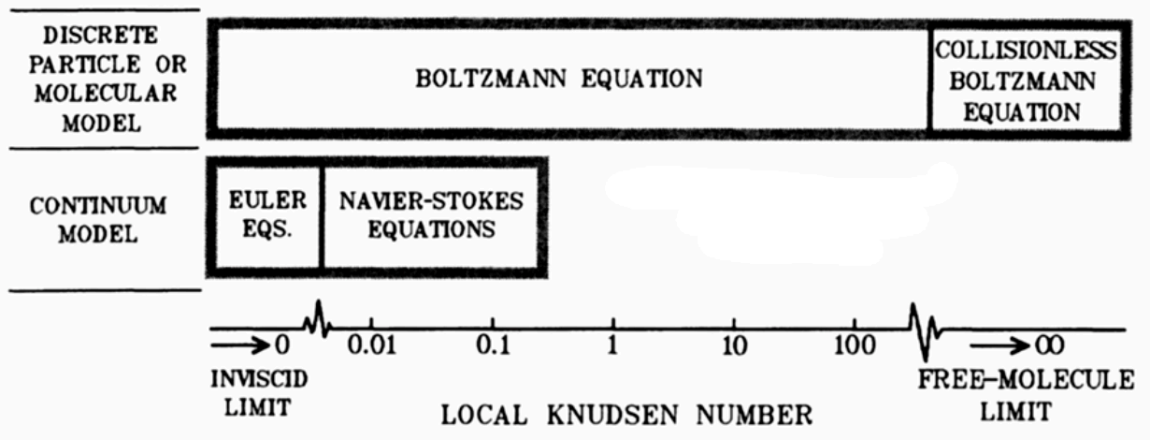

Figure 2.8: Validity of fluid flow modelling equations based on the Kn number (Bird, 1994).

Since, as mentioned above, the LPM is designed to operate at $1 < Kn < 10$, and assuming thermodynamic equilibrium in the plenum, the Boltzmann equation, Equation (2.2) can be used to describe the fluid dynamics (Bird, 1994):

$$\frac{\partial f}{\partial t} + \frac{\boldsymbol{p}}{m_a} \cdot \frac{\partial f}{\partial \boldsymbol{r}} + \boldsymbol{F} \cdot \frac{\partial f}{\partial \boldsymbol{p}} = \left(\frac{\partial f}{\partial t}\right)_{coll} \tag{2.2}$$

where f is the Maxwell-Boltzmann distribution function, $\boldsymbol{p}$ is the momentum vector, $\boldsymbol{r}$ is the position vector and $\boldsymbol{F}$ is the external force vector. The Maxwell-Boltzmann distribution function is defined below, where $\boldsymbol{v}$ is the molecule velocity vector, m_a is the mass of the gas molecules, and T is the thermodynamic gas temperature:

$$f(\boldsymbol{v}) = \left(\frac{m_a}{2\pi kT}\right)^{3/2} \exp\left(\frac{-m_a(\boldsymbol{v^2})}{2kT}\right) \tag{2.3}$$

Currently, the most widely used method to solve the Boltzmann equation to simulate the transition flow regime is the Direct Simulation Monte Carlo (DSMC) method. Developed by Bird (1963), the DSMC is valid for all values of Kn, however it becomes quite expensive computationally for $Kn < 0.1$. Coincidentally, this is the continuum regime and the Navier-Stokes equations can be used instead. The DSMC method is a statistical method whose main assumption is to uncouple the motion of the molecules from their collisions over small time intervals, significantly decreasing the computational time required when compared to fully deterministic Molecular Dynamics (MD) solvers. It models the motion of the molecules deterministically, yet it treats molecular collisions probabilistically, where each simulated molecule represents a much larger number of real molecules (Gad-el-Hak, 2002).

2.2.2. Analytical Modelling

Ketsdever, Lee, and Lilly (2005) developed an analytical model to estimate the performance of the FMMR which assumes $Kn >> 1$. Taking an orthogonal coordinate system in which the x direction is parallel to the wall of the slots, assuming the exit flow to be axial, and the exit of the slot to be in the $y - z$ plane, the general formulation for the flux per unit area $\dot{\Psi}$

of any physical quantity Ψ in the direction of the flow can be described as (Ketsdever, Lee, & Lilly, 2005):

$$\dot{\Psi} = \int_{-\infty}^{\infty}\int_{-\infty}^{\infty}\int_{0}^{\infty} \Psi v_x' f(v_x') dv_x' dv_y' dv_z' \tag{2.4}$$

where v_x' is the speed of the propellant molecules in the x direction, and $f(v_x')$ is Maxwellian distribution function. An expression for the mass flow of propellant molecules leaving the expansion slot axially can be derived by setting $\Psi = \alpha m_a n$, where α is the transmission probability and n is the number density (i.e. the number of molecules per unit volume). The transmission probability is the probability that a propellant molecule that enters the expansion slot will successfully exit it and produce thrust. It strictly depends on the shape and size of the (micro)channel. Lafferty (1998) derived empirical relations to calculate the transmission coefficient as a function of the channel's aspect ratio, as shown in the examples below. Equation (2.5) gives the transmission coefficient of molecules through short uniform rectangular cross sections (i.e. slots), where the aspect ratio ϕ is defined as the ratio between the length of the slot in the direction of the flow and the smallest cross-sectional dimension. On the other hand, Equation (2.6) does the same for cylindrical cross sections. In this case, ϕ is defined as the ratio between the channel's length and its diameter.

$$\alpha = 0.5(1 + \sqrt{1+\phi^2} - \phi) - \frac{1.5[\phi - ln(\phi + \sqrt{1+\phi^2})]^2}{\phi^3 + 3\phi^2 + 4 - (\phi^2+4)\sqrt{1+\phi^2}} \tag{2.5}$$

$$\alpha = 1 + \phi^2 - \phi\sqrt{\phi^2+1} - \frac{[(2-\phi^2)\sqrt{\phi^2+1} + \phi^3 - 2]^2}{4.5\phi\sqrt{\phi^2+1} - 4.5ln(\phi + \sqrt{\phi^2+1})} \tag{2.6}$$

The mass flow exiting the LPM is therefore given by Equation (2.7), where A_e is the exit area of the expansion slots and $\bar{v'}$ is the average thermal speed of the propellant molecules given by Equation (2.8), where T_0 is the plenum temperature.

$$\dot{m} = \alpha m_a n \frac{\bar{v'}}{4} A_e \tag{2.7}$$

$$\bar{v'} = \sqrt{\frac{8kT_0}{\pi m_a}} \tag{2.8}$$

By combining the two equations above with the ideal gas law ($P = nkT$), Ketsdever, Lee, and Lilly (2005) obtains the following expression for the mass flow, where P_0 is the plenum pressure:

$$\dot{m} = \alpha P_0 \sqrt{\frac{m_a}{2\pi k T_0}} A_e \tag{2.9}$$

The thrust F_T of a propulsion system is given by the sum of two terms: the momentum thrust and the pressure thrust. The momentum thrust is related to the linear momentum transported through the exit of expansion slots, whereas the pressure thrust arises from the pressure differential between said exit and the ambient (P_e - P_a). Ketsdever, Lee, and Lilly (2005) assume a negligible pressure thrust, leading to Equation (2.10), where v_e is the exit velocity of the gas molecules. As the gas molecules go through the heated walls, their kinetic energy will increase and their velocity when exiting the slots is given by Equation (2.11), where T_w is

the temperature of the heated walls. By combining Equations (2.11) and (2.9) with Equation (2.10), an analytical expression for the theoretical thrust of the LPM is obtained, as shown below:

$$F_T = \dot{m}v_e + (P_e - P_a)A_e \approx \dot{m}v_e \tag{2.10}$$

$$v_e = \sqrt{\frac{\pi k T_w}{2m_a}} \tag{2.11}$$

$$F_T = \frac{\alpha P_o A_e}{2}\sqrt{\frac{T_w}{T_0}} \tag{2.12}$$

The most common quantity used to measure how efficiently a thruster utilises its propellant is the specific impulse I_{sp}, defined as the total impulse delivered by the thruster per unit weight of propellant used. Mathematically, the I_{sp} is obtained by dividing the thrust of the system by its mass flow and acceleration due to gravity g_0:

$$I_{sp} = \sqrt{\frac{\pi k T_w}{2m g_0^2}} \tag{2.13}$$

Finally, the overall propulsion system efficiency η (i.e. the propulsive efficiency) is given by Equation (2.14), where $\wp$ is the heater chip input power (Ketsdever, Lee, & Lilly, 2005):

$$\eta = \frac{F_T I_{sp} g_0}{2\wp} = \frac{F_T^2}{2\dot{m}\wp} \tag{2.14}$$

Upon performing some experiments and comparing the results with the analytical model, Ketsdever, Lee, and Lilly (2005) show there is quite some difference between the two by plotting the mass flow as a function of the plenum pressure. They argue that there are two main reasons for these differences. Firstly, they point to the uncertainty in the fabricated MEMS heater chip, specifically in the area of the expansion slots. Secondly, and most importantly, they note that the flow in their FMMR is actually in the transitional flow regime, such as in the LPM, where there is a significant number of molecular collisions, whereas the model assumed free molecular (collisionless) flow.

By no longer assuming the pressure thrust term to be negligible (i.e. only $P_a = 0$), Guerrieri et al. (2018b) improved the analytical model above, which, when compared to experimental and numerical results, presented a higher degree of accuracy (maximum error of 10% versus 20-30% using the previous model). First, the exit velocity is reformulated by setting $\Psi = u$ in Equation (2.4) and dividing by the total flux through the surface. Note that the velocity components in the x, y and z directions are now named u, v and w respectively. Solving and writing the result as a function of the translational kinetic temperature T_{tr}, a measure of the molecule's translational kinetic energy:

$$u_e = \frac{\int_{-\infty}^{\infty}\int_{-\infty}^{\infty}\int_{0}^{\infty} u^2 f(u)dudvdw}{\int_{-\infty}^{\infty}\int_{-\infty}^{\infty}\int_{0}^{\infty} u f(u)dudvdw} = \sqrt{\frac{\pi k T_{tr}}{2m_a}} \tag{2.15}$$

Secondly, to model the pressure at the exit of the microchannel (i.e. the slot) Guerrieri et al. (2018b) redefines the mass flow as a function of the exit parameters, arriving at Equation

(2.16). Substituting in the ideal gas law $P_e = n_e k T_{tr}$ and Equation (2.15), the exit pressure is written as per Equation (2.17)

$$\dot{m} = m_a n_e u_e A_e \tag{2.16}$$

$$P_e = \frac{\alpha P_0}{\pi}\sqrt{\frac{T_{tr}}{T_0}} \tag{2.17}$$

The unknown that is left to complete the improved analytical model is the translational kinetic temperature. Upon defining a control volume as seen in Figure 2.9 and using the conservation of energy, the rate of heat transferred $\dot{Q}$ to the gas across the microchannel, assuming stagnation conditions at the plenum (i.e. u_0 = 0), can be defined as (Guerrieri et al., 2018b):

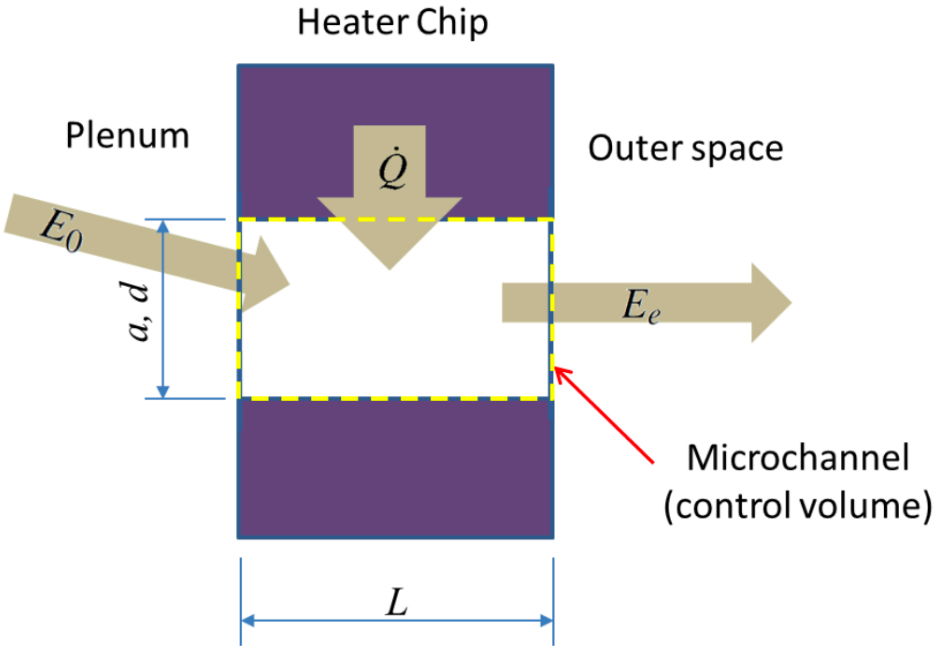

Figure 2.9: Graphical representation of the control volume used by Guerrieri et al. (2018b) to define the energy balance across the microchannel.

$$\dot{Q} = \Delta E = \dot{m}\Delta\left(h + \frac{u^2}{2}\right) = \dot{m}\left(h_e + \frac{u_e^2}{2} - h_0\right) \tag{2.18}$$

where E is the energy and h represents the enthalpy. As an ideal gas is assumed, the change in enthalpy $h_e - h_0$ can also be written as the product between the specific heat of the gas at constant pressure C_p and the difference between its inlet and exit temperatures $T_e - T_0$. Using this formulation instead, the heat transferred to the gas can be estimated as shown in Equation (2.19), leading to Equation (2.20). On the other hand, the C_p is the gas can be written as a function of its degrees of freedom ζ, as per Equation (2.21).

$$\dot{Q} = \dot{m} C_p (T_w - T_0) \tag{2.19}$$

$$C_p(T_w - T_e) = \frac{u_e^2}{2} \tag{2.20}$$

$$C_p = \frac{\zeta + 2}{2}\frac{k}{m_a} \tag{2.21}$$

As correctly pointed out by Guerrieri et al. (2018b), the overall temperature of diatomic and poly-atomic molecules is a function of both their translational kinetic temperature T_{tr} and their internal temperature T_{int}. Assuming the internal temperature to equal the microchannel wall temperature T_w:

$$T_e = \frac{3T_r + (\zeta - 3)T_w}{\zeta} \tag{2.22}$$

Relating the number of degrees of freedom to the specific heat ratio γ of the gas, and replacing Equations (2.15), (2.21) and (2.22) into Equation (2.20) leads to an equation for the translation kinetic temperature in terms of the specific heat ratio of the gas and the wall temperature of the microchannel, Equation (2.23). Finally, by inputting Equations (2.9), (2.15), (2.17) and (2.23) into the thrust equation, given by Equation (2.10), and assuming the ambient pressure $P_a = 0$, the new thrust and I_{sp} equations are given by Equations (2.24) and (2.25) (Guerrieri et al., 2018b):

$$T_{tr} = \frac{6\gamma}{\pi + 6\gamma}T_w \tag{2.23}$$

$$F_T = \frac{\alpha P_o A_e}{2}\left(\frac{\pi + 2}{\pi}\right)\sqrt{\frac{T_w}{T_0}\left(\frac{6\gamma}{\pi + 6\gamma}\right)} \tag{2.24}$$

$$I_{sp} = \frac{\pi + 2}{g_0}\sqrt{\frac{kT_w}{2\pi m_a}\frac{6\gamma}{\pi + 6\gamma}} \tag{2.25}$$

Finally, Guerrieri et al. (2018b) defines the propulsive efficiency of the LPM using the same equation as Ketsdever, Lee, and Lilly (2005), Equation (2.14), but also includes the power required by the tank to keep a constant sublimation/evaporation rate (i.e. mass flow rate). This is done by adding a heating element to the tank, and the power it requires equals the desired mass flow rate multiplied by the enthalpy of the phase change of water Δh_{sub} or Δh_{evap}. The efficiency in this model is therefore given by Equation (2.26), where, neglecting heat transfer losses, the heater chip power $\wp_w \approx \dot{Q}$, is given by Equation (2.19).

$$\eta = \frac{F_T I_{sp} g_0}{2(\wp_t + \wp_w)} \tag{2.26}$$

As seen by Equations (2.13) and (2.25), and as correctly written by Ketsdever, Lee, and Lilly (2005), the I_{sp} is directly proportional to the square root of the microchannel wall temperature and inversely proportional to the square root of the mass of propellant molecules. Therefore, one can do one of two things to increase the propellant usage efficiency: increase the wall temperature and/or choose a propellant with a low molecular mass. The former comes at the expense of the power usage, which shall be kept to a minimum as per typical micro-satellite requirements, whereas the latter is one of the main reasons for choosing water as a propellant, more of which will be discussed in the next section.

2.3. Electro-thermodynamics

Electro-thermal theory defines the main physical and chemical processes that occur during LPM operation: the generation of gas via sublimation/evaporation of the chosen propellant in the tank and the conversion of electricity to kinetic energy of the gas particles in the heated expansion slots. The heat transfer during these two processes is vital for the efficient operation of the LPM. Firstly, one must ensure the desired mass flow is fed to the plenum at all times. This can only be achieved via successful management of the sublimation/evaporation process, by carefully controlling the enthalpy within the tank. The choice of propellant to sublimate/evaporate will be explained in Subsection 2.3.1, followed by its storage conditions, in Subsection 2.3.2. On the other hand, as seen by the analytical models derived above, both the thrust and efficiency (i.e. I_{sp}) of the LPM are directly proportional to the exhaust velocity of the gas particles, which, in turn, is highly dependant on their temperature. The most important trade-off to be made with regards to the LPM is closely related to this: thrust and efficiency versus the power the heater chip requires to heat the particles to the desired temperature. This process, as well as the secondary purpose of the heater chip (i.e. to act as a thermocouple by characterising its resistance) are discussed in Subsection 2.3.3.

2.3.1. Choice of Propellant

Guerrieri, Silva, Cervone, and Gill (2017) performed an extensive characterisation of green propellants to be used in micro-resistojets, concluding with a single choice for the most suitable propellant for the LPM. By means of a feasibility assessment and a Pugh Matrix to compare all options with respect to their safety, performance, and system density, they narrowed down a list of over 90 different fluids to 9 promising propellants. They then performed a detailed analysis of the thrust, I_{sp} and power required to heat up each propellant in the LPM to arrive at the most suitable propellant. For this, they assumed a heater chip with a total exit area of 10000 μm^2 a transmission coefficient α of 0.19, and plenum temperatures and pressures of 300-700 K and 50-300 Pa, respectively, arriving at the results shown in Figure 2.10. As clearly seen in the figure, ammonia and water are by far the best choices, providing a much higher I_{sp} at similar power values than their opponents. To choose between the two, the paper further considers their density and the ΔV that can be achieved by both fluids. When it comes to miniaturised systems, a higher density is always preferable as a larger mass of propellant can be stored in the same volume. In this case, water comes out on top as it has a density around 1.5 times greater than that of ammonia (998.62 kg/m^3 vs 610.33 kg/m^3 in their liquid phase at 1 MPa). Figure 2.11 presents the ΔV per unit volume each propellant can achieve as a function of the input power. Clearly, water is again the favourable choice, as it provides almost twice as much ΔV as ammonia, for the same power level. The paper finally concludes that water is the most promising propellant for the current LPM design.

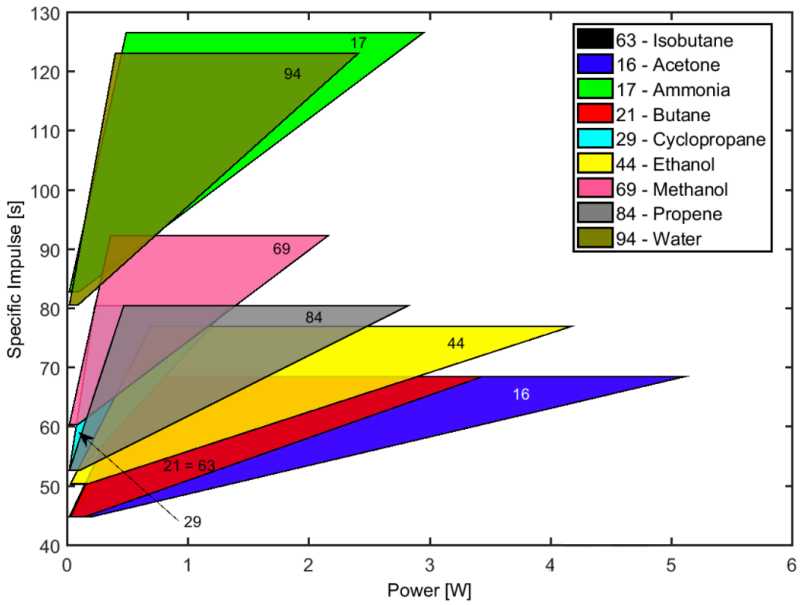

Figure 2.10: I_{sp} versus heating power for the 9 most promising propellants (Guerrieri, Silva, Cervone, & Gill, 2017).

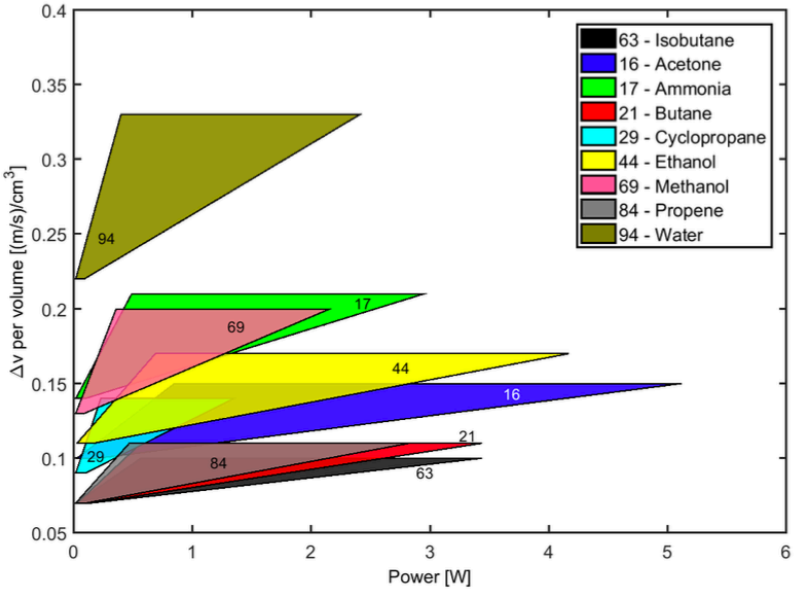

Figure 2.11: Velocity increment ΔV per unit volume versus the heating power required (Guerrieri, Silva, Cervone, & Gill, 2017).

2.3.2. Propellant Storage

The low pressure thruster design has been demonstrated experimentally (Ketsdever, Lee, & Lilly, 2005) and has already reached quite a high maturity level. However, the propellant storage system currently represents the main obstacle preventing its implementation in a spacecraft (Cervone et al., 2015). As mentioned in Section 2.1, the water is to be stored in the tank in its liquid or solid phase. This means that, before being fed to the plenum, it must first be

evaporated or sublimated. Cervone et al. (2015) proposed a system in which ice is constantly sublimating in the propellant tank to keep the tank pressure equal to the vapour pressure (600 Pa at 0 °C). The ice molecules lose heat as they sublimate, given by the product of the rate of sublimation and the enthalpy of sublimation of water (about 2.84 MJ/kg at the given conditions). To maintain equilibrium conditions in the tank, and hence a constant mass flow of gas into the plenum at the desired pressure, a heating element is required to pump in the same amount of heat lost to the ice. As the valve separating the tank and the plenum is opened, the pressure in the tank is lowered below the vapour pressure, making more ice sublimate and again reaching equilibrium conditions. This option has the advantage that equilibrium conditions are reached at a very similar pressure to what is needed to ensure the desired Kn numbers in the plenum, hence little to no pressure regulation is required. The downside is that, to avoid extra costs and procedures incurred if one wanted to keep the water frozen on ground during integration and launch, the water must be frozen in orbit. Hence, a cooling system is required apart from the heater mentioned above, likely increasing the overall power consumption of the system. The proposed system is depicted in Figure 2.12 below.

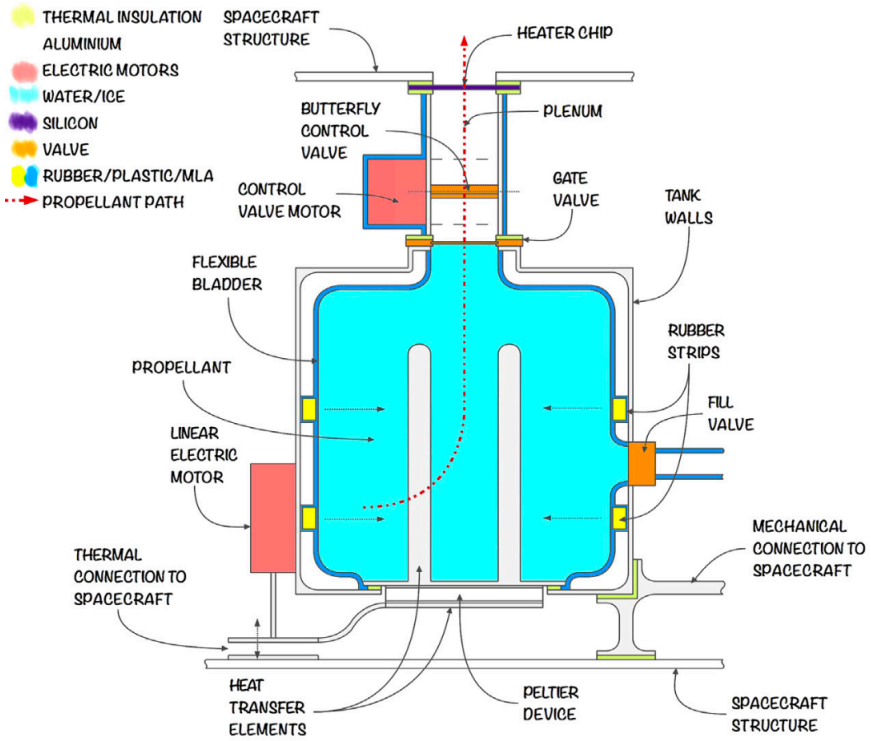

Figure 2.12: Graphical representation of the complete system architecture proposed by Cervone et al. (2015).

Focusing on the propellant storage system (i.e. everything under the gate valve), the design by Cervone et al. (2015) includes a main tank designed to store 100 g of solid water. This tank is made up of a rigid outer layer and a flexible inner membrane designed to keep the solid propellant in constant contact with the two heating elements. A Peltier device, powered by a linear electric motor, was chosen to freeze the water and to maintain the temperature of the ice constant during operation. The thermal energy is transferred via two aluminium fins constantly in contact with the propellant.

Maxence et al. (2017) performed an experimental campaign to provide a better understanding of the underlying physical principles that occur during the sublimation of ice in a tank in

vacuum conditions. The setup, represented by Figure 2.13, consisted of a plastic tube filled with frozen water, several thermocouples, a heater grid and a differential pressure sensor to measure the pressure inside the tube relative to the vacuum chamber the tube is placed in. The generated water vapour is allowed to escape through a small hole near the top of the tube, to emulate the vapour leaving the propellant tank and into the feed system of the LPM.

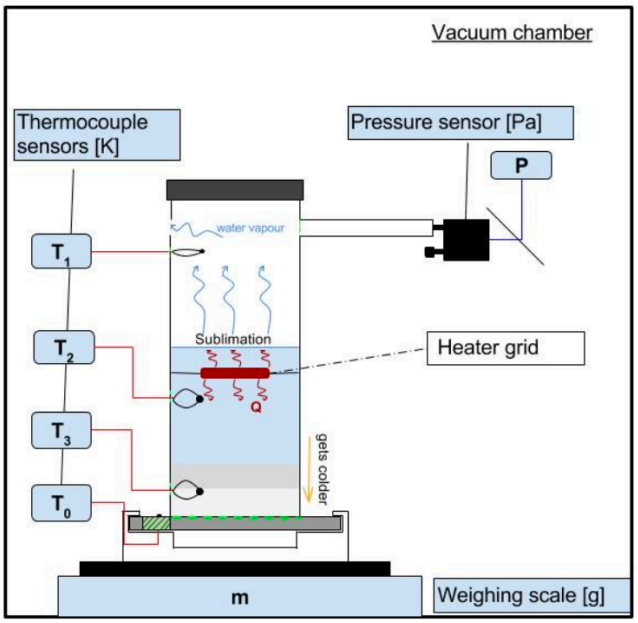

Figure 2.13: Experiment setup used by Maxence et al. (2017).

A sample of the results is shown in Figure 2.14, where Maxence et al. (2017) show that the pressure inside the tank can indeed be kept constant by accurately correcting for the heat lost due to sublimation, as predicted by the theory. The theoretical pressure was calculated using Equation (2.27) and the temperature measured by thermocouple T2, shown in Figure 2.13, whereas the measured pressure is the output of the pressure sensor P. Note that Equation (2.27), is an empirical equation based on an experimental data set that describes the pressure along the sublimation curve of ice, as derived by Wagner et al. (1994). Assuming that all the heat provided by the heater is used for sublimation (i.e. no heat loss within the system), they showed that the sublimation rate indeed increases with heater power. However, this only occurs until a power value of 2.8 W, after which the mass flow of sublimation will no longer increase, and even begins to decrease in some cases. This is most likely because if the heat flux to the ice is too large, it will start to melt, directly affecting the rate of sublimation.

$$\begin{aligned} P_{sub} &= e^{\theta} \\ \theta &= 9.550426 - 5723.265/T_{sub} + 3.53068log(T_{sub}) - 0.00728332T_{sub} \end{aligned} \tag{2.27}$$

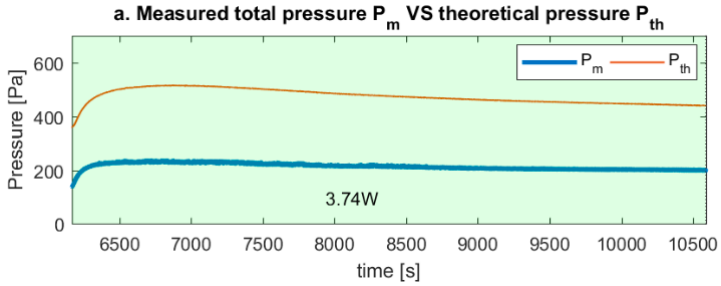

Figure 2.14: Example of results obtained from the pressure measurements for a heater power of 3.74 W. The two pressures are quite different in magnitude due to their measuring location (Maxence et al., 2017).

The other option for the propellant storage system is to store the water in its liquid phase and generate the required gas molecules by means of evaporation. The main difference when compared to the option explained above is that the vapour pressure is higher at the temperature in which water is in its liquid phase (1210 Pa at 10 °C or 1680 Pa at 15 °C (Lide, 2004)), therefore equilibrium in the tank will be reached at a much higher pressure than is required by the plenum to ensure the desired Kn number. The main downside of this option arises from this: the gas pressure will need to be regulated before it is fed to the plenum, increasing the complexity of the design. On the other hand, cooling capabilities are no longer necessary, decreasing the overall power required by the heater.

According to Guerrieri et al. (2018a), due to the low pressures required in the tank to keep the water at its desired liquid or solid state, the tank thickness can be calculated by simply taking into account the maximum expected launch loads. However, the low pressure in the tanks means that the atmospheric pressure on ground, when the satellite is waiting to be launched, is orders of magnitude larger than the tank pressure. This pressure gradient will likely lead to the tank collapsing and/or buckling if not taken into account while calculating the tank thickness. Nevertheless, suitable tanks are discussed for two reference mission scenarios: a formation flight to be performed by two identical CubeSats and a technology demonstration flight aboard a PocketQube. A wide variety of tanks is considered that can be put into three main categories: rigid tanks, flexible tanks and non-conventional tanks. Rigid tanks are immediately discarded due to the lack of sloshing prevention, which can be quite important in the case of having liquid water as propellant. The focus is shifted towards flexible tanks, which, due to the tough volume requirements typical to micro-satellites, are the type of tank that can be better optimised in terms of volume and propellant mass. Two types of flexible tanks are considered: bladder tanks and pipe tanks. Note that pipe tanks are generally not considered "flexible", but it is assumed that the author defined "flexible" as a tank that can, in theory, have any desired shape. The sloshing issue may still be present in bladder tanks as the bladder is typically free to move with the propellant, hence it is discarded. Guerrieri et al. (2018a) therefore conclude that pipe tanks are the most suitable for such types of satellites. Apart from the ability to optimise the propellant storage volume, capillary forces within the tank avoid mixing between the liquid/solid and gas phase of the water propellant. This type of tank shall be used in TU Delft's technology demonstration platform, the Delfi-PQ (Turmaine, 2018).

2.3.3. Heat Transfer & Resistivity of the MEMS Heater Chip

As can be seen in Equation (2.10), the thrust of the LPM is directly proportional to the mass flow $\dot{m}$ and the exit velocity v_e of the propellant particles, which in turn shares the same proportionality with their energy. This means that the performance of the thruster, and hence its efficiency, critically depend on the energy transfer between the heater chip and the propellant molecules (Ketsdever, Lee, & Lilly, 2005), which can be calculated using Equations (2.18) and (2.19). As mentioned in Section 2.1, Guerrieri et al. (2016) analysed the effectiveness of said heat transfer as a function of the shape of the expansion slot. Using the results for the entirely divergent channel (i.e. Case 2 in Figure 2.5), it was proved that, for an increasing divergence angle, the number of collisions between the propellant particles and the heated walls decreases, and hence so does the effectiveness of the heat transfer when compared the a straight channel. However, the divergent angle of the channel increases the acceleration of the particles due to thermal expansion, leading to a supersonic flow at the exit and hence larger exit velocities than the baseline (straight) case, as well as much larger transmission coefficients (and mass flows). The comparison between the straight channel (left) and divergent channel (right) can be seen in Figure 2.15. An optimum between the two counteracting effects was found in Case 4, where a divergent first half increases the thermal expansion and the mass flow rate and a straight second half increases the gas temperature.

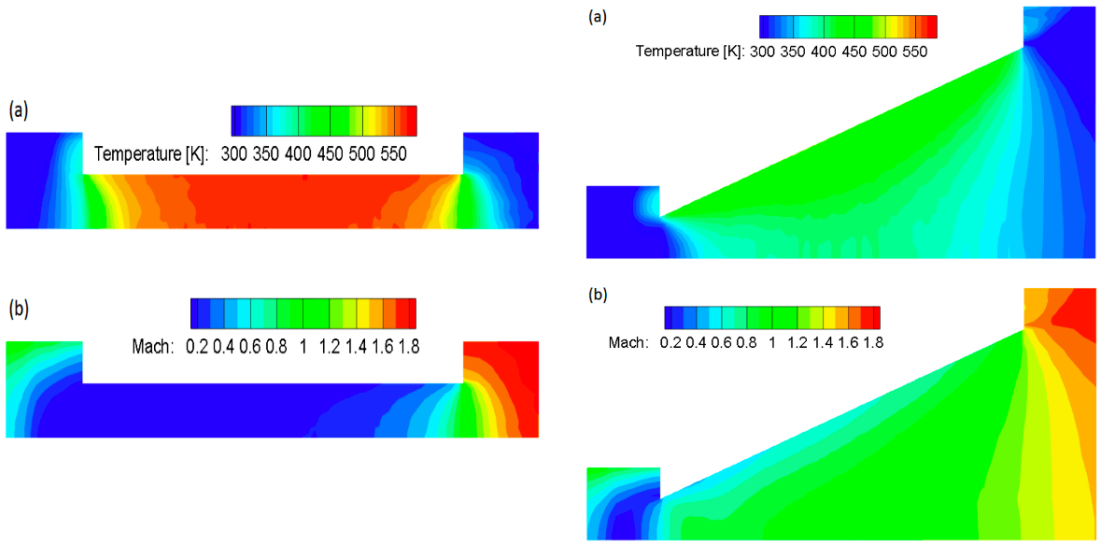

Figure 2.15: The effect of a divergent channel on the heat transfer effectiveness and exit velocity. Comparison between a straight channel, Case 1 (left), and a divergent channel, Case 2 (right). The plenum conditions are 300 K and 150 Pa, respectively, and the heater chip wall temperature is 573 K. (Guerrieri et al., 2016)

The heat transfer between heater chip and propellant can also be improved by limiting the heat lost to the surroundings by both conduction and radiation, as this is the major reason for the low power efficiency, and hence low thrust-to-power ratio of the proposed type of system (Palmer et al., 2013). Radiation is the main mode of heat transfer in the vacuum of space, and hence the main source of heat loss from a spacecraft to its surroundings. It can be calculated using Equation (2.28), where Q is the heat leaving the heater chip, ε is the material emissivity, A is the radiative area, σ is the Stefan-Boltzmann constant and T is the temperature. Clearly, it is desirable to apply surface coatings with low emissivity to increase the power efficiency

of the LPM. The other major cause of the low power efficiency of the system is the heat loss through conduction. This can be quantified by using Fourier's law of heat conduction, given by Equation (2.29), where $\dot{Q}$ is the heat flow, κ is the thermal conductivity, A is the cross sectional area, T_1 and T_2 are the temperatures of the two surfaces, and L is the distance between them (Giancoli, 2008). Losses due to conduction can be avoided by insulating the heater chip with materials that have low thermal conductivities, such as silicon dioxide, as done by Palmer et al. (2013). This analysis is not only applicable to the heater chip, but to the plenum as well. Ketsdever, Lee, and Lilly (2005) and Guerrieri, Silva, Zeijl, et al. (2017) use Teflon as the material of choice for the plenum of their respective designs to further reduce the heat losses and limit the power consumption required by the system to increase the temperature of the gas to a certain extent. However, the latter suggests the use of ceramic materials in future iterations of the design, which typically present better insulation properties and thermal resistivity.

$$Q = A\varepsilon\sigma T^4 \tag{2.28}$$

$$\dot{Q} = \kappa A \frac{T_1 - T_2}{L} \tag{2.29}$$

As briefly mentioned in Section 2.1, Guerrieri, Silva, Zeijl, et al. (2017) proposed a heater chip made of Molybdenum (Mo) with integrated temperature measurement, avoiding the need for extra thermocouples to be added on-board. The operating temperature T can be calculated as a function of the measured resistance R of the material using Equation (2.30) below, where β is the temperature coefficient of the resistance (TCR), and R_0 is the resistance measured at a reference temperature T_0. Firstly, the resistance at the reference temperature R_0 (room temperature in this case) is measured experimentally or simply calculated using Equation (2.31), where ρ_r is the material resistivity, L the material length and A_R the cross sectional area. To characterise the TCR, Guerrieri, Silva, Zeijl, et al. (2017) set up a power supply and a test bench fitted with a very accurate thermal camera. A constant voltage is then applied, and the resistance is measured as a function of temperature, allowing Equation (2.30) to be used to calculate β. Then, during operation, by actively measuring the resistance the same equation can be used again to monitor the heater chip temperature.

$$\beta = \frac{R - R_0}{R_0(T - T_0)} \tag{2.30}$$

$$R_0 = \frac{\rho_r L}{A_R} \tag{2.31}$$

The choice of material strongly impacts the overall performance of the heater chip. Mele et al. (2012) describes several materials that have been used in the past. Polysilicon works well, however, due to grain instability, it becomes unstable in terms of resistivity for temperatures above 550°C. Platinum is one of the most widely used materials as it is chemically inert, however its resistivity starts to drift above 650°C. In terms of temperature stability, titanium nitrate is promising, however a high stress on the heater chip is likely to cause yield problems. On the other hand, Molybdenum seems to be a more advantageous choice. It has a high melting point (2693°C) and is proven to be stable in temperatures up until 850°C. Standard etching techniques can be used (i.e. dry or wet etching, more to be discussed in the following section) and it is resistant to potassium hydroxide and hydrochloric acid, both of which are

typically used in MEMS manufacturing techniques. The only disadvantage is that it forms an oxide in air at around 300°C, which can be avoided by depositing a fine layer of Plasma-Enhanced Chemical Vapour Deposition (PEVCD) silicon oxide, or tetraethoxysilane (TEOS) in the case of Guerrieri, Silva, Zeijl, et al. (2017).

2.4. MEMS Manufacturing

As their name entails, MEMS are a set of processing techniques used to fabricate devices, such as sensors or actuators, on the micro scale in a single chip. Derived from integrated circuit (IC) technology, MEMS have been slated as one of the century's most promising technologies, and are used in a very extensive range of markets, from the medical industry to communication and defence systems. It is a considerably interdisciplinary set of technologies, utilising knowledge from many fields such as mechanical and electrical engineering, chemistry, and optical and instrumentation engineering.

In general, MEMS processing is based on the "addition or subtraction of two dimensional layers on a substrate (usually silicon) based on photolithography and chemical etching" (PRIME Faraday Partnership, 2002). Photolithography is the process of transferring a desired pattern onto a substrate, or wafer. The wafer is covered with a thin film polymer, called the photoresist, which is sensitive to ultraviolet (UV) radiation. The photoresist is then covered with a "mask", where the desired pattern is present, and the wafer is exposed to UV radiation, imprinting the desired pattern onto the photoresist. The parts of the photoresist that are no longer needed are then removed, or "developed". On the other hand, chemical etching is the process of removing a selected piece of material by using chemicals in their liquid or gaseous form. According to the PRIME Faraday Partnership (2002), there are three main types of processes used in MEMS fabrication:

- Bulk Micromachining: essentially a material removal, or "subtractive", process. Specific parts of the silicon wafer are removed by either wet or dry etching in order to create the desired channels/grooves. The former involves placing the wafer inside a chemical bath, where the chemical (i.e. the etchant) can be anisotropic or isotropic (orientation dependant or independent). The latter relies on high temperature reactive gases or vapours, and its most common form is reactive ion etching (RIE), where the wafer is etched by ion bombardment. Typical FMMR (and LPM) fabrication procedures make use of both techniques (Ketsdever, Lee, & Lilly, 2005)(Palmer et al., 2013)(Guerrieri, Silva, Zeijl, et al., 2017)(Singh, 2023).
- Surface Micromachining: in contrast to bulk micromachining, this procedure is based on building up the desired feature by applying extra layers on the surface of the silicon wafer, that are then patterned or etched. Said layers are either used to make up the desired structures, or as sacrificial material to, for example, provide support to a recently etched movable part and later be removed (PRIME Faraday Partnership, 2002)(Singh, 2023). The most common types of surface micromachining are low-pressure chemical vapour deposition (LPCVD) and plasma-enhanced chemical vapour deposition (PECVD), used to apply thin films or material onto the wafer (Gad-el-Hak, 2002).
- High Aspect Ratio (HAR) Micromachining: allows for high aspect ratio holes/trenches

to be etched onto the wafer. One of the main HAR processes is called deep reactive ion etching (DRIE), a highly anisotropic etching method used to fabricate every iteration of the LPM's expansion slots (Ketsdever, Lee, & Lilly, 2005)(Palmer et al., 2013)(Guerrieri, Silva, Zeijl, et al., 2017)(Singh, 2023).

2.4.1. LPM Fabrication

The LPM designed by Guerrieri, Silva, Zeijl, et al. (2017), which was also the first LPM prototype developed at the TU Delft, was manufactured in house. This was done at the Else Kooi Laboratory (EKL), part of the Faculty of Electrical Engineering, Mathematics and Computer Science, as well the Department of Space Engineering (SpE), in the Faculty of Aerospace Engineering. The EKL allows full production and assembly capabilities by providing state-of-the-art micro-manufacturing facilities for ICs and MEMS, including, but not limited to, photolithography, bulk micromachining, and thin film deposition. With over 600 m^2 of class 100 cleanrooms (ISO 5) and over 400 m^2 of class 10000 (ISO 7), it is one of the largest cleanrooms in the Netherlands (EKL, 2022).

As mentioned in Section 2.1, three different heater chip geometries were fabricated by Guerrieri, Silva, Zeijl, et al. (2017). The same heater mask was used for all three chips, however three different masks were used for the expansion slots, as seen in Figure 2.16. The heater consisted of two sets of resistances in series, each made up of nineteen 10 mm long, 20 µm wide and 200 nm thick resistances arranged in parallel made of Mo, with a design resistance of 105 Ω. On the other hand, the different expansion slot geometries included a configuration with ten 6.28 mm long slots (GLS) that are 200 µm wide, another with twice as many slots with the same length, but half the width (GSS), and a third configuration consisting of a grid of 40x40 holes with a diameter of 100 µm (GH).

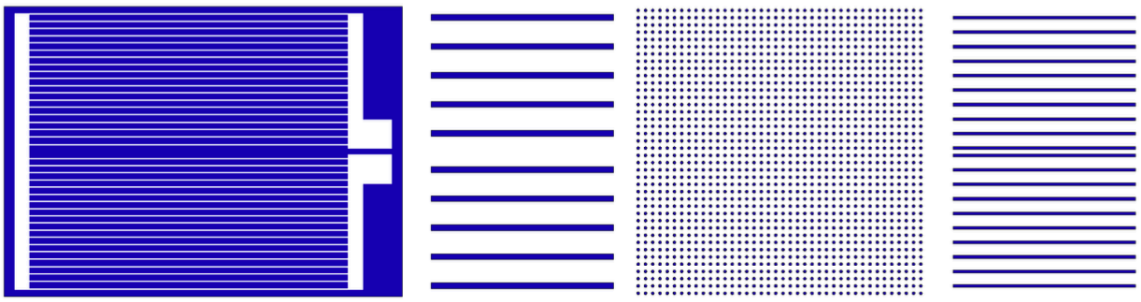

Figure 2.16: Graphical representation of the heater design and expansion slot geometries manufactured and tested by Guerrieri, Silva, Zeijl, et al. (2017).

Beginning with a 500 µm thick double side polished silicon wafer, Guerrieri, Silva, Zeijl, et al. (2017) follow an 11-step procedure to fabricate the LPM heater chips:

1. Lithographic marks are etched onto the wafer to increase the accuracy of the alignment of the next layers to be added.
2. To isolate the wafer and the heater, a 500 nm thick layer of LPCVD silicon nitride is

deposited, as shown in Figure 2.17a.

3. A 200 nm thick layer of Mo is sputtered onto the silicon nitride layer.
4. A 300 nm Tetraethoxysilane (TEOS) hard mask for the Mo layer is deposited using PECVD, Figure 2.17b.
5. The heater mask shown in Figure 2.16, made by photoresist, is deposited, Figure 2.17c.
6. To create the desired resistance geometry on the Mo layer, two wet etching processes are done: the hard mask is etched with buffered hydrochloric acid (BHF), and the photoresist with aluminium etch, Figure 2.17d. The photoresist is then removed with a plasma, and the remaining TEOS with BHF, Figure 2.17e.
7. As typically done during HAR Micromachining, to etch through the entire wafer, a hard mask is required on one side, and a stopping layer on the other. A 5 µm thick silicon dioxide layer is deposed on both sides, Figure 2.17f.
8. A photoresist layer acting as the soft mask for the chosen type of expansion slot geometry is deposed on the hard mask. Three wafers are produced in total, one for each expansion slot geometry.
9. The silicon oxide and nitride are plasma etched, Figure 2.17h.
10. Anisotropic DRIE is used to etch through the wafer, using the previous soft and hard masks, Figure 2.17i.
11. Masks and stopping layer are removed via wet etching.

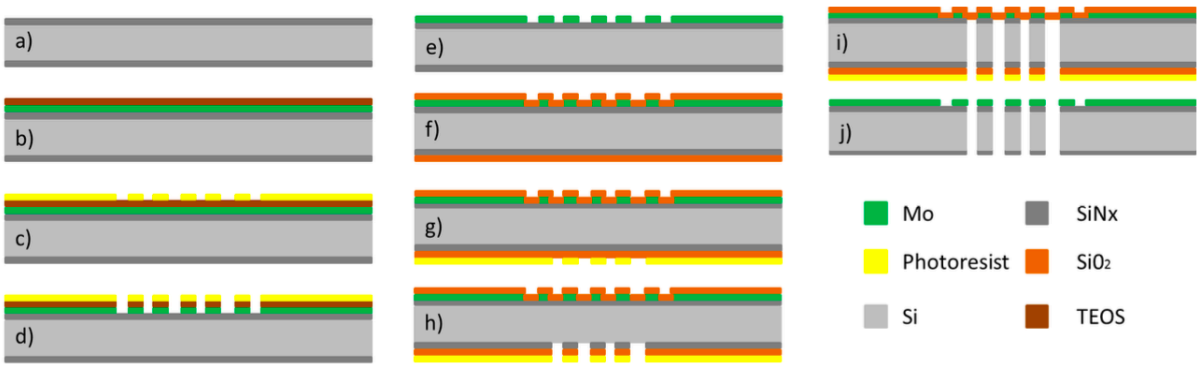

Figure 2.17: Cross section view of the chips during the manufacturing steps (Guerrieri, Silva, Zeijl, et al., 2017).

On the other hand, Singh (2023) devised a similar manufacturing procedure, including some changes and managing to decrease the fabrication complexity and time. The main difference with regards to the design by Guerrieri, Silva, Zeijl, et al. (2017) is that a 500 nm layer of titanium (Ti) was deposited for the resistance, as opposed to a 200 nm layer molybdenum. Although the above section concludes that Mo is clearly advantageous in terms of its electrical properties, when comparing both materials in terms of fabrication, the etching and deposition of Ti onto the wafer is far simpler than that of Mo, which was the main reason for this design change. Another extra step was introduced, with the future possibility of wire bonding the chip directly to a PCB in mind. Bonding to Ti does not work as the wires typically used are either aluminium or gold, hence the contact pads must be made of aluminium as well, by

sputtering a layer of it over the Ti and using a photoresist mask to develop the pads. Finally, a simple photoresist mask is used to etch the desired heater geometry, rather than first depositing a TEOS hard mask. These procedural changes proposed by Singh (2023) led to a decrease of 4% in number of steps, as well as the use of simpler metal deposition techniques. For comparison, this updated procedure can be seen in Figure 2.18. Further design changes concerning the heater mask were introduced by the manufacturer, Dr. Henk van Zeijl from the EKL laboratory in this case. For a more cost-effective process flow, three changes were made: the length of the resistance lines was increased to 11 mm, the spacing between the resistances was decreased from 230 µm to 130 µm, meaning that wafers with the GLS design could no longer be manufactured, and their width was increased from 20 µm to 120 µm. A total of 10 wafers were hence processed using the design by Singh (2023): 5 with the GH design, and 5 with the GSS. Using Equation (2.31) and a Ti resistivity of $4.8\text{x}10^{-7}$ Ωm (Sundqvist & Tolpygo, 2018), the design resistance of the new chips is calculated to be 9.26 Ω. The large difference between the design resistances of the chips by Guerrieri, Silva, Zeijl, et al. (2017) and Singh (2023) arise mostly from the order of magnitude difference between the resistivities of Ti and Mo.

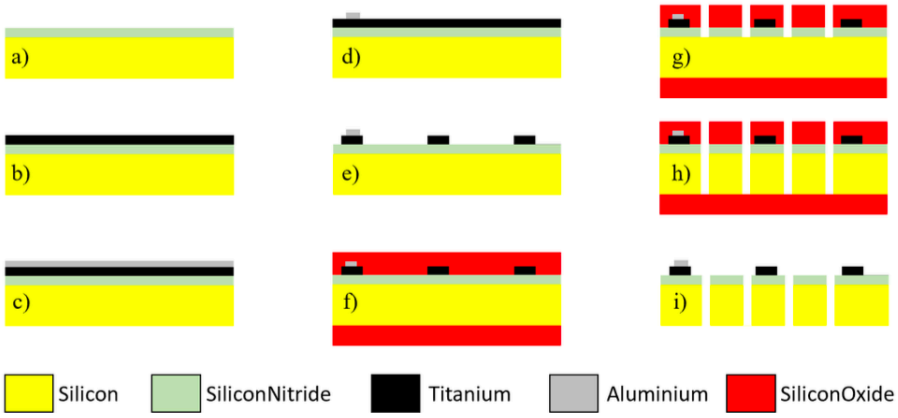

Figure 2.18: Manufacturing procedure proposed by Singh (2023). Note that photoresist layers are not shown, but are included between steps c-d, d-e, and f-g.

There are four main MEMS fabrication techniques that are used in both procedures described above that are yet to be discussed:

- LPCVD: a type of chemical vapour deposition (CVD) (surface micromachining) that involves placing the wafer in a type of vacuum chamber with a certain reactive gas, and using heat to start a reaction between the gas and the surface of the wafer. The low pressure allows for increased layer uniformity and better control of the reactions taking place within the chamber (Lurie Nanofabrication Faculty, 2020a).
- PECVD: another type of CVD in which a plasma, generally created by a radio frequency (RF), is used for the reaction between the gas and the wafer surface to take place, rather than using a high temperature (Lurie Nanofabrication Faculty, 2020b).
- Sputtering: a type of physical vapour deposition (PVD) where a gas plasma is used to knock off atoms from a source material (called the target) which condense into a thin film upon contact with the wafer surface (Lurie Nanofabrication Faculty, 2023).

- DRIE: a type of RIE used to create deep, high aspect ratio surfaces, hence it belongs to two main groups: bulk micromachining and HAR micromachining. The wafer is placed into a vacuum chamber with a certain gas/gases. An RF is used to create a gas plasma which is then accelerated towards the places to be etched on the wafer surface, marked by a mask, by applying a negative current to it (Lurie Nanofabrication Faculty, 2021).

The accuracy of the fabrication procedures can vastly affect the thruster performance. Guerrieri, Silva, Zeijl, et al. (2017) performed a mechanical characterisation on the heater chips fabricated using the step-by-step procedure described above. First, it was discovered that the silicon nitride layer on one of the sides was not etched correctly in step 10. This resulted in a different width or diameter along the thickness of the slot. For example, in the case of the GH, the holes in the silicon nitride layer were measured with an electron microscope to be 100.7 µm in diameter, whereas the ones in the silicon wafer are 106.3 µm wide. On the other hand, the Mo layer was also measured to be thinner than desired, as proven by the resistance measurements done on the finished product, which showed values of around 4 times larger than expected, in the case of the GH. Finally, significant surface roughness was found in the silicon wafer wall, due to the DRIE method used to etch through it. This, as well as the silicon nitride layer protrusion, can be seen in Figure 2.19. These inaccuracies not only affect the thruster performance in terms of the actual thrust provided, but also in the power required to heat up the chip, as well as the overall propulsive efficiency. The lack of a constant width slot, as well as the added surface roughness, can induce more collisions between the propellant particles and the slot walls, leading to undesirable losses in energy and hence exhaust velocity and thrust, and the higher calculated resistance means that more power is needed to heat up the chip to the desired temperature.

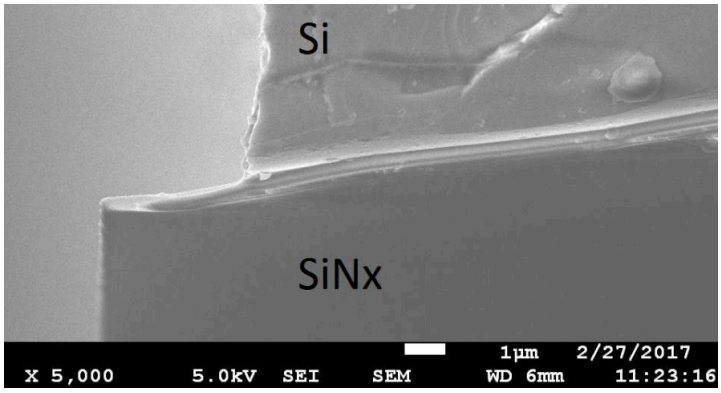

Figure 2.19: Cross sectional view of the produced GLS chips showing the silicon surface roughness and the silicon nitride layer protrusion (Guerrieri, Silva, Zeijl, et al., 2017).

2.5. Micro-propulsion Testing

With the exponential growth of the microsatellite industry over the last couple of decades, the ability to measure thrust levels in the *micro* or even the *nano* scale has become crucial in the development of the novel propulsion systems required by such satellites. Conventional, large scale thrust benches simply lack the necessary accuracy to analyse the operating conditions of such systems, hence specialised facilities shall be developed. As analysed by Ketsdever (2002), the background pressure at which the tests are conducted also affects the characterisation of

the propulsion capabilities of these systems. According to the tests performed, the effect of the background pressure in the measured thrust of such test facilities increases with decreasing thrust, therefore the capacity and dimension of the vacuum chambers used is also of the utmost importance to obtain accurate measurements.

Ketsdever, Lee, and Lilly (2005) performed the first testing campaign of the FMMR concept using several gases as propellant. These tests were conducted in the so-called nano-Newton thrust stand (nNTS), developed by Tew et al. (2000). The nNTS, represented in Figure 2.20, is a torsional thrust stand, supported by two flexure pivots, that measures the linear displacement caused by the thrust force, using a linear variable differential transformer (LVDT), at a known radius from the vertical axis of rotation. This can be related to the angular displacement, which is in turn proportional to the torque about the axis of rotation provided by the thruster. Knowing this torque and the distance from the thruster to the axis of rotation allows for the thrust to be calculated. Due to the low angular displacements expected, a linear relationship is assumed between the measured displacement and the thrust (Ketsdever, 2002). The thrust stand system is calibrated using DSMC results and dampened by an oil bath with a known viscosity and specific gravity. To mimic operational conditions, the test setup was placed in a vacuum chamber capable of maintaining the ambient pressure below 0.0013 Pa.

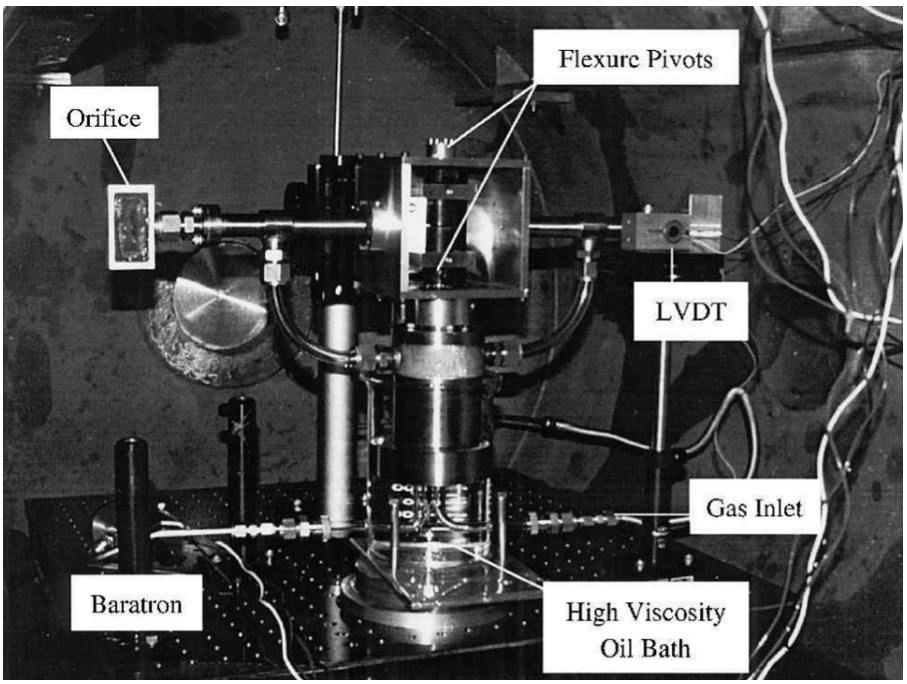

Figure 2.20: The nNTS test stand used by Ketsdever, Lee, and Lilly (2005) to test the first version of the FMMR (Ketsdever, 2002). Note that the thruster is placed in the part labelled 'orifice'.

On the other hand, Guerrieri, Silva, Zeijl, et al. (2017) characterised the propulsion of the LPM using the test stand available at the SpE of the TU Delft. This test stand, called the AE-TB-5m, first designed by Bijster (2014) and later improved by Jansen (2016), consists of a pendulum that indirectly measures the thrust of a system by providing an accurate measurement of the displacement it causes. It is depicted in Figure 2.21. The main calibration procedure required for this test stand therefore consists of obtaining a relationship between force and displacement, which is done using a coil and magnet assembly to generate a known

force on the pendulum and a capacitive displacement sensor to measure its effect. The tests were done by placing the LPM along with the TB-5m stand in the vacuum chamber available at the SpE, keeping the background pressure between 15 and 35 Pa.

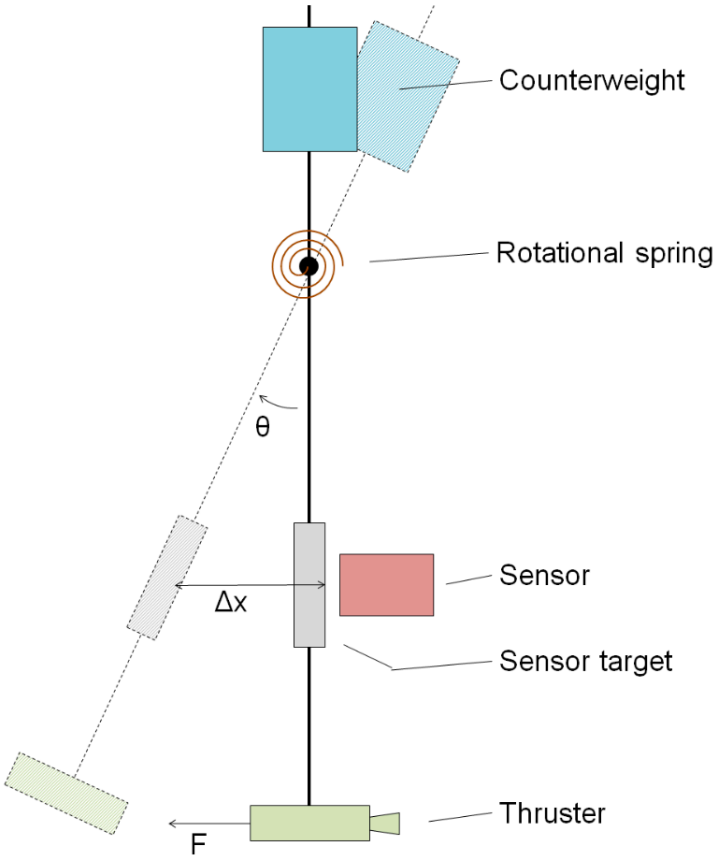

Figure 2.21: Schematic representation of the working principle of the AE-TB-5m test setup (Jansen, 2016). Note that the calibration actuator coil is not depicted here, but is attached to the sensor target.

A further software improvement was implemented by Versteeg (2020), where a digital controller was created that uses the actuator to provide a known force to keep the pendulum at a certain distance from the sensor. When a thruster is attached to the pendulum and is in operation, the force required by the controlled actuator to keep the pendulum distance changes. Since the relationship between the current and the actuator force is well established, the changes in current to maintain equilibrium can be directly related to the thrust provided by the system. This improvement made the previous calibration procedure redundant, as one no longer needs to relate force to displacement and then relate it back to the thruster force, decreasing the overall amount of steps needed to use the AE-TB-5m. This procedural update was validated by Pappadimitriou (2021), who showed <1% difference between the measured thrust using both test stand setups. Applying an active digital damping technique, and performing equipment calibration experimentally, certainly increases the bench's overall measurement accuracy as compared to the setup used by Ketsdever, Lee, and Lilly (2005).

2.6. Conclusions and Research Plan

This chapter has presented a review of the relevant past and current literature on the new micro-resistojet thruster being developed by the TU Delft, the Low Pressure Micro-resistojet, or LPM. The main goal was two-fold: to become acquainted with the underlying theory and to identify any knowledge gaps to be filled during the remainder of this thesis project. To fulfil this objective and to narrow down the scope of the research, five research questions were posed:

Research Questions

- R.Q.1: *What are the main advantages of using the transition flow regime (with Knudsen numbers between 0.1 and 10) as opposed to continuum flow in the micro-resistojet?*
- R.Q.2: *What other green propellant(s) is/are more suitable than water in the current LPM design?*
- R.Q.3: *Is the addition of pressure regulators to such systems needed to ensure constant thrust profiles?*
- R.Q.4: *What are the main MEMS manufacturing technologies that have led the way to the design of the proposed micro-resistojet?*
- R.Q.5: *Given the conclusions arisen from the previous research questions, which research questions and objectives are suitable for the remainder of the thesis duration?*

To answer the research questions, this chapter was divided into five distinct sections. First, Section 2.1 presents a brief historical timeline, from when this system was first theorised by Ketsdever et al. (1998), and called the Free Molecular Micro-Resistojet (FMMR), to the advancements that led to the current state of the LPM, such as those by Guerrieri, Silva, Zeijl, et al. (2017) and Singh (2023). This is followed by Section 2.2, where the molecular gas dynamics theory that explains the working principles of the LPM is laid out. This section also includes a brief introduction into the modelling techniques required to numerically simulate the operating conditions of such systems, as well as a thorough explanation of the analytical models proposed by Ketsdever, Lee, and Lilly (2005) and later improved by Guerrieri et al. (2018b). The choice of the propellant to be used by the LPM, as well as its method of storage are explained in Section 2.3, along with a discussion on the heat transfer and the resistivity of the heater chip. Furthermore, Section 2.4 introduces the MEMS fabrication technologies used for the production of the LPM, as well as a comparison between the manufacturing procedures of Guerrieri, Silva, Zeijl, et al. (2017) and Singh (2023), and a brief overview of the importance of the fabrication accuracy. Finally, the testing facilities used to characterise the performance of the early FMMR and the latest LPM design are described in Section 2.5. The information and discussions presented in these sections paved the way for the research questions to be answered to the highest of standards, as presented below. Please note that the last research question, R.Q.5, is answered in the form of the Research Plan itself, as it was posed for this very same reason, to act as a bridge between the four theory-based questions and the remainder of the thesis project.

- *R.Q.1: What are the main advantages of using the transition flow regime (with Knudsen numbers between 0.1 and 10) as opposed to continuum flow in the micro-resistojet?*

Operating in this flow regime, with Kn numbers ranging from 0.1 to 10, is synonymous to the low-pressure operation of the LPM, as shown by Equation (2.1). There are many advantages of having a propulsion system that can operate at such low pressures, especially when discussing one being designed for a satellite in the *micro* or even the *nano* scale. First and foremost, low pressure operation is directly related low system mass, one of the main requirements, if not the main one, posed on these types of systems. The reduced propellant storage pressure required significantly decreases the tank mass, one of the main dry mass contributors in most propulsion systems. Secondly, the low pressure allows for much more relaxed leakage rate requirements, which are practically negligible. The flexibility with regards to the propellant storage phase is also a consequence of choosing this flow regime, as the thruster can operate under the propellant's vapour pressure by being stored as either a liquid or a solid. Furthermore, the LPM does not need convergent-divergent nozzle geometries to expand and accelerate the propellant particles. In this size scale, nozzle throats are more prone to blockage and are much harder to manufacture than straight expansion channels. Furthermore, Ketsdever, Clabough, et al. (2005) showed that at low Reynolds number operation, which is the case, nozzles do not offer significantly different propulsive efficiencies when compared to expansion slots. Last but not least, as explained in Lafferty (1998), the flow in the transitional regime will always be laminar. This typically means a more precise flow control and lower power usage, all of which are advantageous. (Ketsdever et al., 1998) (Ketsdever, Lee, & Lilly, 2005)

- *R.Q.2: What other green propellant(s) is/are more suitable than water in the current LPM design?*

There are two ways in which the answer to this question can be discussed: theory and simulation based or in terms of design feasibility. Out of the more than 90 different fluids considered by Guerrieri, Silva, Cervone, and Gill (2017), and discussed in Section 2.3, when selecting the best propellant for the LPM, there was one that stood out along with water: ammonia. Given that the simulation results presented in said research were based on an assumed set of constant values and dimensions, and that the two propellants came extremely close in terms of I_{sp}, it is not too far-fetched to consider that ammonia can indeed be better than water in terms of performance for a different set of characteristic values. On the other hand, given the need for miniaturisation, there is no other green propellant other than water that comes close in terms of the applied ΔV per unit volume. So, in terms of the theory and simulated performance, the only other green propellant that can compete with water is likely to be ammonia.

In terms of design feasibility, the reasoning is completely different. As described throughout this literature review, there are two different designs in terms of propellant storage: to store it as a liquid, or as a solid. This currently represents the biggest challenge towards this system's implementation, as put by Cervone et al. (2015). Keeping the water propellant in its liquid state may lead to complications related to sloshing and higher plenum pressures than desired, more of which will be discussed in the following research question. On the other hand, freezing the water propellant after launch is practically impossible due to the strict low pressure requirements. Doing so prior to launch is unfeasible due to water's physical characteristics. Again, a large amount of power would be needed to keep the water frozen from ground integration to launch, which could mean a decent number of days. Therefore, in terms of feasibility, the answer depends on the final propellant storage system design. If the problems arisen due to storing it as a liquid are addressed and accepted, water is definitely the most

viable option. However, if it is decided to store the propellant as a solid, the design could be made simpler and hence more feasible by choosing a green propellant that can easily be kept frozen on ground, with a melting point higher than water, that does not require extra power to remain in that state (Cervone et al., 2015).

R.Q.3: Is the addition of pressure regulators to such systems needed to ensure constant thrust profiles?

The need for regulating the pressure within the LPM will ultimately depend on the final selection of the propellant storage phase, which has not yet been done, as well as on the experimental results from further sublimation and evaporation research. If the water propellant is to be stored as a solid, there is a smaller chance that the system would need any kind of pressure regulation device. Water, in its solid state, has a low vapour pressure (around 600 Pa at 0°C) and the preliminary results from the experimental campaign on water ice sublimation ran by Maxence et al. (2017) show that equilibrium can be reached at low enough pressures to negate the need for regulation, by carefully controlling the conditions within the tank. On the other hand, the vapour pressure of liquid water is much higher (1210 Pa at 10°C). This means that the evaporation will reach an equilibrium at a higher pressure than desired to remain within the wanted Kn number range, and hence some means of pressure regulation will likely be needed to step down the gas pressure between the storage system and the plenum. Of course, this is also vastly dependent on future evaporation tests, as it may be the case that equilibrium is reached at a lower pressure than theory predicts. A final trade-off must therefore be done to select the propellant storage phase between two options with several pros and cons. Storing the water as a solid likely negates the need for a typically complex pressure regulation device, however requires more power to freeze the water in orbit (following the discussion in the previous answer) and keep it frozen. On the other hand, doing so as a liquid relaxes the power requirement, however increases the system's complexity due to the likely necessity for pressure regulation and may also introduce propellant sloshing issues.

Generally speaking, pressure regulation within micro-satellite propulsion systems is done by operating the valves within the feed system in a pulsed manner, as conventional pressure regulator designs do not comply with the strict mass and volume requirements. Depending on the final propellant storage choice and future sublimation and evaporation testing campaigns, more research shall be done on micro-valves capable of the desired pulsed operation. A testing campaign with the valves currently owned by the SpE would certainly go a long way towards the LPM's implementation in future micro-satellites. In any case, propellant storage is certainly the most important constraint preventing the current LPM design from flight-readiness. Furthermore, the addition of pressure regulation requirements will certainly increase the complexity of the system being designed, which is not ideal.

R.Q.4: What are the main MEMS manufacturing technologies that have led the way to the design of the proposed micro-resistojet?

Upon reviewing the LPM designs by Guerrieri, Silva, Zeijl, et al. (2017) and Singh (2023), it is clear that all three main types of MEMS fabrication processes described in Section 2.4 are equally important. In terms of bulk micromachining, the proposed LPM design procedure relies on several wet etching steps. These wet etching processes, using specific chemical baths, are mostly used to create the desired resistance geometries and to remove the appropriate photoresist layers. When it comes to surface micromachining, several chemical vapour deposition

steps are required to fabricate the proposed heater chips, such as the deposition of the silicon nitride isolation layer. Two types are used: LPCVD and PECVD. Finally, in order to create the slots/channels, the most typical HAR technique is used, DRIE, which accelerates a gas plasma onto the wafer, etching its surface to the desired depth.

Manufacturing inaccuracies are inherently present at the machines in the EKL due to constant use and possible contamination. Because of this, most machines have a logbook in which users must write down their process times for the required actions. This is done such that future users can calculate the process times required for their desired outcome. For example, a PECVD machine initially required 15 seconds to deposit a 300 nm layer of TEOS. After some time, users report in the logbook that the same layer thickness took 18 seconds to be deposed. Future users can use this data to calculate their process times, which of course leads to a new set of inaccuracies. These shall be judged by performing a complete mechanical and electrical characterisation of the new heater chips.

2.6.1. Research Plan

As mentioned in the introduction of this chapter, the research plan stems from R.Q.5, which was posed to link the answers from R.Q.1 through R.Q.4 to the objectives of the remaining months of the thesis project. A research objective is hence posed for the plan, followed by a main research question to fulfil said objective, and a number of sub-questions to aid in the same effort. The proposed work is divided into several work packages, which include a set of tasks, as well as the expected time frame for their completion.

Assuming that the manufacturing of the LPM heater chip proposed by Singh (2023) is completed in due time, the thesis project will focus on the complete mechanical, electrical, and propulsive characterisation of the new thrusters. The research objective can hence be posed as follows, as well as the main research question that comes with it:

Research Objective #1

To characterise the newest version of the TU Delft LPM in terms of its mechanical, electrical, and propulsive performance by developing an appropriate thruster interface and performing the necessary testing efforts.

Research Question #1

How have the recent changes done to the design and manufacturing procedure of the TU Delft LPM affect its mechanical, electrical, and propulsive characteristics?

To aid in the completion of the above research objective, a number of sub-goals are defined as follows:

1. To design and manufacture a prototype thruster interface to house the LPM heater chip and provide the appropriate electrical and mechanical connections.
2. To perform a complete mechanical charaterisation of the newly manufactured LPM heater chips.
3. To perform a complete electrical charaterisation of the newly manufactured LPM heater

chips.

4. To perform a complete propulsion characterisation of the newly manufactured LPM heater chips in near-operational conditions using nitrogen gas and water vapour as propellant.

Four sub-questions can be explored to achieve the above sub-goals:

- R.Q.1: How can a suitable interface be designed to aid in the propulsive characterisation of the LPM and to be used in the Delfi-PQ flight demonstration?
- R.Q.2: How accurately have the new LPM chips been manufactured?
- R.Q.3: How have the changes made to the LPM's fabrication procedure affected its electrical characteristics?
- R.Q.4: How have the changes made to the LPM's fabrication procedure affected its propulsion capabilities in near-operational conditions?

The completion of the above objectives and research plans is divided into five distinct work packages. Each work package is given a duration and a set of tasks to be done for its completion. A work breakdown structure (WBS) of this first research plan is seen below:

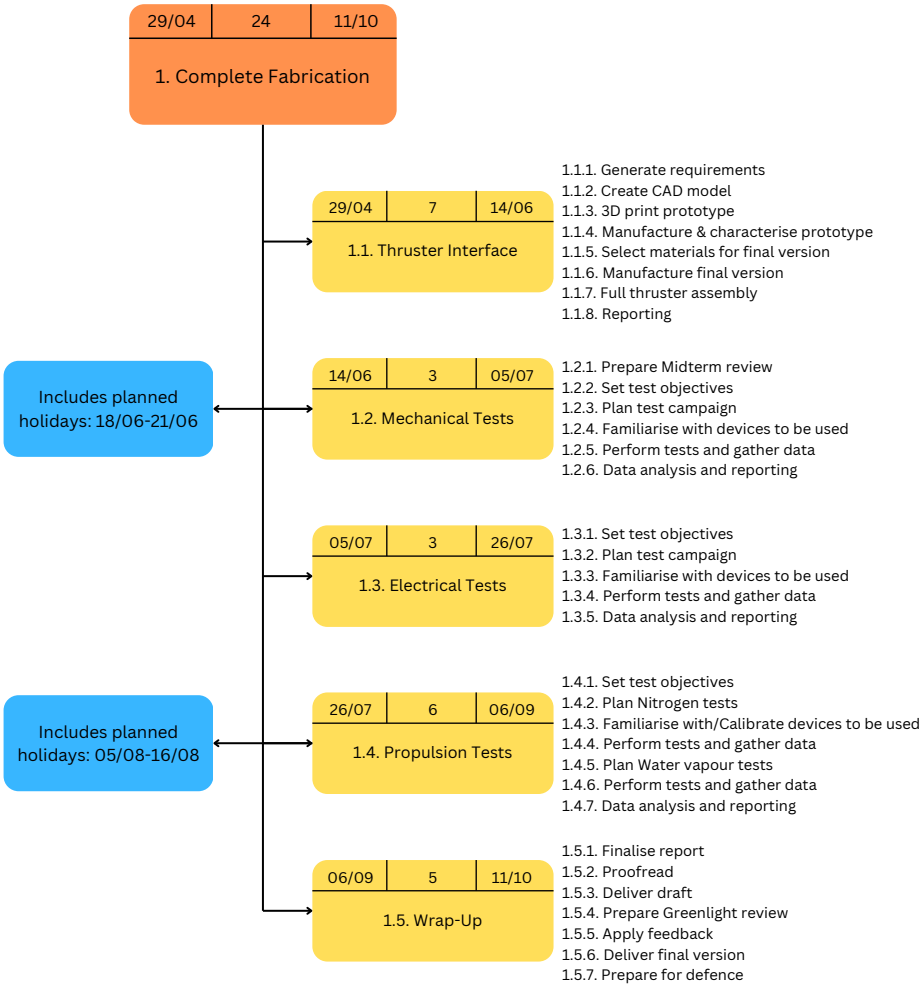

Figure 2.22: WBS of Research Plan #1. Note that the top left and right corners represent the expected start and end dates of the work package, respectively, and the duration in number of weeks is given in the middle.

3

LPM Thruster Interface

As mentioned in the research plan above, the first step towards the completion of the objectives set for this thesis involves designing, prototyping, and manufacturing the first engineering model of the LPM interface with its final application in mind. Several other LPM interfaces have previously been designed by other Masters students at the TU Delft. However, these were done solely for testing purposes, entirely disregarding the thruster's final application. The LPM is to be demonstrated in the next iteration of the Delfi-PQ satellite being developed by the TU Delft, hence the requirements for its interface shall stem from the upper level satellite propulsion system requirements, as reported by Pallichadath (2018).

This chapter begins with a short description of the target satellite, as well as its propulsion system requirements, in Section 3.1. This is followed by Section 3.2, where the first stage of any design project is present: generation of requirements. The design and assembly of the interface prototype, manufactured using 3D printed parts, is then seen in Section 3.3. Lastly, the final design, as well as the requirement compliance matrix and an explanation of the design choices that lead to the LPM's new electrical connections, are shown in Section 3.4.

3.1. Delfi-PQ Propulsion System

The Delfi-PQ, hereafter called the DPQ, is a 3-unit (3P) PocketQube being designed by the TU Delft as a response to the industry's increasingly competitive miniature satellite market. PocketQubes are characterised by a form factor of 5x5x5 cm, 8 times smaller in volume than the established CubeSat standard, and a mass of no more than 250 grams per unit, putting them in the *pico*-satellite range (Guo, 2022). The main goal is to reduce the development costs and time even further when compared to CubeSats, and to ensure continuous bus and payload innovation by students by following an iterative design concept, focusing on the desired technology demonstrations, rather than on specific missions (Speretta et al., 2016).

The DPQ Propulsion Payload Demonstrator (PPD), shown in Figure 3.1, consists of two micropropulsion systems, both relying on MEMS technology: the LPM being investigated in this report, as well as the Vaporizing Liquid Micro-resistojet (VLM), being worked on in tandem by fellow Masters student Andrei Pârvulescu. The design of the PPD was performed by Turmaine (2018), and later verified by Melaika (2019) by means of test and analysis. The

requirements currently set for the PPD are shown in Table 3.1 below.

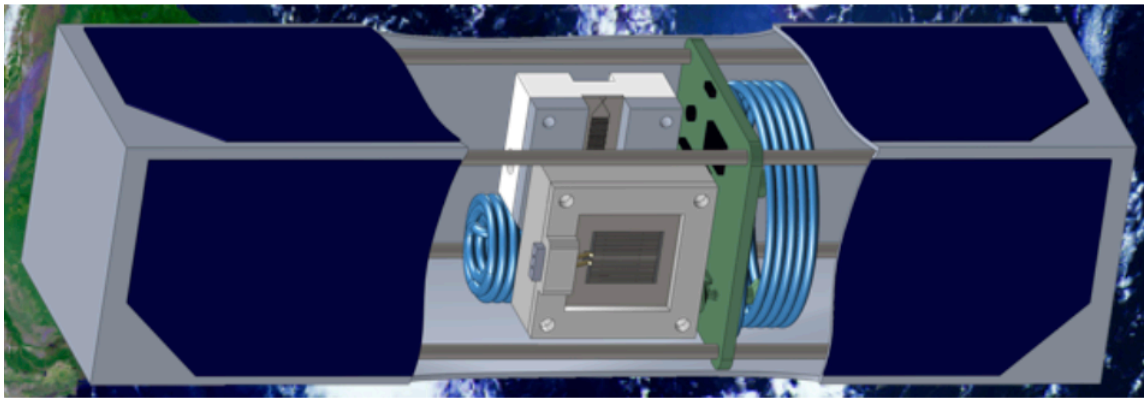

Figure 3.1: Render of the DPQ satellite showing the PPD with both thrusters in the middle unit (Melaika, 2019).

Table 3.1: Summary of the requirements for the DPQ propulsion system (Pallichadath, 2018). Note that requirements that are not fully complete (i.e. including "To Be Completed (TBD)"), as well as ones that sit outside of the scope of the research objectives described above, are excluded.

Requirement ID	**Description**
	System
PROP-SYST-100	The total wet mass of the propulsion system at launch shall be not higher than 75 g.
PROP-SYST-200	The total size of the propulsion system shall be within 42 mm x 42 mm x 30 mm (including thrusters, valves, electronics board, harness, connectors & propellant storage tube).
PROP-SYST-300	The peak power consumption of the propulsion system during ignition or heating shall be not higher than 4 W.
PROP-SYST-500	The critical mission lifetime of the propulsion system shall be equal to at least 3 months.
	Performance
PROP-PERF-200	The thrust provided by the propulsion system shall be 3 mN as a maximum.
PROP-PERF-210	The thrust provided by the propulsion system shall be at least 0.12 mN.
PROP-PERF-400	The micro-propulsion system shall operate on a single unregulated supply voltage of 3 [VDC] to 4.1 [VDC].
	Functional
PROP-FUN-200	The thruster shall be able to operate on gaseous N2, as well as on liquid H2O.

PROP-FUN-700	The Micropropulsion system shall allow for the mounting of electronic sensing devices for the measurements of propellant temperature and pressure inside the tank, temperature and pressure measurements, IMU measurements (accelerometers & gyroscopes), Voltage Monitoring/ Current monitoring/ Temperature Measurement.
	Interface
PROP-INT-300	The propulsion system shall be electrically connected to the satellite power subsystem through the standard RS-485 interface.
	RAMS
PROP-RAMS-200	The internal pressure of all propulsion system components shall not be higher than 10 bar.
PROP-RAMS-310	Materials used in the thruster shall be compatible with liquid demineralized water in both liquid and vapour state, nitrogen gas and air.
PROP-RAMS-320	Materials used in the propulsion system shall not be toxic, flammable, or in any way potentially hazardous for the operators or the other satellite subsystems.

3.2. Interface Requirements

As mentioned in the introduction of this chapter, the interface for the LPM thruster shall be designed following the requirements for the DPQ propulsion system, shown in Table 3.1. This is not only done as the LPM is expected to be demonstrated in DPQ's next flight, but also because the requirements for a PocketQube are most likely the most constraining of all other types of satellite, hence it is expected that the designed LPM interface also complies with requirements on larger CubeSat models that could eventually require a propulsion system such as the LPM.

Noting that the requirements seen in Table 3.1 apply to the propulsion system as a whole, which includes both the VLM and the LPM thrusters, as well as the propellant tanks and feed system, a new set of requirements, specific to the LPM, must first be formulated and reasoned. These requirements, shown in Table 3.2, stem from the general DPQ requirements, as well as from the choices made by students that previously worked on the detailed design of the DPQ propulsion subsystem and payload (Turmaine, 2018)(Melaika, 2019). These choices include the exact dimensions for the LPM interface, the chosen sensors, feed systems, tubing sizes and interfaces, and so forth.

Table 3.2: List of requirements generated for the design of the LPM interface.

Requirement ID	Description	Rationale
	General	
PROP-INT-LPM-G-001	The interface shall have a maximum volume of 20x20x10 mm.	As per requirements set by Pallichadath (2018) and Melaika (2019).
PROP-INT-LPM-G-002	The interface shall allow for pressure and temperature measurements inside the plenum.	As per PROP-FUN-700 from Pallichadath (2018). The selected pressure sensor to be used in the DPQ thrusters is the TE Connectivity HCLA12X5DU, as chosen by Melaika (2019). Temperature is expected to be controlled using the measured resistance of the heater chip, as per Subsection 2.3.3.
PROP-INT-LPM-G-003	The interface shall include a 0.138-40 UNF-2B threaded inlet for propellant feeding.	Interface used by all 062 MINSTAC parts (The Lee Company), chosen by Turmaine (2018) and used by Melaika (2019).
PROP-INT-LPM-G-004	The interface shall allow for the new heater chips to be tested using the AE-TB-5m test bench at the SpE of the TU Delft.	A second interface is required to attach the LPM interface to the test bench via an M4 screw.
PROP-INT-LPM-G-005	The engineering model of the interface shall be fabricated out of Teflon.	Regardless of the possibility of interface deformations and leaks at high temperatures, teflon is the best material in terms of thermal insulation available at the DEMO workshop. Keeping in mind the main goal of this thesis is to test the new LPM chips, this material is deemed more than sufficient to fulfil the research objectives.
	Performance	
PROP-INT-LPM-PER-001	The interface shall withstand a maximum plenum pressure of 450 Pa.	The maximum plenum pressure allowed to remain in the transitional flow regime (Guerrieri et al., 2018a) including a safety margin of 1.5.
PROP-INT-LPM-PER-002	The interface shall withstand a maximum temperature of 500 K.	Based on the reported melting operating temperature of Teflon (*Teflon PTFE Properties Handbook*, n.d.).

3.3. Prototype Design & Assembly

Following the requirements stated above, this section presents the design and assembly procedure of the prototype for the engineering model of the LPM interface, which will be fabricated with poly-lactic acid (PLA) using the available 3D printers at the Delft Aerospace Structures and Materials Lab (DASML). This material has inferior thermal qualities as compared to teflon, however is a good step to perform the necessary fitting and volume tests on the interface prototype. After performing the appropriate fitting and volume tests, the final engineering-model will be fabricated by DEMO, as explained in Section 3.4.

Given the volume requirement set above, it is clear that the plenum of this new interface will be much smaller than its predecessors. Previously built interfaces by Guerrieri, Silva, Zeijl, et al. (2017), Figure 2.6, and Melaika (2019), Figure 3.2, were almost twice as big in terms of volume, having a plenum with about the same dimensions as required here for the entire interface. Nonetheless, Singh (2023) performed some CFD simulations using the COMSOL software to analyse the effect of the plenum size on the thrust. The thrust of the LPM using two different plenum heights of 14 and 4 mm was simulated, and the results showed that a decreasing plenum height does not affect the operational conditions of the LPM to an unacceptable extent. More specifically, both the simulated thrust and average molecular flux, which can be directly related to the mass flow, showed a maximum decrease of 1% in all simulations performed. The plenum height for the newly designed interface is 6 mm as mentioned below, and hence this difference is expected to be even lower than 1%, which is deemed acceptable at this stage in the thruster's design life cycle.

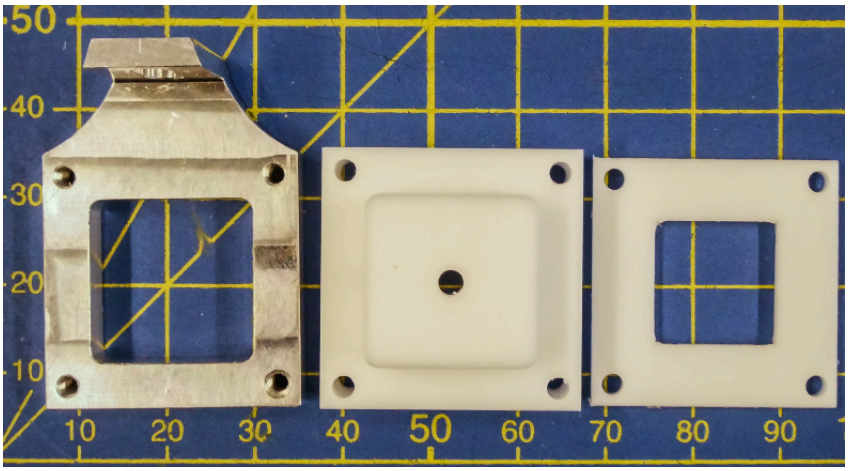

Figure 3.2: LPM interface version designed and built by Melaika (2019) for solenoid valve testing.

The interface was designed using a computer-aided design (CAD) software, namely Fusion360 from Autodesk. The design is made up of two distinct parts: a bigger bottom part, containing the required propellant inlet, pressure port and chip slot, and a smaller front cover to hold the chip, as well as the electrical connections in place. The two parts, made of Teflon, are joined by four M2 screws, one in each corner. The original idea was to glue both parts after the chip

is inserted, in order to comply with PROP-INT-LPM-G-001. However, due to the extreme difficulty in gluing two Teflon parts to each other, it was decided to add the screws. This does mean that the requirement is not met, however, the increase in volume is almost negligible, and it also means a more modular design in which the same interface can be used to test several chips. Considering the short budget for manufacturing, this last point outweighs the fact that the volume requirement is not met.

In terms of the electrical interface, the first version of the CAD design included a slot big enough to hold a 2-pin header, as done by Guerrieri, Silva, Zeijl, et al. (2017). However, after consultation with Dr. van Zeijl from EKL, it was decided that a 4-pin header would be ideal such that 2 pins could be used to provide power, and the other two to measure the chip's resistance. Measuring the resistance using the same pins where the current is supplied from induces a large error, mostly due to the contact resistance of the connectors themselves and the lead resistance. The voltage drop caused by this cannot be measured using 2 pins, and hence neither can the aforementioned change in resistance. By using two different pins in contact with the contact pads to measure the resistance, these measurement errors can be drastically decreased, a so-called 4 point measurement. Essentially, this setup allows for a resistance measurement solely based on the voltage drop caused by the resistor itself (i.e. what we are interested in) rather than the entire circuit. The electrical pin slot is the thinnest section of the interface and is likely to be the first to slightly deform at higher temperatures, and possibly lead to leakages. This is one of the reasons why the hole on top cover is designed to be the same size of the chip active area. This design choice allows for the entire perimeter of the top cover to sit on top of at least 2 mm of inactive chip area, holding it firmly against its slot on the bottom box and hence preventing leakages.

The features present in the interface, shown in Figure 3.3 and displayed in Appendix A, are summarised as follows. Note that the engineering drawings shown in Appendix A include a few microns of tolerance added upon consultation with DEMO prior to fabrication.

A bottom, 20x20x7.5 mm box-shaped part containing:

- A 3.51 mm diameter hole on the bottom plate acting as the inlet, complying with requirement PROP-INT-LPM-G-001.
- A 15x13 mm slot for the LPM chip to be placed. The chip dimensions programmed into the wafer stepper by Dr. Henk van Zeijl are 15x13 mm, such that enough space is left for chip mounting as well as maintaining the integrity of the interface walls.
- A 2 mm whole acting as the pressure sensor port, complying with PROP-INT-LPM-G-002.
- A 13x10x6 mm plenum.
- Four M2 holes, one on each corner, to attach the top cover and thrust bench interface.

A top, 20x20x2.5 mm top cover including:

- Four M2 holes, one on each corner, to attach to the bottom part.
- A 13x10 mm whole in the center allowing the heated propellant to escape.
- A 10x2.5 mm slot for the electrical connection to the heater chip.

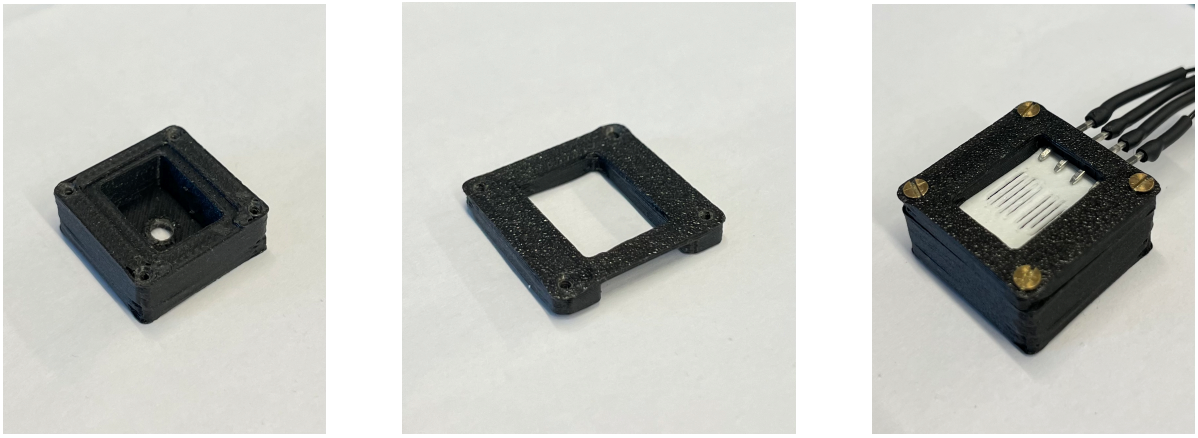

(a) Bottom part. **(b)** Top cover. **(c)** Assembled interface.

Figure 3.3: 3D printed parts of the LPM interface prototype.

Lastly, a second interface is needed to attach the LPM interface to the test bench that will be used in the propulsive characterisation of the new chips. As mentioned in Chapter 2, the test bench available to measure the thrust values predicted for the LPM is called the AE-TB-5m. The attachment between test bench and the system to be tested is done via a single M4 threaded hole. The design is based on the previous test bench interface produced by Melaika (2019), shown on the left of Figure 3.2. However, in order to reduce the protrusion of the propellant inlet into the plenum, as per Figure 3.4, effectively decreasing its size, the decision was made to have the inlet go through this second interface as well. The final design prototype is shown in Figure 3.5 and in Appendix A, including the characteristics described below.

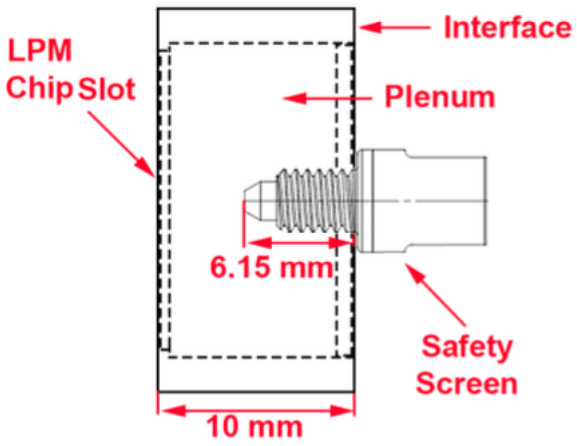

Figure 3.4: Side view of the plenum of the LPM showing the estimated protrusion of the threaded part of the INMX0350000A safety screen used as the propellant inlet (Melaika, 2019).

- Four M2 threaded holes in the corners to connect the LPM interface.
- One .138-40 UNF-2B (3.505 mm diameter) threaded hole in the bottom plate acting as the inlet, complying with requirement PROP-INT-LPM-G-003.
- One perpendicularly placed M4 hole to attach the LPM interface to the test bench.

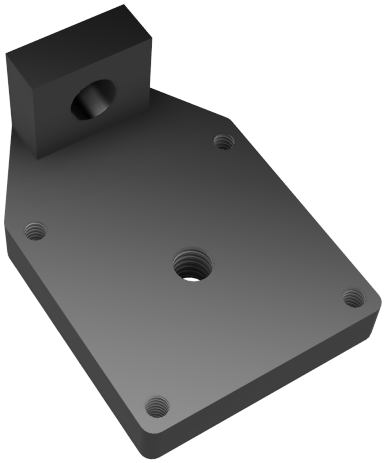

Figure 3.5: Render of the thrust bench interface. Note that the LPM interface is to be attached on the back side of this image.

3.4. Engineering Model Assembly

After finalising the design stage of the interface, the CAD models were sent to DEMO for manufacturing. The final version of the manufactured interface can be seen in Figure 3.6. As per PROP-INT-LPM-G-005, the LPM interface was fabricated using Teflon. On the other hand, Aluminium (Al) was used for the test bench interface. This is because Al is a much stronger material which allows for the LPM interface to be more tightly secured to the AE-TB-5m thrust bench. The advantage of this is that undesirable moments can be avoided and the thrust direction can be kept perpendicular to the pendulum axis at all times, ensuring all the thrust provided by the LPM is translated into pendulum rotation, hence increasing the reliability of the thrust tests.

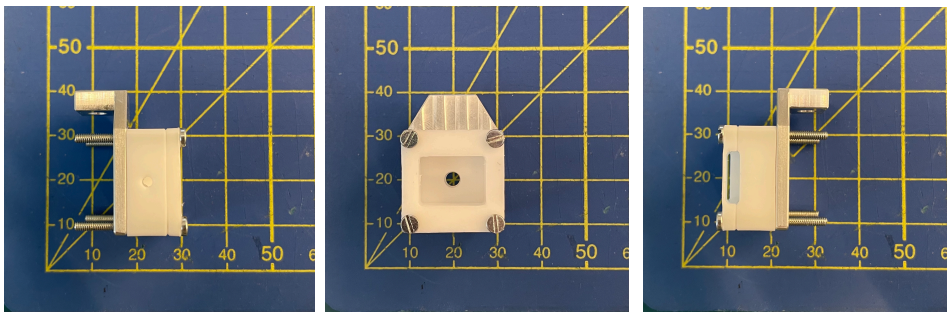

(a) Left view **(b)** Top view **(c)** Right view

Figure 3.6: Manufactured LPM interface showing the pressure sensor port (a), the inlet port (b) and the electrical connection slot (c).

The electrical connection was clearly something to be improved upon with regards to the interface designed by Guerrieri, Silva, Zeijl, et al. (2017). The pins were simply placed on top of the chips creating an electrical connection by contact, making it extremely delicate. Three methods to update this connection were hence considered, namely gluing the pins to

the chip with a conductive glue, wire-bonding the chip contact pads to a PCB, or soldering the pins to gold pads that were previously glued to the chip using the same conductive glue. The three tested versions can be seen in Figures 3.7 and 3.8. Upon testing the three versions, it was observed that the gold pads were extremely small and very hard to solder the pins to, whereas the PCB option required further design (i.e. of the PCB itself), highly constrained by the interface volume requirement. Hence, in the absence of time and with design simplicity in mind, the first option was chosen to move forward with: gluing the pins to the contact pads of the chips using the Loctite ABLEBOLD 84-1LMI conductive glue (Loctite, 2014). This glue does however pose a constraint on the maximum operating temperature of the chips, as it was proved to fail at around 150 °C by Pappadimitriou (2021). In terms of outgassing, both NASA ASTM E595, (ASTM International, 2021) and ESA ECSS-Q-ST-70-02C (European Cooperation for Space Standardisation (ECSS), 2008) requirement standards are satisfied.

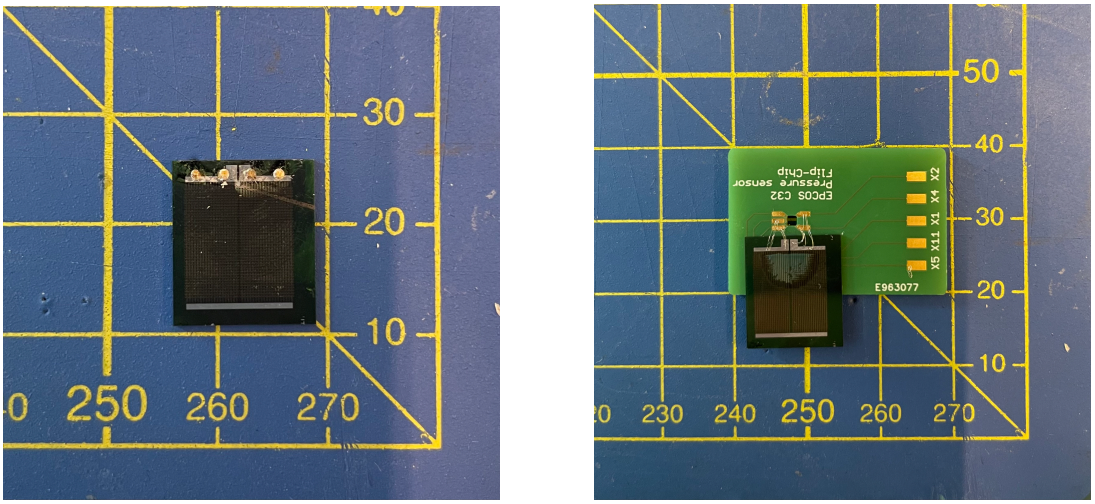

(a) Gold pads **(b)** Printed circuit board (PCB)

Figure 3.7: Discarded versions of the new electrical connections for the LPM chip.

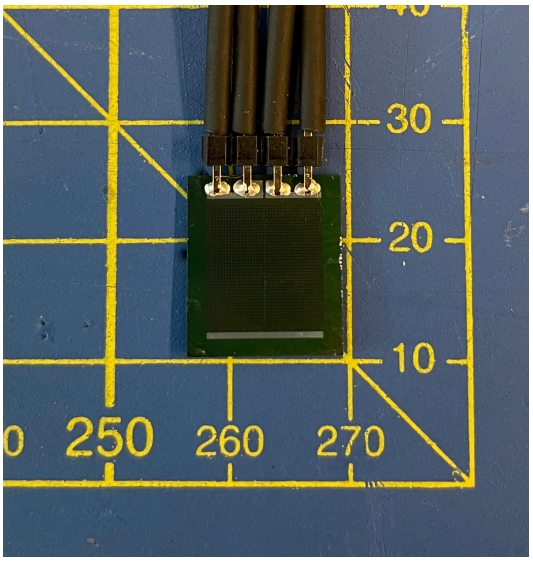

Figure 3.8: Glued electrical connection

The final versions of the assembled interface, for the cold gas thruster and the resistojet setups, are shown in Figures 3.9a and 3.9b. Keep in mind that these figures show the same thruster interface, the only difference being the presence of the electrical connection. Thus, only one interface was manufactured by DEMO. The two thruster versions weigh a total of 7.13 $\pm$ 0.002 g and 7.36 $\pm$ 0.003 g, respectively, the difference coming from the electrical connection shown in Figure 3.9b. As seen in Table 3.3, the new interface complies with most requirements set prior to its design. Only two requirements are not complied with: PROP-INT-LPM-G-001, which relates to the final interface volume, and PROP-INT-LPM-PER-002, relating to the maximum operating temperature of the interface. The former is not complied with mainly due to the fact that Teflon had to be used to manufacture it. Teflon is notoriously hard to glue, hence screws had to be used to hold the two parts of the interface together, as mentioned previously. In the future flight model, it is expected that other materials such as ceramics are used, enabling bonding and finally complying with this requirement. The latter requirement was marked as "not complied" due to the lack of validation. A preliminary analysis was performed using the COMSOL Multiphysics platform, however the results could not be validated with experiments due to the low maximum operating temperature of the conductive glue. Nevertheless, the simulation using COMSOL, shown in Figure 3.10, merely considering the heat transfer through solids and a chip temperature of 500 K for 10 s does seem to prove that the Teflon material would withstand these temperatures. This can be considered a worst case scenario, as in reality the propellant flow would act as an insulator and help dissipate heat over the interface. Note that the simulation does not show any possible deformations in the teflon material, which are expected to occur prior to melting by examining the interfaces produced by Guerrieri, Silva, Zeijl, et al. (2017) and Melaika (2019), and hence should definitely be improved upon.

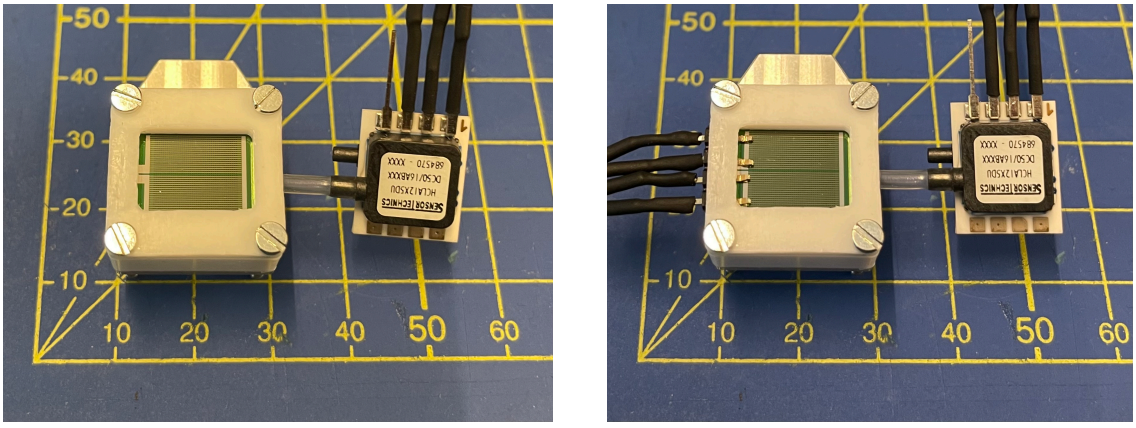

(a) Cold gas thruster version.

(b) Resistojet thruster version.

Figure 3.9: Final assembled LPM interface versions.

Table 3.3: List of requirements generated for the design of the LPM interface.

Requirement ID	Description	Compliance (Y/N)	Rationale
	General		
PROP-INT-LPM-G-001	The interface shall have a maximum volume of 20x20x10 mm.	N	Use of screws and electrical pins increase the volume of the designed interface.
PROP-INT-LPM-G-002	The interface shall allow for pressure and temperature measurements inside the plenum.	Y	Hole on the left wall allows HCLA12X5DU sensor to be connected, Figure 3.6a.
PROP-INT-LPM-G-003	The interface shall include a 0.138-40 UNF-2B threaded inlet for propellant feeding.	Y	0.138-40 UNF-2B threaded hole present in bottom wall, Figure 3.6b.
PROP-INT-LPM-G-004	The interface shall allow for the new heater chips to be tested using the AE-TB-5m test bench at the SpE of the TU Delft.	Y	Aluminium piece contains M4 hole to be attached to the test bench, Figure 4.8.
PROP-INT-LPM-G-005	The engineering model of the interface shall be fabricated out of Teflon.	Y	Interface indeed fabricated using Teflon. Deformation possibility is avoided by setting a maximum testing temperature of 140°C. Furthermore, the parts with the thinnest profiles, and hence more likely to deform, are not likely to lead to leaks due to the location of the chips inside the interface.
	Performance		
PROP-INT-LPM-PER-001	The interface shall withstand a maximum plenum pressure of 450 Pa.	Y	Pressures of over 600 Pa were reached while performing the plenum pressure tests described in Subsection 4.2.5.

PROP-INT-LPM-PER-002	The interface shall withstand a maximum temperature of 500K.	N	Not verified due to maximum operating temperature of conductive glue.

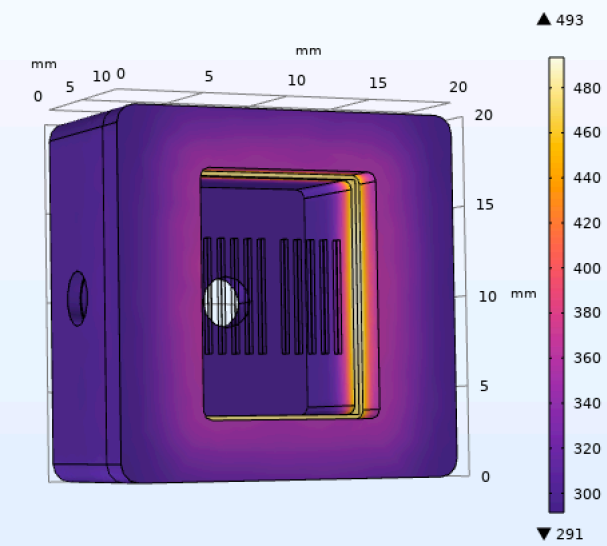

Figure 3.10: Simulation of the temperature profile of a Teflon interface with a 500 K chip for a duration of 10 s. Note that this can be considered as a worst case scenario, as no gas is flowing and absorbing the heat from the chip.

4

Experimental Campaign Plan

In this chapter, all experiments to be performed on the new LPM chips, with the exception of the mechanical tests, as these are considered as mere measurements, are introduced and explained. Starting with the electrical characterisation tests, in Section 4.1, and ending with the thrust tests, in Section 4.2, this chapter provides a complete description of the procedures, setups and success parameters to ensure that future students and faculty members can reproduce the experiments performed to further validate the design of the new chips and interface.

4.1. Electrical Tests

In order to fulfil the third research objective posed in Chapter 2, the electrical characteristics of the new LPM chips must be thoroughly analysed. As mentioned in that same chapter, the chips are to have a secondary purpose apart from producing thrust: to act as temperature sensors. For this purpose to be fulfilled, the TCR of the chips must first be found with the highest accuracy possible. This represents the main goal of the electrical characterisation of the LPM chips. A short explanation of the procedure to achieve this was given in Chapter 2, but it will be revisited below. A secondary goal, yet equally important, is to obtain a relation between power and chip temperature to facilitate future LPM operation.

The temperature T of the heater chip can be related at all times to its resistance R via Equation (4.1) below, where the subscript 0 identifies their values at room temperature and β is the temperature coefficient of resistance, or TCR. Hence, for the chip to act as a temperature sensor as well, its resistance at room temperature, as well as the TCR, must be known.

$$\beta = \frac{R - R_0}{R_0(T - T_0)} \tag{4.1}$$

Two different experiments arise from the previous statement: one to measure the room temperature resistance R_0, which is henceforth known as TEST-ELEC-01 and another one to find the TCR β, TEST-ELEC-02.

4.1.1. TEST-ELEC-01 - Resistance at Room Temperature

As explained above, the first test of the electrical characterisation campaign of the new LPM chips is to measure the resistance of the two types of chips at room temperature. Even though the design of the resistance is the same for both types of chips, it is still good practice to characterise both types separately. This is a relatively simple test in principle, requiring only a multimeter with its wiring, and the chips themselves. However, as mentioned in Section 3.3, the design of the electrical connection has been changed as opposed to the interface fabricated by Guerrieri, Silva, Zeijl, et al. (2017) in order to obtain more accurate measurements. TEST-ELEC-01 will therefore be performed using both configurations, to characterise the effect of this design change.

The first the test consists of measuring the resistance using 2 of the pins, as done by previous researchers. This is easily done by attaching the wires to two banana plugs and plugging them into the Hewlett-Packard 34401A digital multimeter (DMM) in the correct resistance measurement ports. The multimeter will show a value for the resistance, without taking into account any voltage drops caused by the wires and contacts in the circuit. The second test will be performed using all four pins, to perform the so-called 4-point measurement. Using the same DMM, the 4-point measurement mode is selected, and the other 2 wires are connected to the 4-point measurement sensing ports. These two extra wires will essentially only measure the voltage drop caused by the heater. The resistance measurement will be much more accurate than the previous design, however, due to the layout of the resistances on the chip, many will be measured in parallel, leaving even more room for improvement. The two types of measurements can be represented by Figure 4.1 below. Three thrusters of each type will be tested. The main reason for this is that, at this stage of the project, only three chips of each type were already glue to the electrical pins. Furthermore, a more representative result of the wafers is obtained if more than one chip of each is tested. The resistance of all other chips of the same type is assumed to be within the uncertainty of the calculated average. The resulting room temperature resistances are given in Subsection 5.2.1.

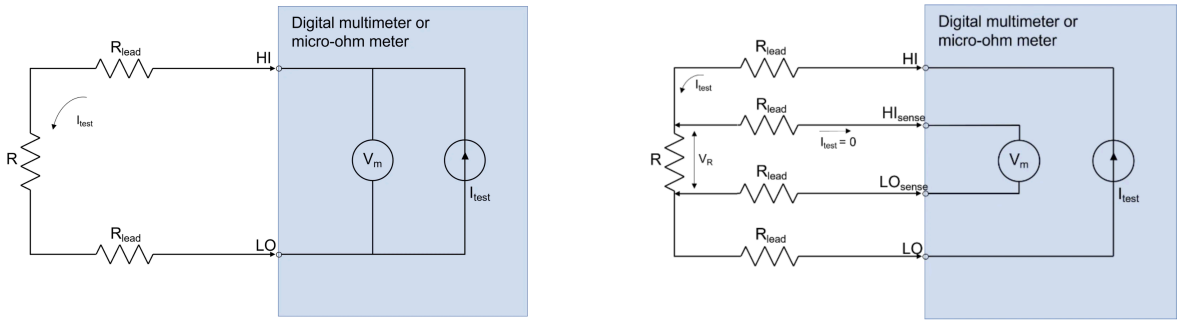

(a) 2-point measurement.

(b) 4-point measurement.

Figure 4.1: Electrical diagrams[1] of 2-point and 4- point resistance measurements, where R is the resistance being measured (i.e. the chip in this case).

[1] URL:https://www.keysight.com/blogs/en/tech/bench/2022/06/14/how-to-use-a-digital-multimeter [Accessed on 16/07/2024]

Table 4.1: List of components and equipment required to perform TEST-ELEC-01.

Name	Amount	Rationale
GSS/GH chips	3	To measure the resistance of 3 chips of each type.
Banana plug	4	To connect the LPM wires to the DMM.
Hewlett-Packard 34401A DMM	1	To measure the resistance of the chip at room temperature. Stated accuracy of 0.01% of the reading (Keysight, 2022).

4.1.2. TEST-ELEC-02 - TCR

As its name describes, this second electrical test campaign consists of finding the TCR of the chips as accurately as possible, such that the chips themselves can be used as temperature sensors in the later thrust tests. As mentioned in the introduction of this section, a secondary goal is to obtain power-temperature relations for the chips, to further facilitate the temperature control and chip operation in the future.

The original plan consisted of using an IR camera, placed above the chips, to measure their temperature and relate it to the measured resistance using Equation (4.1). However, due to the low emissivity of the chips (highly polished surface), the accuracy of the temperature readings using the IR camera is not high enough. More specifically, the IR radiation of the camera itself would reflect on the chip surface and be added to the chip temperature output. As the camera started to heat up more and more as it was being used, this offset was not constant in time and rather difficult to predict. To solve this issue and hence simplify the experiment, as opposed to using the IR camera, thermocouples are placed directly in contact with the chips to measure their temperature. Due to the design of the resistor lines and the direction of the current flow, the temperature is not constant over the entire active area of the chips. To take this effect into account and measure the average temperature over the chip, three thermocouples are hence used: one closer to the centre of the chip and one of each side.

The control variable for this experiment is the current provided to the chips via the two electrical pins in the middle of the 4-pin header. An automatic control is implemented to increase the provided current from 0 to 0.5 A in steps of 0.1 A, every 30 seconds, giving enough time for the provided PSU current and chip temperature to settle. This current limit is chosen as it lead to a temperature close to the maximum operating temperature of the conductive glue described in Section 3.4. To calculate the resistance of the chips, the voltage drop across them is measured using the two outer leads. This is done by connecting them to two analogue inputs via a breakout board (BoB), which in turn is connected to a NI PCI-6229 DAQ card inside the PC. With the chips inside the vacuum chamber, the connection of the two outer leads to the BoB is done via one of the five D-sub9 connectors taped to the left side of the chamber. The output of the D-sub9, from which the leads are connected to the BoB, sits outside of the chamber. The voltage drop is calculated as the difference between the voltages sensed by each outer lead,

and hence resistance is calculated using the provided current and the aforementioned voltage drop. The materials needed to perform this experiment are given in Table 4.2 below.

The test is performed three times with the initial thermocouple positions, shown in Figure 4.2a. To analyse the effect of changing the thermocouple positions on the experimental TCR value found, the test is performed three more times with the thermocouples positioned as per Figure 4.2b, leading to six sets of data for each type of chip. Each dataset is plotted with resistance on the Y-axis and temperature on the X-axis in Subsection 5.2.2. The slope of the linear trend line is used to calculate β, by dividing it with the room temperature resistance values found using the procedure explained in the preceding section. One chip of each type is tested for the initial thermocouple positions, and another chip of the same type is used for the secondary positions. It is assumed that the TCR for all other chips belonging to the same type lie within the calculated uncertainty of the result.

Table 4.2: List of components and equipment required to perform TEST-ELEC-02.

Name	**Amount**	**Rationale**
GSS/GH chip	2	To measure the TCR of the 2 types of chips.
Delta Elektronika SM-7020-D	1	To provide the desired control current to the chips. Has a programming accuracy in constant current mode of 0.5% (Hutten, 2021).
CR computer	1	To control the power supply and read the thermocouple values and analogue voltage inputs.
K-type thermocouples	3	To measure the temperature at various points on the chips. Has an accuracy of $\pm$2.2 K of 0.75% of the measurement (Hutten, 2021). The 2.2 K is leading in this case.
NI 9211 DAQ	1	Acquires data from thermocouples and sends it to PC. Adds an error of $\pm$2.5 K to each measurement (Hutten, 2021).
NI CB-68LP BoB	1	Allows for connection between analogue inputs/outputs and DAQ device on PC.
NI PCI-6229 DAQ Card	1	Allows for required data to be read by the cleanroom PC

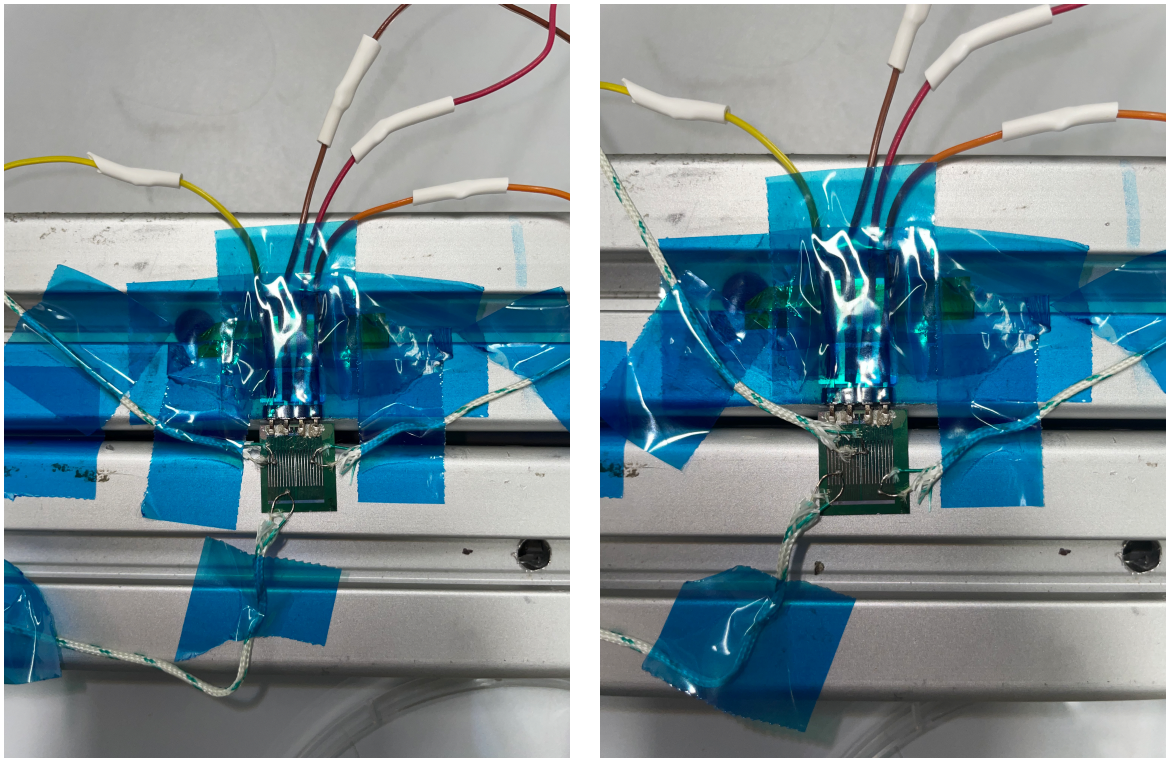

(a) Positions for the first test run.

(b) Positions for the second test run

Figure 4.2: Thermocouple (white and green wiring) positions for the two tests performed on the thruster chips (green). Note that the same two positions are used for the tests using the GH chip.

4.2. Thrust Tests

As mentioned several times before, the thrust obtained by the LPM chips is the most important outcome of this report. The aim of this propulsion characterisation is to not only analyse the ability of the LPM to work as a resistojet, but also as a simple cold gas thruster, in case its application requires it to work without any power.

As explained in Chapter 2, the test bench that will be used to perform these tests is the AE-TB-5m. A more detailed description of this test bench, as well as the procedures required to calibrate it, are given in Subsections 4.2.1 through 4.2.3. The gas feed system used at the SpE department cleanroom to perform the required thrust tests, called the general purpose feed system (GPFS) is then described in Subsection 4.2.4. This is followed by Subsection 4.2.5, where the procedure followed to understand how to control the pressure in the LPM plenum is found. Finally, the cold thrust tests, as well as the resistojet tests, are explained in Subsections 4.2.6 and 4.2.7, respectively. Note that, due to lack of time, the resistojet tests were not performed in the end, however their procedure is still explained here for future reference.

4.2.1. Thrust Bench Setup

The AE-TB-5m thrust bench was briefly discussed in Section 2.5, however it will be revisited here in more detail. Designed by Bijster (2014) and later improved by Jansen (2016) and Versteeg (2020), the AE-TB-5m is a pendulum-based thrust bench capable of measuring a thrust

range of 0-5 mN. It consists of a hanging pendulum to which the thruster is attached at the bottom. The pendulum hangs on near-frictionless hinges and provides indirect measurements of thrust by measuring displacements from its equilibrium position, caused by the force provided by the attached thruster. The original design is represented by Figure 2.21.

To obtain the desired thrust values, the relationship between force and pendulum displacement, the displacement sensor sensitivity S_d must be known as accurately as possible. For this very same reason, a magnetic actuator was attached to the sensor target by Jansen (2016). Prior to thrust testing, the thrust bench is calibrated by providing a known force F_{mag} with the actuator and measuring the resulting displacement Δd, allowing the aforementioned force-displacement relationship to be obtained. Another calibration procedure is hence needed to first find the relationship between the current applied to the actuator coil and the force it generates, the so-called coil sensitivity S_c. As a way to streamline the thrust measurement process, Versteeg (2020) came up with a way to essentially skip the calibration process relating force with displacement. By implementing a discrete time PID controller to keep the pendulum at a set distance from the sensor during testing, the thrust provided by the attached thruster can be directly related to the change in actuator current needed to maintain the set position. This way, the thrust can be calculated by simply knowing the relationship between current and force of the actuator, the coil sensitivity S_c. This method is known as the force compensation method.

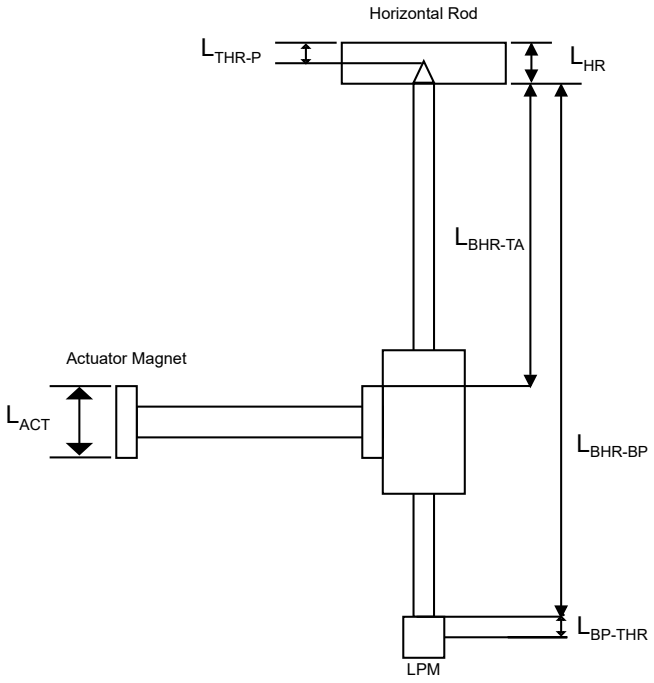

Figure 4.3: Simplified diagram of the thrust bench showing the distances that need to be measured to find the force conversion factor. A description of the different lengths can be found in Table 6.1.

Last but not least, one must take into account the different positions of the actuator and the

thruster with regards to the pendulum pivot, as depicted in Figure 4.3. The moment arm of the force produced by the actuator to keep it at a set distance from the sensor, L_{act}, is different than that of the force produced by the thruster, L_{thr}. In order to calculate the thrust force using the method mentioned above, which is done assuming both moments cancel out, a conversion factor, λ, is needed (Versteeg, 2020):

$$F_{thr}L_{thr} = F_{act}L_{act} \tag{4.2}$$

$$F_{thr} = F_{act}\frac{L_{act}}{L_{thr}} = F_{act}\lambda \tag{4.3}$$

Due to the difficulty in measuring L_{act} and L_{thr} directly, they are found indirectly by breaking them down into smaller, easily measurable lengths, as shown in Figure 4.3 and explained in Table 4.3 below. This is mainly done because, for example, it is more accurate to measure the entire length of the actuator L_{act} and then halve it, than guessing where this half is and directly placing the caliper/ruler there. The smaller lengths are measured using vernier calipers with an accuracy $\pm$ 0.02 mm[1], however, L_{BHR-BP} is measured using a ruler with a least count of half a millimetre, for which is accuracy is assumed to be $\pm$ 0.25 mm. L_{BP-THR} is measured from the final interface. Finally, L_{act} and L_{thr} are calculated using Equations (4.4) and (4.5), respectively. This test is named TEST-CAL-01 for future reference.

Table 4.3: Description of the different lengths to be measured to find the force conversion factor.

Name	Description
L_{TR-P}	Top of horizontal rod to pendulum pivot point.
L_{HR}	Thickness of horizontal rod.
L_{BHR-TA}	Bottom of horizontal rod to top of actuator magnet.
L_{MAG}	Length of actuator magnet.
L_{BHR-BP}	Bottom of horizontal rod to bottom of pendulum arm.
L_{BP-THR}	Bottom of pendulum arm to centre of thruster interface.

$$L_{act} = L_{HR} - L_{TR-P} + L_{BHR-TA} + \frac{L_{MAG}}{2} \tag{4.4}$$

$$L_{thr} = L_{HR} - L_{TR-P} + L_{BHR-BP} + L_{BP-THR} \tag{4.5}$$

By knowing the conversion factor and the displacement sensor sensitivity S_d, the thrust force produced by the thruster can be calculated with the displacement method using Equation (4.6),

[1]https://www.reidsupply.com/en-us/industry-news/dial-vs-digital-vs-vernier-calipers

where Δd is the displacement measured by the sensor. If the force compensation method is preferred, Equation (4.7) can be used.

$$F_{thr} = S_d \cdot \lambda \cdot \Delta d \tag{4.6}$$

$$F_{thr} = S_c \cdot \lambda \cdot \Delta I \tag{4.7}$$

4.2.2. TEST-CAL-02 - Magnetic Actuator Calibration

Throughout the years, the actuator coil has been moved around quite often as it is also used by other test benches at the SpE. As it has been put together and taken apart so many times, it was decided to calibrate it again as its sensitivity S_c (i.e. the relation between current and force) may have changed over time, given that its last calibration was performed in 2021 (Versteeg, 2020)(Pappadimitriou, 2021). The calibration will be performed following the same procedure as done by the aforementioned students, using the equipment described in Table 4.4.

Table 4.4: List of components and equipment required to perform TEST-CAL-01.

Name	Amount	Rationale
CR computer	1	To run the LabView code and perform the experiment.
VTDC	1	Actuator to be calibrated
AG245 High Precision Mettler Toledo scale	1	To measure the force exerted by the coil on the magnet due to a current input.
Delta Elektronica SM-7020-D	1	To supply the current to the VTDC. Has a programming accuracy in constant current mode of 0.5% (Hutten, 2021).

The magnet arm is placed on the scale and a bubble level is used to ensure the arm is perfectly in a vertical position. The setup can be seen in Figure 4.4 below. The coil is then connected to a power source that increases the current from 0 to 10 A in steps of 0.25 A, controlled by a LabView program. The current flowing through the coil produces a magnetic force on the magnet arm, which can be calculated by multiplying the mass value seen on the scale by the acceleration due to gravity (i.e. 9.80665 m/s^2). A 15 second pause is applied between each step increase to give the balance time to settle and for the mass to be recorded as accurately as possible. A linear regression line is then applied to the data, and its slope gives the desired sensitivity S_c in mN/A. In this case, since the same PSU will be used to power the actuator during thrust testing, the PSU uncertainty is discarded as the combination of PSU and actuator is now calibrated as a whole, hence only its repeatability is of importance (Versteeg, 2020). The uncertainty of the resulting sensitivity will hence be given as the standard deviation of the average of all tests performed. The results are analysed in Subsection 6.1.2.

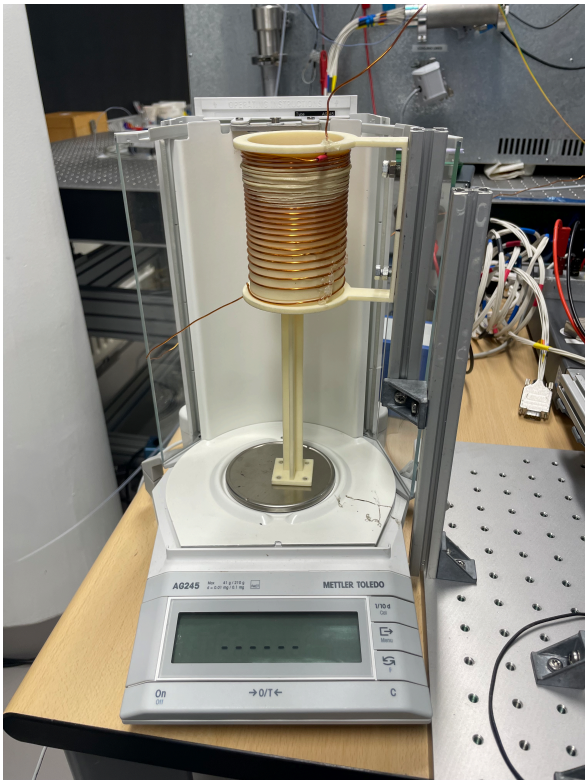

Figure 4.4: Coil setup on the Mettler Toledo high precision scale.

4.2.3. TEST-CAL-03 - Displacement Sensor Calibration

The displacement sensor used in the AE-TB-5m test bench is the CS2 capacitive displacement sensor by Micro-Epsilon, with a measurement range of 0-2 mm (Micro-Epsilon, 2015). The data acquisition is done via the DT-6220 demodulator, also by Micro-Epsilon, connected to the PC via an Ethernet cable. Regardless of the fact that this sensor has been extensively calibrated by previous students, it is always good practice to perform the calibration procedures again prior to testing, specially if they take such little effort. As mentioned in Subsection 4.2.1, the displacement sensor sensitivity (i.e. the relation between force and displacement) must be known as accurately as possible to increase the reliability of the thrust measurements. The procedure followed by Pappadimitriou (2021) will be used for this experiment, requiring the equipment described in Table 4.5 below.

Table 4.5: List of components and equipment required to perform TEST-CAL-02.

Name	Amount	Rationale
CR computer	1	To run the LabView code and perform the experiment.
VTDC	1	To generate known force.
Delta Elektronica SM-7020-D PSU	1	To supply the current to the VTDC. Has a programming accuracy in constant current mode of 0.5% (Hutten, 2021).

CS2 Capacitive Displacement Sensor	1	To be calibrated. Along with the demodulator, an accuracy of 5.02 µm is found (Makhan, 2018).
DT-6220 Demodulator	1	To read data from displacement sensor and feed it to PC.
AE-TB-5m Test Bench	1	To be calibrated along with the sensor.
LPM interface with chip	1	To approximate the pendulum conditions during the thrust testing.
Propellant tubing	-	To calibrate sensor with same displacement perturbations as observed during thrust tests.

First, the displacement at the pendulum's equilibrium position is noted. The SM-7020-D PSU is then used to supply an increasing current from 0 - 2.5 A to the actuator, in 10 steps, causing a certain pendulum displacement from the equilibrium position. These current increases are done at a rate of 50 mA/s to avoid excessive pendulum oscillations. At every step increase in current, the displacement is allowed to stabilise, arriving at a relationship between current and displacement. This relationship, in A/µm, is converted into the displacement sensor sensitivity S_d, in mN/µm, by multiplying it with the actuator sensitivity S_c, in mN/A, found by following the procedure described in the above section. The uncertainty in the sensor sensitivity is again given as the standard deviation from the resulting average of the three performed tests. In order to mimic the pendulum dynamics during the thrust tests and arrive at representative results for the sensor sensitivity, the same setup is used as shown in Subsection 4.2.6.

4.2.4. General Purpose Feed System

A general purpose feed system (GPFS) will be used to supply the required N2 gas to the test setup inside the vacuum chamber. As seen in Figure 4.5, the feed system components are connected to a vertical board attached to a wheeled cart for easier relocation. The N2 bottle sits behind said vertical board. As the valve on top of the N2 gas bottle is opened, the high-pressure gas (0-200 bar) flows towards the high pressure shut-off valve. This is followed by a high pressure gauge, used to monitor the gas pressure inside the N2 cylinder, and a pressure regulator that lowers the gas pressure to the desired feed system value, displayed in the low pressure gauge. The low pressure gas then flows through a low pressure shut-off valve towards one of three distinct branches, selected by the user via the yellow selection valves. Finally, a Brooks 5850S mass flow sensor and controller is installed at the end of the branch being used, after which the gas is fed into the vacuum chamber via a series of tubes and quick-connection fittings.

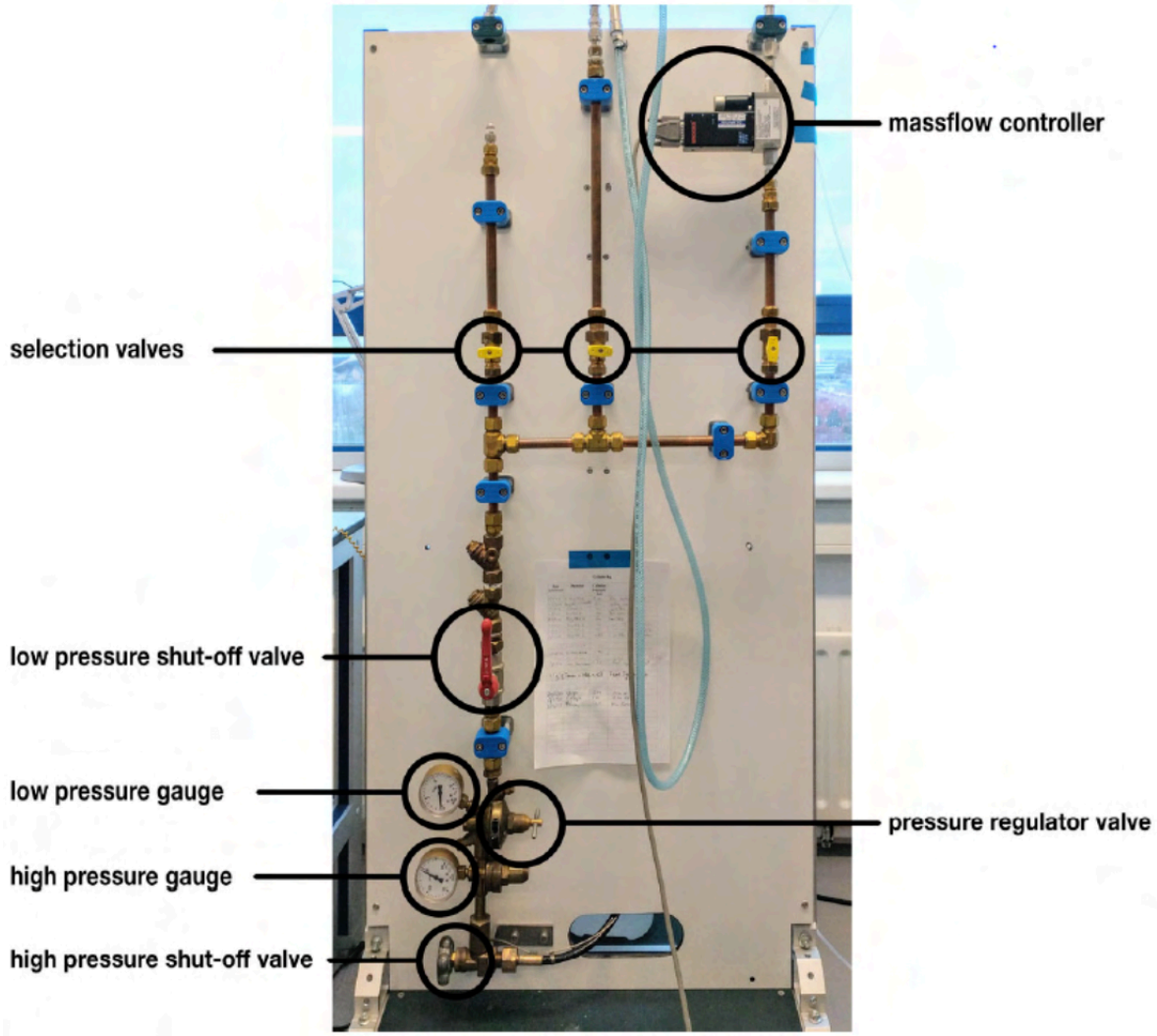

Figure 4.5: GPFS board used for thrust testing at the SpE (Hutten, 2021).

4.2.5. TEST-PRE-01 - Plenum Pressure Control

As mentioned several times throughout this report, the LPM is expected to operate at plenum pressures ranging from 50 to 300 Pa. The units of the pressure regulator valve used in the GPFS are [bar], where 1 bar equals 100000 Pa, hence some means of regulating the propellant pressure before reaching the plenum is certainly needed. This can be done in two ways using the available equipment at the SpE department: using a mass flow controller or operating the solenoid valve via a PWM signal. However, the available Brooks 5850S mass flow controller used in the feed system does not produce mass flow values which are stable enough (Makhan, 2018), hence there is really only one valid option, the solenoid valve.

The valve that has been extensively used and tested at the SpE is the normally closed, 2-way INKX0514300A solenoid valve by The Lee Company. The IECX0501350AA control module was purchased along with the valve, to provide the required spike (24 V) and hold (3.2 V) voltage to operate it. As concluded by Silvestrini (2017), implementing the PWM signal via the PC did not produce a stable signal as the timing of operations depends on the current CPU

load, leading to an unstable duty cycle, regardless of whether it is manually changed or not by the user. The control module is therefore controlled via an Arduino board that generates the PWM signal, in which its duty cycle (DC) is stable and is controlled via LabVIEW. However, after years of usage and poor documentation, it is currently unknown which code is uploaded into the Arduino board, and it is impossible to retrieve. Furthermore, as two more students are using the CR facilities for testing similar devices concurrently, it was instructed not to change anything regarding this setup. This meant that the pressure control implemented by Guerrieri, Silva, Zeijl, et al. (2017) and Melaika (2019) could not be used, as different Arduino codes were used to control not only the valve, but also the pressure sensors, as well as updating the DC after every control loop. There is hence no other choice but to try to achieve stable plenum pressures by controlling the PWM via LabVIEW directly, regardless of the conclusions found by Silvestrini (2017).

The ambient pressure for all tests is chosen to be 25 Pa, a compromise between real world applicability and the time it takes for the pump to achieve the desired ambient pressure after every test. The same ambient pressure is required for all tests as the HCLA12X5DU pressure sensor provides differential pressure measurements, hence the results for which duty cycle leads to which plenum pressure are only valid, within a certain accuracy, for the same ambient pressure. A range of duty cycles is tested to know which duty cycle leads to which plenum pressure, to be used later in the thrust tests. The valve is left open until the ambient pressure in the chamber increases by 5 Pa. This is because the same pressure increase threshold will be used for the thrust tests, the reasons for which are explained in the next section. The equipment needed to perform this test is the same as for the cold thrust tests explained below, with the exception of the AE-TB-5m test bench, which is not required. The fluidic setup inside the vacuum chamber is shown in Figure 4.6.

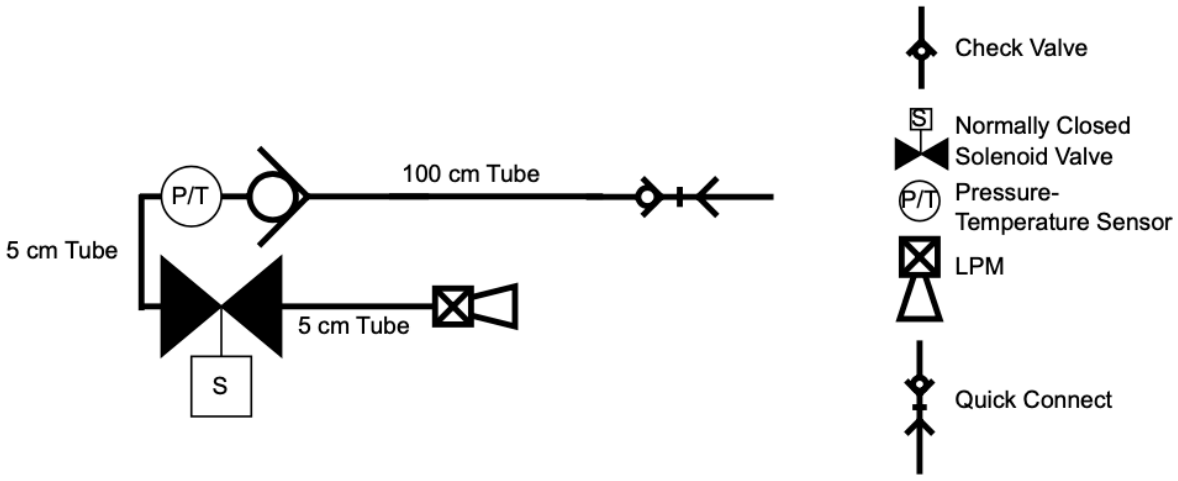

Figure 4.6: Fluidic diagram of the feed system setup used for the plenum pressure control tests.

4.2.6. TEST-THR-01 - Cold Gas Testing

Part of the propulsion characterisation of the LPM consists of testing its ability to operate purely as a cold gas thruster, that is, without applying any power to the chip. This is an

inherently simpler test, as no temperature/power control is needed, however almost equally important. As mentioned several times throughout this report, the power consumption of the target satellites is always one of the toughest requirements. The ability of a propulsion system to operate using virtually zero power, except for its solenoid valve, is therefore quite significant considering its desired application.

The AE-TB-5m test bench, which has been previously calibrated following the procedures described in the preceding sections, is used for these tests, as well as all other components mentioned in Table 4.6 below. The tests are performed using three different background pressures: 20, 25, and 30 pascals. The Vacuubrand RZ6 pump is capable of achieving even lower pressures, however a compromise had to be made between approximating vacuum conditions and the time it takes to get there. Five different plenum pressures are tested, from 100 to 300 Pa, where the lower limit stems from the minimum displacement that can be discerned from the test bench pendulum, whereas the higher limit comes from the threshold between transitional and slip-flow regimes (i.e. around 280 Pa according to Guerrieri, Silva, Zeijl, et al. (2017)). To show repeatability and hence increase the reliability of the results, the tests will be repeated once using the exact same conditions (i.e. pendulum equilibrium point and supply gas pressure), and once more using a different equilibrium point, to ensure the thrust is not affected by this. It would've been useful to further prove repeatability by performing even more tests, however time constraints did not allow this to happen. Since the vacuum chamber used has a fairly small area, the background pressure increases quite rapidly as the propellant is expelled from the LPM. For all tests, once the desired background pressure is reached, the solenoid valve is left open until the pressure increases by 5 Pa, after which it is closed and the pendulum is allowed to return to its equilibrium point. The main reason for this choice of a 5 Pa threshold comes from the fact that the only other experiment campaign performed on the LPM, albeit on another type of chip, used the same value. For comparison, it was decided that the same value would be the most suitable. Furthermore, it is noticed that the time it takes for the 5 Pa threshold to be met is just enough for the mass flow meter to stabilise, without increasing the time it took for two consecutive tests to be performed too much (i.e. the time it takes for the pump to bring back the desired background pressure). Using the analytical model described in Chapter 2, the maximum thrust difference that could be caused by this 5 Pa difference in background pressure is calculated to be 4%, which is concluded to be small enough during this preliminary thrust testing phase. The tests will be performed using both the displacement and the force compensation methods, using Equations (4.6) and (4.7), respectively. To take into account possible equilibrium errors (i.e. zero errors), the change in displacement caused by the LPM is calculated as d_1 - (d_0 + d_2)/2, where d_0 and d_2 represent the average displacements before and after the thrust period, and d_1 the average displacement while the valve is open. The same can be said for the change in current ΔI, when analysing the results according to the force compensation method.

Table 4.6: List of components and equipment required to perform TEST-THR-01.

Name	Amount	Rationale
CR computer	1	To run the LabView codes and perform the experiment.
GSS/GH chip	2	LPM chips to be investigated.

LPM interface	1	To provide the required mechanical connection between the chips and the test bench.
AE-TB-5m test bench	1	To measure the thrust produced by the LPM.
VTDC	1	To keep the pendulum at the chosen equilibrium distance while performing force compensation thrust tests.
HCLA12X5DU Pressure Sensor	1	To measure the pressure inside the interface plenum.
CB-68LP BoB (channels 0-15)	1	To provide required excitation voltage and to acquire the voltage output from the HCLA12X5DU sensor as well as the current output from the SM-7020-D PSU.
RedBearLab Blend Micro v1.0	1	Arduino board to control the solenoid valve control module.
IECX0501350AA Control Module	1	To control the power to the valve.
Delta Elektronica D-030-10	1	To provide required hold voltage to the valve.
Delta Elektronica E-030-10	1	To provide required spike voltage to the valve.
Delta Elektronica SM-7020-D	1	To provide the required current to the VTDC.
INKX0514300A solenoid valve	1	To control the flow of propellant towards the plenum.
TUTC3216910D-A 1 m 062MINSTAC tube	1	To carry propellant from the check valve to the LPM interface.
TKLA3201112H 062MINSTAC Check Valve	1	To connect the 5 cm and the 1 m tubes, as they both have male connections.
TUTC4012905L-A 5 cm 062MINSTAC tube	2	One is part of the MS5832-30BA interface, another between the solenoid valve and the check valve to enlarge the length of the feed system.
MS5837-30BA Pressure Sensor	1	To measure the incoming gas pressure and temperature.
NI USB-6008	1	To provide required excitation voltage to MS5837-30BA sensor.
NI USB-8451 DAQ	1	To acquire data from the MS5837-30BA sensor.
Brooks 5850S Mass Flow Controller	1	To measure the mass flow of N2 gas being fed to the thruster

Heraeus Vacutherm	1	Vacuum oven available in the CR.
Vacuubrand VSP 3000	1	To measure the ambient pressure inside the vacuum chamber.
Vacuubrand RZ6 Rotary Vane Pump	1	To remove the air from the vacuum chamber and decrease the ambient pressure inside.

The fluidic setup inside the vacuum chamber used for all experiments was updated with respect to the one presented above following the results of the same test. As observed in Figure 4.7, the pressure interface designed by Melaika (2019) is now the most upstream component of the setup, connected to the vacuum chamber quick disconnect via a 5 cm tube (TUTC4012905L-A). This pressure interface, fitted with an MS5837-30BA pressure sensor, is used to measure the incoming N2 flow conditions (i.e. pressure and temperature). The INKX0514300A solenoid valve is fitted directly to the other side of the pressure interface, followed by another 5 cm tube and the TKLA3201112H check valve, both used to extend the length of the feed system. Finally, the 1 m tube (TUTC3216910D-A) connects the check valve and the LPM interface. As seen in Figure 4.8, this tube is taped to the pendulum arm, looped around and taped again to the top of the pendulum, to prevent any unwanted oscillations due to the propellant feed pressure during testing. The same procedure is done for the electrical wiring belonging to the HCLA12X5DU sensor.

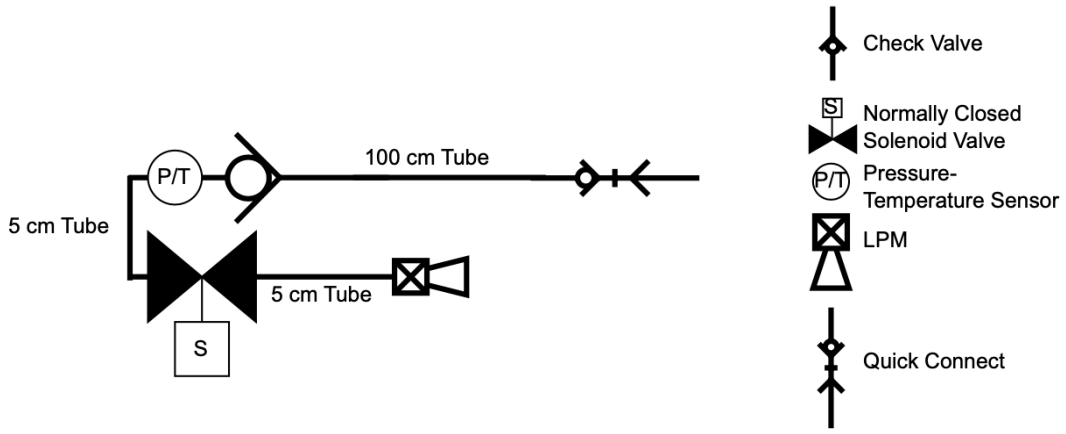

Figure 4.7: Fluidic diagram of the second and final version of the feed system used for plenum pressure control and thrust tests.

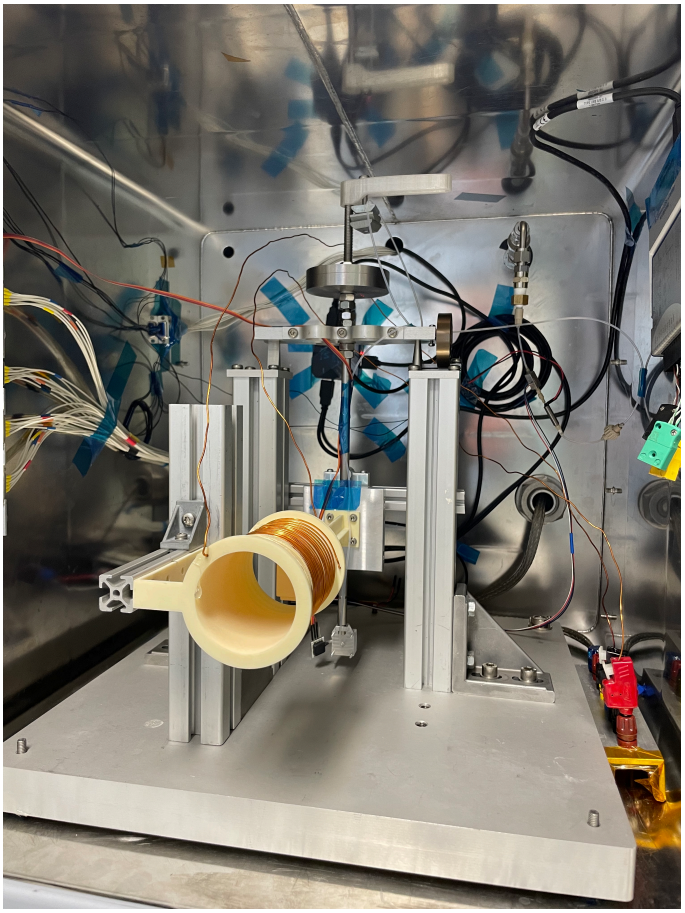

Figure 4.8: Test setup for the cold thrust test campaign (TEST-THR-01)

4.2.7. TEST-THR-02 - Resistojet

The resistojet tests are performed in a similar manner as the cold gas tests, however with the added difficulty of connecting the chips to a power supply and controlling their temperature by using the TCR found from TEST-ELEC-02 and actively measuring their resistance. In terms of components, equipment, and fluidic setup, Table 4.6 and Figure 4.7 can also be used, with two small changes and/or additions. First, as discussed in the results analysis of the cold gas test campaign, the VTDC is no longer needed as the force compensation method can no longer be used. The SM-7020-D that was used to power it is hence now used to provide the required power to the chips, by connecting the two inner leads seen in Figure 3.8 and Figure 3.9b to the appropriate banana plugs inside the chamber (i.e. ports 6 and 7 as of the writing of this report). Furthermore, the CB-68LP BoB is given another function: to actively measure the voltage drop across the outer leads of chips, the connection of which is done via one of the D-sub9 connectors inside the chamber, as explained in Subsection 4.1.2.

In terms of background pressures, plenum pressures, and amount of tests, no changes are planned with respect to the cold gas test campaign described in the preceding section. As mentioned above, the only change in the test procedure comes from the required temperature control of the chips, for which the results from the electrical characterisation (i.e. TEST-ELEC-01 and TEST-ELEC-02) will be used. The results showed that the GH chip was calibrated as a

temperature sensor for the temperature range of 40-140 °C. The GSS was concluded to require further testing in terms of electrical characterisation and should hence not be used for this test, for now. Upon completing the test setup, as seen in Figure 4.8, the current supplied to the chip is slowly increased until the desired temperature is calculated according to the results of the electrical characterisation. Once this temperature is reached, the valve is opened until the background pressure increases by 5 Pa, after which it is closed and the pendulum is allowed to go back to its equilibrium position.

4.3. Overview of Proposed Tests

As its name implies, this section simply serves as an overview of the tests that will be performed throughout the duration of this thesis. For future reference, the LabVIEW files (.vi) used for the tests, located in the cleanroom PC (E:\Gabriel_Teixeira), are also named.

Table 4.7: Overview of all tests to be performed during this project, including the LabVIEW file used in each case.

Test Name	File Name	Description
TEST-ELEC-01	N/A	Measure the room temperature resistance of the chips. No VI needed.
TEST-ELEC-02	TCRmeasurement.vi	Calculate the TCR, the relationship between power and temperature, and the temperature control of this chips.
TEST-CALI-01	N/A	Calculate the force conversion factor of the test bench. No VI needed.
TEST-CALI-02	actuator_calibration.vi	Calibrate the magnetic actuator of the test bench.
TEST-CALI-03	calibration.vi	Calibrate the CS2 displacement sensor of the test bench.
TEST-PRE-01.	plenum_pressure.vi	Control the pressure in the LPM plenum.
TEST-THR-01	thrust_cold_pid_main.vi	Cold gas thrust tests, both methods
TEST-THR-02	N/A	Resistojet thrust tests.

5

Fabrication Characterisation

A large part of the objective for this project is to characterise the fabrication of the new LPM chips, in terms of their mechanical and electrical properties, as best as possible. It is practically impossible to manufacture a device to the exact design dimensions, and hence these differences must be measured as accurately as possible to better predict the functionality of the final products. The main chip dimensions, including the actual size of the resistance lines, as well as the exit area of the slots and holes, are described in Section 5.1. On the other hand, the results related to the electrical characteristics of the chips, including room temperature resistance and TCR, are given in Section 5.2.

5.1. Mechanical Characterisation

Part of the main research question for this project, stated in Chapter 2, consists of evaluating the discrepancies between the actual mechanical characteristics of the newly fabricated LPM chips and their design values, as well as analysing their effect. To fulfil this objective, the Keyence VK-X1000 3D Laser Scanning Confocal microscope at DASML was used. One chip of each type was tested, and it is assumed that the dimensions of all chips belonging to the same wafer lie within the uncertainty of the resulting values. This was deemed an valid assumption in consultation with Dr. van Zeijl, as the variability between chips belonging to the same wafer is practically negligible. However, this assumption may not be valid for chips belonging to a different wafer, and hence care should be taken by future students in this regard.

There are two main variables that are of interest to mechanically characterise the chips in this case: the size of the resistances, and the size of the slots/holes for the propellant to flow through. The general procedure followed to arrive at representative average values and measurement uncertainties was the same for both types of chip. For each variable, five regions of interest (ROIs) were selected, after which the image was frozen and the appropriate measurements were taken. The five regions were selected in a square configuration, with the fifth region being placed near the centre of the chip. This is done such that a representable value of the entire chip is found. The final value is taken as the average of these measurements with its uncertainty, calculated as shown in Equation (5.1) below, where N is the sample size, and x is the sample error:

$$\frac{\sqrt{\sum_{i=1}^{N} x_i^2}}{N} \tag{5.1}$$

5.1.1. Fabricated LPM Chips

The design dimensions of the chips used in this report have already been described in Chapter 2, however will be revisited here. Five wafers of the GSS and GH chips were ordered from the EKL, each containing 26 thruster chips. The GSS chips consist of 20 slots that are 100 µm wide and 6.28 mm long, whereas the GH chips consist of a grid of 40x40 holes with a diameter of 100 µm. The resistance lines are designed to be the same for both types of chip: 11 mm in length, 120 µm wide and 500 nm thick. With a titanium resistivity of $4.8 \cdot 10^{-7}$ Ωm, the design resistance of the chips is calculated using Equation (2.31) to be 9.26 Ω. As this project was underway, two wafers of each type were fabricated. Note that the first wafer of each type was not properly diced (i.e. cut into the 26 chips), as the active area of the chip was not diced in the middle of the total area. This does mean that some thrust will be lost as several holes/slots will be blocked when placed inside the interface designed in Chapter 3, hence it is advised that these wafers are used for mechanical and electrical testing only.

5.1.2. Resistance Dimensions

It is very important to characterise the actual dimensions of the resistance lines as these logically affect the resistance of the fabricated chips. Three dimensions were of interest: their height, length and width. An extra step was included in the procedure explained above to arrive at height measurements, as 3D information is needed. The laser scanning mode of the microscope was used for this, after which step heights were found while analysing the 3D data. On each region of interest, two areas were drawn: one on the resistance line and one on the adjacent silicon nitride layer. The microscope software then used the acquired 3D data to give a value for the height difference between the two areas, which in this case equals the height of the Ti resistance lines. Figure 5.1 shows an example of the preceding explanation. Since the length of the resistance lines was larger than the ROIs chosen to measure their height and width, five resistance lines were chosen and their length was measured separately. Again, the resistance lines were chosen to cover most of the chip area as possible, to arrive at the most representative result over the entire chip area.

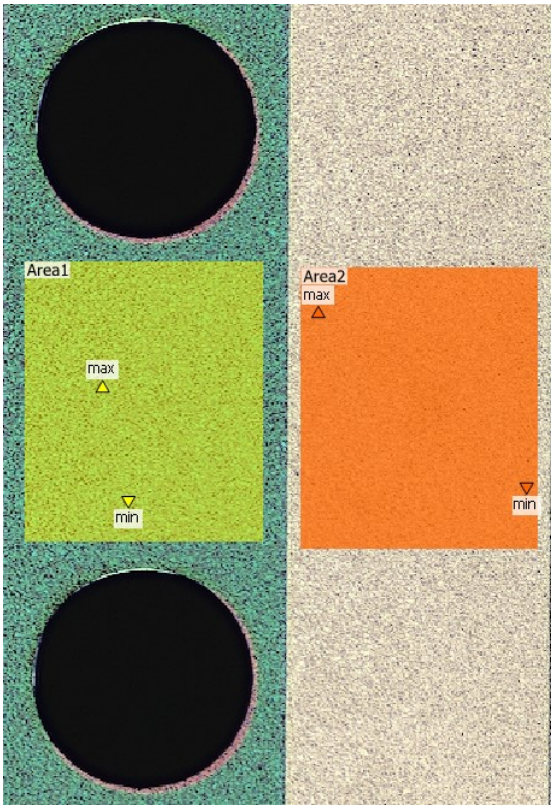

Figure 5.1: Areas used in ROI #2 to find the height of the resistor line, using the 3D data obtained from the laser scan. The reference area, Area 1 (Yellow), is placed on the silicon nitride layer, while Area 2 (Orange) is placed on the Ti layer.

Tables 5.1 and 5.2 gives the results for all measurements taken with regards to the resistance for both types of chip, as well as their final average values and uncertainties. The uncertainty of the 3D height measurements is given by the accuracy of the laser scanning mode, $\pm$ 0.5 nm (Keyence, 2015), while that of the width and length measurements is given as the sum of half of the thickness of the measurement lines shown in Figure 5.2, given that the two measurement lines have different thicknesses. These thicknesses were simply found by counting pixels and translating them into a dimension by using the appropriate scale.

Table 5.1: Measurement results for the resistor line dimensions of the GSS chip.

Measurement	**Width [µm]**	**Length [µm]**	**Height [µm]**
1	123.02 $\pm$ 3.45	10981.7 $\pm$ 0.24	0.556 $\pm$ 0.0005
2	123.38 $\pm$ 3.45	10985.5 $\pm$ 0.24	0.571 $\pm$ 0.0005
3	123.16 $\pm$ 3.45	10982.1 $\pm$ 0.24	0.572$\pm$ 0.0005
4	123.24 $\pm$ 3.45	10977.7 $\pm$ 0.24	0.596 $\pm$ 0.0005
5	123.15 $\pm$ 3.45	10984.1 $\pm$ 0.24	0.546 $\pm$ 0.0005
Mean	123.19 $\pm$ 1.54	10982.2 $\pm$ 0.11	0.568 $\pm$ 0.0002

Table 5.2: Measurement results for the resistor line dimensions of the GH chip.

Measurement	**Width [µm]**	**Length [µm]**	**Height [µm]**
1	123.07 ± 5.17	10982.7 ± 0.24	0.548 ± 0.0005
2	123.32 ± 5.17	10985.4 ± 0.24	0.439 ± 0.0005
3	123.12 ± 5.17	10983.6 ± 0.24	0.565 ± 0.0005
4	123.28 ± 5.17	10982.9 ± 0.24	0.589 ± 0.0005
5	123.29 ± 5.17	10984.6 ± 0.24	0.648 ± 0.0005
Mean	123.22 ± 2.31	10983.8 ± 0.11	0.558 ± 0.0002

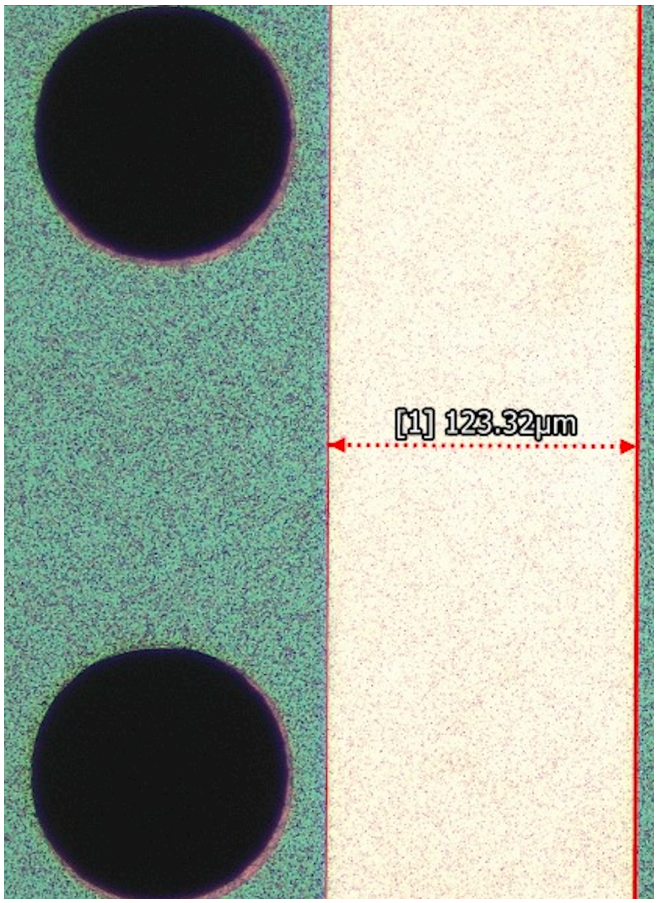

Figure 5.2: GH ROI #2 used to find the average width of the resistance lines.

As mentioned in the section above, the resistance lines were designed to have a width of 120 µm, a length of 11 mm and a thickness (i.e. height) of 0.5 µm. The results presented above show that, due to fabrication inaccuracies, the width and height of the lines turned out to be larger than desired, whereas their length became shorter. In terms of the GSS chips, a 0.16% decrease in length is observed, whereas the cross sectional area suffered a 16.6% increase. As for the GH chips, a similar 0.15% decrease is seen in length, with a 14.6% increase in area. From these results, it can be said that the GH chips were fabricated more accurately than the

GSS chips, as they are truer to their design values. These outcomes are further explored in the conclusion of this chapter.

5.1.3. Slot and Hole Dimensions

The actual dimensions of the slots in the GSS chips and the holes in the GH chips can be said to have an even greater importance to characterise. This is because the exit area of the propellant through the chips is directly proportional the thrust they produce, as seen in Equation (2.24). Following the general procedure described above, five ROIs were chosen and every slot/hole in each ROI was measured, as shown in Figure 5.3. Please note that the ROIs used to measure these dimensions are not the same ones that were used for the resistance line measurements. In terms of the slot length, and as done with the lengths of the resistance lines, five slots were chosen using the same reasoning as above, and the measured lengths were averaged. The final results are presented in Table 5.3.

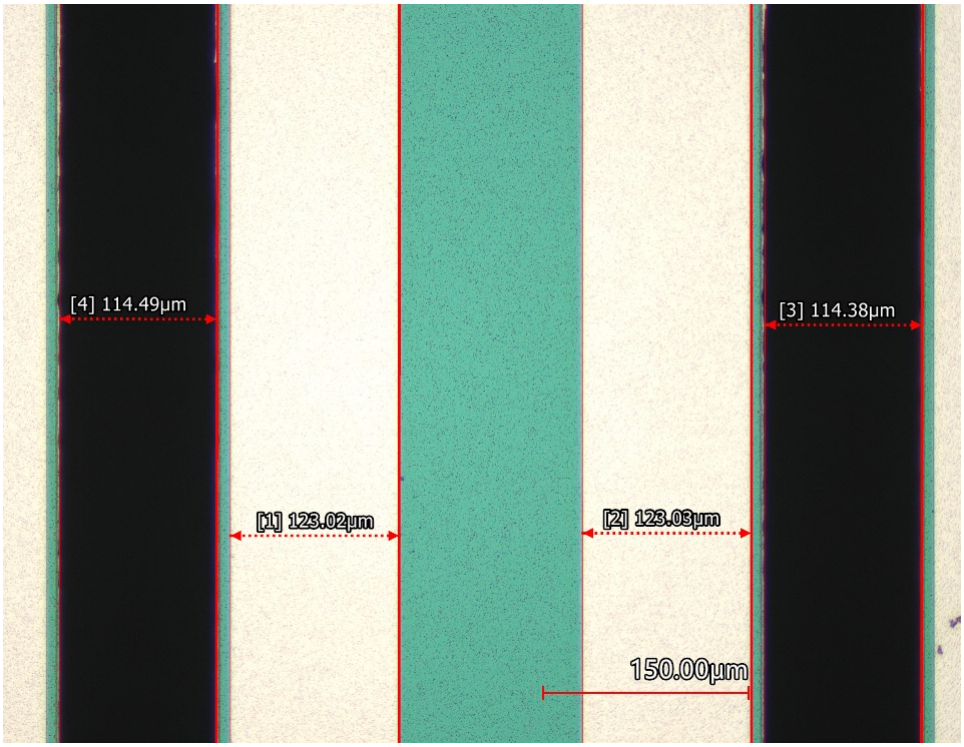

Figure 5.3: ROI #1 used to measure the widths of the GSS chip slots (black).

Table 5.3: Final averaged dimensions to size the GSS slots and the GH holes. Note that the uncertainties were calculated as expressed in the previous sections.

	GSS		**GH**
	Width [µm]	**Length [µm]**	**Diameter [µm]**
Mean	115.11 ± 1.23	6584.97 ± 0.18	101.58 ± 2.89

The GSS chips have been described to consist of 20 slots, whereas the GH chips are based on

a grid of 40x40 holes. With these newfound values, the actual exit areas of the chips are calculated to be 15.16 $\pm$ 1.6 mm^2 and 13 $\pm$ 7 mm^2 for the GSS and GH chips, respectively. These results again show that the GH chips were fabricated more accurately than the GSS chips, seeing that the found values differ less from the design values presented in Subsection 2.4.1.

5.2. Electrical Characterisation

The third sub-question proposed for this research relates to the electrical characteristics of the new LPM thruster chips. Their resistojet capabilities, as well as their desired secondary use as temperature sensors is examined in this section. As mentioned in Chapter 4, two main tests are planned as part of this characterisation. The results for room temperature resistance of the new chips, TEST-ELEC-01, are hence described in Subsection 5.2.1, whereas the TCR and power-temperature curves, TEST-ELEC-02, can be found in Subsection 5.2.2.

5.2.1. Resistance at Room Temperature - R0

As expected, the effect of the 4-point resistance measurement was seen quite clearly when measuring the room temperature resistance of the chips. Using the HP 34401A DMM in 2-point measuring mode, as shown in Figure 5.4a, the room temperature resistance of the chips was found to be 15.898 $\pm$ 0.02 Ω for the GSS and 14.664 $\pm$ 0.7 Ω for the GH, as averaged from the results shown in Table 5.4. When switching the DMM to 4-point, or sensing mode, as per in Figure 5.4b the resistance values decreased to 11.959 $\pm$ 0.05 Ω and 12.135 $\pm$ 0.1 Ω. These results show an average decrease of 24.8% for the GSS and 17.1% for the GH, proving that switching to 4-point measurements will indeed lead to lower resistance measurements during thrust testing. The results from the 4-point measurements can also be consider to better represent the actual resistance of the chips. This is because, as described in Subsection 4.1.1, measuring the resistance using 2 contact points means measuring the resistance of the circuit as a whole, including contacts and lead resistances. Clearly, if one wants to measure the resistance of the chip itself as accurately as possible, these so-called parasitic resistances must be neglected, which is the entire point of performing 4-point, or Kelvin, resistance measurements.

It is noteworthy that the measured resistance of the GH-01 chip noticeably differs from the other GH chips when performing a 2-point measurement. The GH-01 chip considered here was wire bonded to a PCB, which had been fabricated previously when testing the different electrical connections, as explained in Section 3.4. This provides further proof regarding the fact that 2-point measurements can significantly vary depending on the test setup (i.e. the wiring and contacts in this case), whereas the 4-point measurements are independent of this, and provides results solely taking into account the sample being measured.

Table 5.4: Room temperature resistance results using the 2 and the 4 point measurement techniques.

Chip	2-point [Ω]	4-point [Ω]
GSS-01	15.915	12.006
GSS-02	15.885	11.914
GSS-03	15.893	11.956
GH-01	13.844	12.138
GH-02	14.985	12.234
GH-03	15.164	12.033

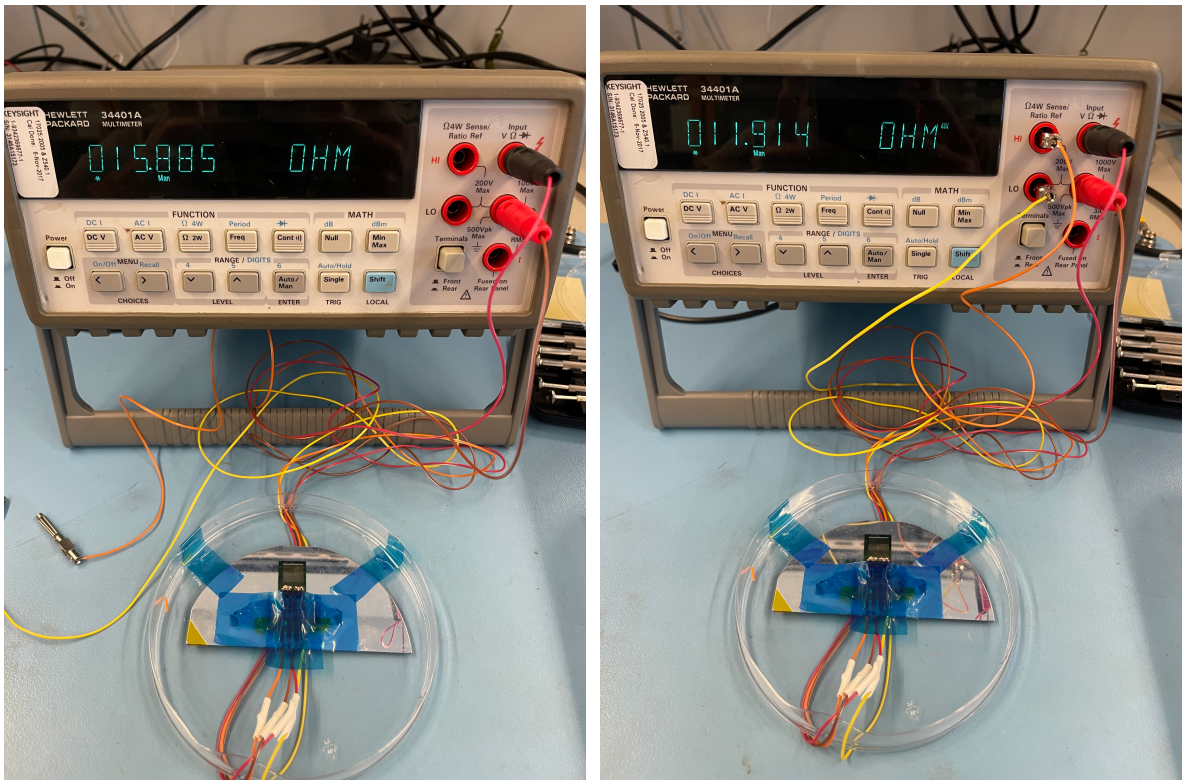

(a) 2-point R0 measurement

(b) 4-point R0 measurement

Figure 5.4: Room temperature resistance measurements of the GSS-02 chip.

5.2.2. TCR & Power - Chip Temperature Control

Following the procedure explained in Subsection 4.1.2, six data sets were obtained for each type of chip: three main tests with the primary thermocouple locations, and three more tests using a different chip and the secondary locations, to prove the repeatability of the results. First of all, a consistent offset of -0.042 A was noticed between the set current and the measured current, consistent with the accuracy of the programming mode of the PSU used, mentioned in Table 4.2. Since the measured current was used for the calculations, the PSU programming accuracy was hence not taken into account. Some more corrections were required before starting

the experiments as it was seen that the data acquisition program read some current and voltage drop values even though the PSU current was set to 0 A. An average current and voltage drop offset was calculated from the first 30 seconds of each test (i.e. the time in which the PSU current is set to 0 A) and applied to the results during post-processing. It was also noted that the resistance measurements took some time to stabilise from the offsets at 0 A to the point in which the chips actually started to heat up, closer to 0.2 A. Since only the linear relation is of interest to calculate the TCR, these points were not taken into account in the plots presented in Figure 5.5. The plots also clearly show the moments in time in which the supplied current was increased, represented by the slight changes in slope observed. Finally, note the different power-temperature relationships shown in Figure 5.6 for both chips. Since the resistance material for both chips is exactly the same, and the results from the mechanical characterisation of the resistor lines show very little deviation between the chips, it was expected that both would reach similar temperatures for the same applied power. It was already assumed that the GSS chips would be slightly cooler due to the higher exit area, and hence higher rate of heat loss through convection, however not to such a large extent. The most likely reason for this is attributed to different curing schedules used for the conductive glue used to glue the pins to the chips. Different curing schedules may affect the current carrying capabilities of the glue, and hence less current may actually go through the chip than provided by the PSU. This also explains why the TCR results are still similar for both chips, as the same factor that affects the current provided to the chips, and hence leads to lower temperatures, also affects the voltage drop being measured across them.

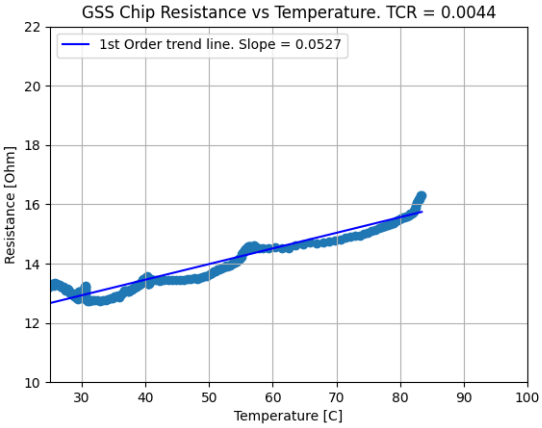

(a) GSS Test 1

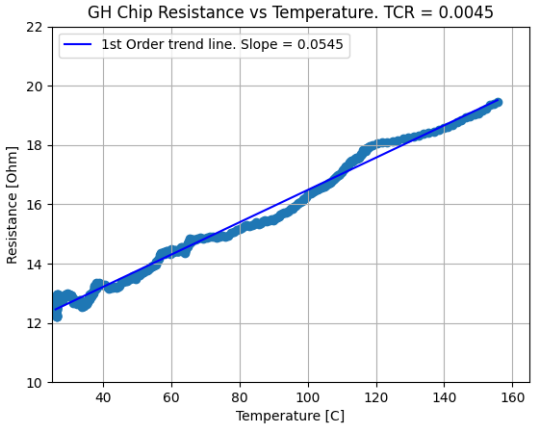

(b) GH Test 1

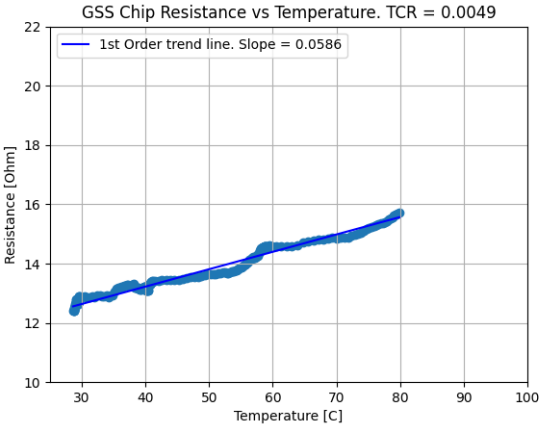

(c) GSS Test 2

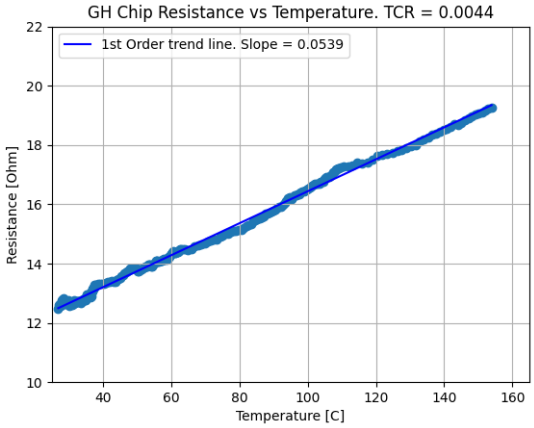

(d) GH Test 2

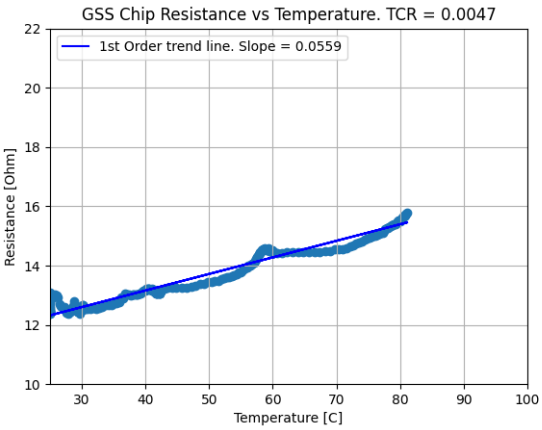

(e) GSS Test 3

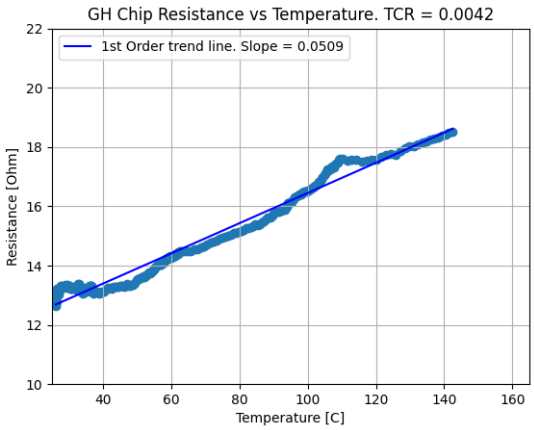

(f) GH Test 3

Figure 5.5: Results for the three TCR tests using the GSS chips (left) and the GH chips (right). Note that "Test 3" represents a test performed with a different chip of each type and the secondary thermocouple locations. This is plotted here to show the repeatability of the results under different test conditions.

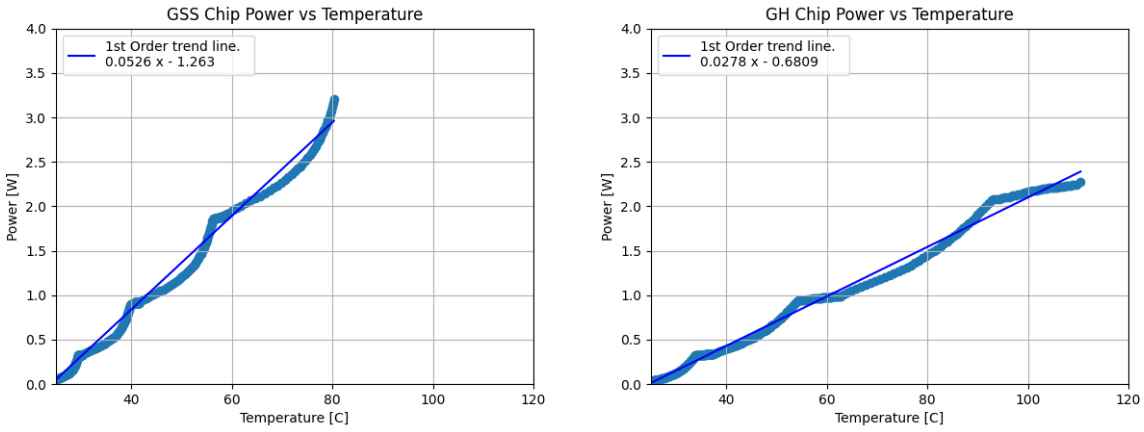

(a) GSS Chip

(b) GH Chip

Figure 5.6: Averaged power and temperature results from the three tests described above. As with the preceding curves, the sudden changes in slope are related to the step increases in the supplied current.

As shown in Table 5.5 below, the GSS chips have a β of 0.00464 $\pm$ 2.5 $\cdot$ 10^{-4} °C^{-1} and the GH of 0.00438 $\pm$ 1.6 $\cdot$ 10^{-4} °C^{-1}. These are the values that will be used to control the chip temperature during the thrust tests. Upon performing the test three more times with the secondary thermocouple locations for both types of chip, it was seen that the average β remained within the range described above, and hence the results were deemed to be acceptable. Previous experimental studies put the TCR of titanium at 0.00415 °C^{-1} (Singh et al., 2022) showing repeatability in the results obtained during this test campaign. The main reason for the differences is attributed to the accuracy of the thermocouples used to measure the temperature as mentioned in Table 4.2, as well as the method used (i.e. placing three thermocouples and calculating an average). Assuming both the thermocouple and the DAQ accuracies to be independent, each temperature measurement had an uncertainty of $\sqrt{2.2^2 + 2.5^2}$ (Lynn, 2002). Each temperature measurement therefore has an uncertainty of $\pm$ 3.3 K. Again using Equation (5.1), the uncertainty of each calculated average temperature, without taking into account the effect of the thermocouple location, is calculated to be $\pm$ 1.9 K. Due to the resistance layout, it is expected that the temperature is not uniform across the chip and hence measuring its overall temperature as an average of three thermocouples may not yield the most representative value. Recommendations on how to improve this will be given in the conclusion of this chapter.

Table 5.5: TCR results for the three tests done on each type of chip using the thermocouple locations as per Figure 4.2a.

Test	**GSS**	**GH**
1	0.00439	0.00449
2	0.00489	0.00444
3	0.00465	0.00419
Mean	0.00464	0.00438
$\boldsymbol{\sigma}$	0.00025	0.00016

Finally, Figure 5.7 shows that, with the calculated TCR value and using Equation (4.1), the GH chip has indeed been calibrated as a temperature sensor for a temperature range of 30-140 °C. Note that, as with the TCR tests, the resistance measurement, and hence the temperature calculation, only stabilises once a certain amount of current is applied, close to 0.2 A. This is shown in the plot as the calculated temperature curve (the orange plot) starts to approximate the measured temperature (the blue plot) at around the 40 second mark, when over 0.1 A are applied to the chip. Again, the points in time at which the current is increased can be clearly seen in the measured temperature line. This test was only performed for the GH chip due to the previous discussion regarding the unexpected behaviour of the GSS chip tests, and hence the resistojet testing should focus on the GH chips, as more testing is advised in terms of the GSS chip.

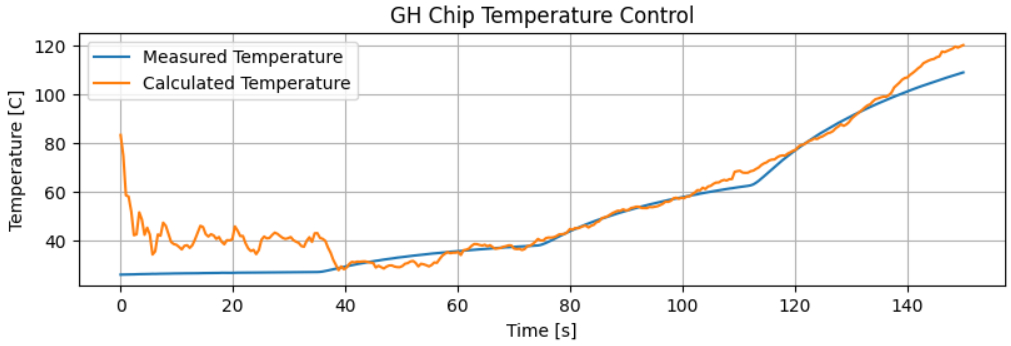

Figure 5.7: Measured and calculated temperature using the TCR and Equation (4.1) for the GH chip.

Furthermore, note the slightly diverging behaviour between the two curves as the measured temperature exceeds 100 °C. It is clear that the temperature of the chip, using the measured TCR, can be controlled more accurately for the temperatures below this value. This difference is attributed to the decreasing accuracy of the average temperature measurement as the power provided to the chip increases, which consequentially leads to a decrease in the accuracy of the calculated TCR. As the power increased during the tests, it was noticed that the thermocouple placed closer to the centre of the chip read an increasingly higher temperature than the ones placed near the edges, skewing the average towards a higher, and less representative value.

5.3. Conclusions

In summary, this chapter represents the quality control procedure done on the fabrication of the new LPM chips. Two important aspects were discussed, namely their main mechanical and electrical characteristics. The former consisted of performing microscope measurements on both types of chip to accurately size their resistance lines as well as their actual exit area, which directly affects the thrust produced by them. The latter involved calculating the relationship between the chip's temperature and its resistance, allowing for the temperature to be controlled without the need of extra sensors on board, as well as knowing the amount of electrical current required to bring the chips to certain desired temperatures.

The fabricated size of the resistance lines is cause for discussion. Inputting the values from Tables 5.1 and 5.2 into Equation (2.31) allows for the calculation of the actual fabrication

resistance of the new LPM chips which, as expected, slightly differs from its design value of 9.26 Ω. A room temperature fabrication resistance of 7.93 ± 0.10 Ω and 8.07 ± 0.15 Ω for the GSS and GH chips are found, respectively. On the other hand, the room temperature resistance measurements reported in Subsection 5.2.1 tell another story. The GSS and GH chips are measured to have a resistance of 11.959 Ω and 12.135 Ω, respectively. This difference between the resistance calculated using the measured resistor dimensions and the one measured using a multimeter can be explained as follows. Even though the 4-point method allows for the elimination of most contact and lead resistances, other parasitic resistances arise in the circuit which are not accounted for due to the location of the multimeter leads, as well as the layout of the resistor itself, for example the resistance of the aluminium contact pads between the two pins on the same side of the chip, illustrated in Figure 5.8. To conclude the results of the mechanical characterisation, the actual exit areas of the GSS and GH chips were calculated to be 151.6 ± 1.6 mm ^{2} and 130 ± 7 mm^2, respectively.

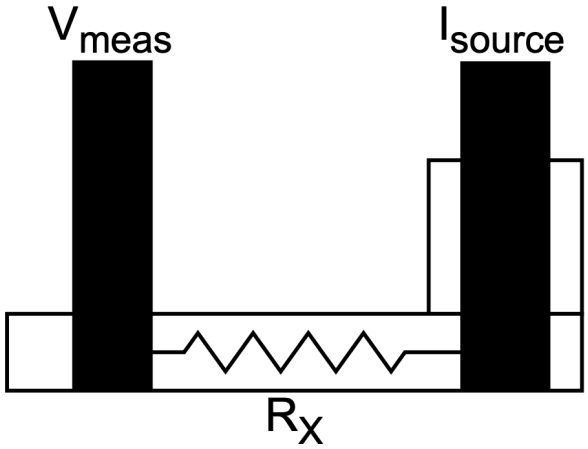

Figure 5.8: Simplified diagram showing an example of a parasitic resistance (R_X) not taken into account by the 4-point measurement. Shows one contact pad of the LPM chip, as well as the two pins connected to it: I_{source} to provide a current, and V_{meas} to measure the voltage drop across.

In terms of the electrical characterisation of the fabricated chips, their room temperature resistances, as well as their TCR were measured. Three chips of each type were measured for their room temperature resistance using both the 2-point and 4-point measurement methods, to analyse its effect. 2-point resistance measurement results were 15.898 ± 0.02 Ω for the GSS chip and 14.664 ± 0.7 Ω for the GH chip. When switching the DMM to the 4-point measurement method, removing the influence of contact and lead resistances from the circuit, the room temperature resistance values dropped to 11.959 ± 0.05 Ω and 12.135 ± 0.1 Ω, respectively, proving that switching to 4-wire connections is beneficial in terms of measurement accuracy. Furthermore, as expected, the two types of chips were found to have very similar TCR values, comparable to published experimental values (Singh et al., 2022). For the GSS, an average TCR from three tests of 0.00464 ± 2.5·10^{-4} °C^{-1} was found. In terms of the GH, the resulting value was 0.00438 ± 1.6 · 10^{-4} °C^{-1}. Some problems were encountered however in terms of the power/temperature relationship of both chips. For the GSS, it was found that the same values of power lead to much lower chip temperatures, which is not in line with the fact that the resistances of both chips are designed in the same way and have negligible fabrication differences as shown by the mechanical characterisation. The difference in P/T re-

lationship is thought to be a consequence of different curing schedules and temperatures used for the conductive gluing of both chips. This is assumed to have resulted in different current carrying capabilities of the electrical connection used in both chips, leading to different P/T curves. With this in mind, only the GH chip was tested in terms of temperature control. It was found that the calculated TCR lead to the calibration of the chip as a temperature sensor for the range of 40-140 °C.

It is certainly recommended to perform the TCR experiments once more, using a more accurate method to measure the temperature of the chips. Using three randomly placed thermocouples has obvious sources of uncertainty. If possible, a uniform emissivity ink should be applied to the chips, allowing their temperature to be accurately measured by the available IR camera, as done by Guerrieri, Silva, Zeijl, et al. (2017). Furthermore, the issues arisen from the conductive glue used are clearly cause for repetition of the experiments with regards to the GSS chip, as well as revisiting the electrical connection method as a whole. Discarded due to interface volume requirements, the PCB option is still the most robust alternative in terms of a stable electrical connection. Future work should also focus on the complete re-design of the resistance layout of both chips, allowing for a more constant temperature profile across them. Having one contact pad for several resistance lines in parallel likely leads to different currents being applied to each, specially if the fabricated lines differ ever-so-slightly in dimensions, and hence resistance. It also means that slight differences in the length of the current path may be observed, leading to different resistances and hence current applied. Finally, even though the temperature has been proven to be quite stable as a function of the applied power, it is recommended to create a PID to control the chip temperature during resistojet testing.

6

Propulsion Characterisation

In this chapter, the results of the propulsion characterisation of the new LPM chips, as a means to answer the fourth research sub-question, are presented. As mentioned in Chapter 4, several preliminary tests were performed, all of which build up to the most important results of this thesis: the thrust of the new LPM chips. The first set of tests, needed to calibrate the thrust bench used in this report, are presented in Section 6.1. This is followed by Section 6.2, where an investigation into which solenoid valve duty cycles and feed system pressures lead to the required LPM plenum pressures is found. Finally, the cold thrust results for both chips are presented in Section 6.3, the remaining inventory after the tests is shown in Section 6.4, and a conclusion to the chapter, including a summary of the main findings, in Section 6.5.

6.1. AE-TB-5m Calibration Results

As mentioned above, the results for all calibration procedures done prior to thrust testing are presented in this section. Three calibrations were performed in total, in which one simply consisted of performing ruler and caliper measurements, whereas the rest involved slightly more complicated procedures, with many more components and pieces software required. The force conversion factor, required to relate the force generated at the bottom of the pendulum to that closer to the sensor, is described in Subsection 6.1.1. This is followed by the two more complicated procedures, namely the magnetic actuator calibration, in Subsection 6.1.2, and the displacement sensor calibration, described in Subsection 6.1.3.

6.1.1. Force Conversion Factor

A breakdown of the required measurements and formulae to calculate the force conversion factor (i.e. the relation between force at the bottom of the pendulum and at the sensor) was given in Subsection 4.2.1. The results for the measured distances are given in Table 6.1 below. Note that L_{TR-P}, L_{HR}, L_{MAG} and L_{BP-THR} were measured with vernier calipers, previously mentioned to have an accuracy of $\pm$ 0.02 mm, and the other two lengths were measured with a ruler with an accuracy of 0.25 mm. The uncertainty of each average length is calculated using Equation (5.1), and hence the uncertainty of the average lengths calculated with the calipers is calculated as $\pm$0.01 mm and that of the ones for which the rule was used as $\pm$0.14 mm.

Table 6.1: Measurements taken to find the lengths needed for the calculation of the force conversion factor. The final measurements are given by their mean and an uncertainty of one standard deviation.

Length [mm]	L_{TR-P}	L_{HR}	L_{BHR-TA}	L_{MAG}	L_{BHR-BP}	L_{BP-THR}
1	5.25	10	143.2	30.1	243.5	18.1
2	5.3	10.05	142.9	30.2	243.3	18
3	5.3	10	143.1	30.2	243.3	18.1
Mean	5.28	10.02	143.07	30.17	243.37	18.03

Using Equations (4.4) and (4.5), the force conversion factor is calculated as:

$$\lambda = \frac{L_{act}}{L_{thr}} = 0.612 \pm 0.001 \tag{6.1}$$

6.1.2. Magnetic Actuator Sensitivity

Following the test procedure described in Subsection 4.2.2, this test was performed a total a five times. The final test setup is seen in Figure 4.4, minus the cleanroom PC and the PSU. The results for the tests can be seen in Table 6.2. The sensitivity value found by Versteeg (2020) and Pappadimitriou (2021), 0.827 mN/A, has clearly changed over the years, proving that it was a good idea to perform the calibration procedure again to re-characterise the response of the coil to a given current. As mentioned in Subsection 4.2.2, the equipment accuracy in this case is discarded as the PSU and the actuator are calibrated as a whole, and then same equipment will be used during thrust testing. The final result for the sensitivity of the magnetic actuator coil, including its uncertainty, calculated as the sample standard deviation of the calculated sensitivities, is given by Equation (6.2).

Upon detaching the VTDC from a different test bench to set up this experiment, one side of the copper coil snapped as it had been moved and twisted too many times. This was fixed by soldering the broken piece back with the rest of the coil, securing it with a heat shrink tube and applying some glue to restrict movement and prevent it from snapping again. This could therefore be one of the reasons for which the calculated sensitivity appears to have changed when compared to past results. Another possible reason for the change in results is the observable change in coil positions. By visual inspection it can be seen that some of the glue used to fix the coil turns in place has worn off, leaving some space for the distance between the turns to change, which can directly affect the magnetic field created when a current is applied (Bijster, 2014).

$$S_c = 0.8134 \pm 0.0002 \quad [mN/A] \tag{6.2}$$

Table 6.2: Results for the calibration of the magnetic actuator. Note that the result for the test performed right before the thrust tests is not shown as it was not used to calculate the mean, however the sensitivity was confirmed to be within the confidence interval given in Equation (6.2). The smallest R^2 value of the linear regressions applied to all tests was 0.9998.

Test Name	Sensitivity	Comments
CALI-01	0.8135 mN/A	N/A
CALI-02	0.8132 mN/A	Performed by fellow MSc student Andrei Pârvulescu to remove measurement reading bias.
CALI-03	0.816 mN/A	Deemed an outlier when calculating the mean sensitivity.
CALI-04	0.8136 mN/A	Performed to have three values from which to calculate the mean (as CALI-03 was discarded).
MEAN	0.8134 mN/A	Mean sensitivity calculated with CALI-01, CALI-02 and CALI-04.
σ	0.00021 mN/A	Standard deviation of the calculated sensitivities, excluding the outlier.

6.1.3. Sensor Calibration

The sensor calibration test was performed three times following the procedure described in Subsection 4.2.3. Figure 6.1 shows the resulting current and displacement plots of one of the tests, after being smoothed out using a simple moving average filter. The relative displacement is found by subtracting the average baseline displacement from the sensor displacement data, where the average baseline is given as (d_{start} + d_{end})/2, to take into account any zero error that may arise due to the used setup and procedure. Note that, as mentioned before, each displacement data point is accurate to within $\pm$ 5.02 µm.

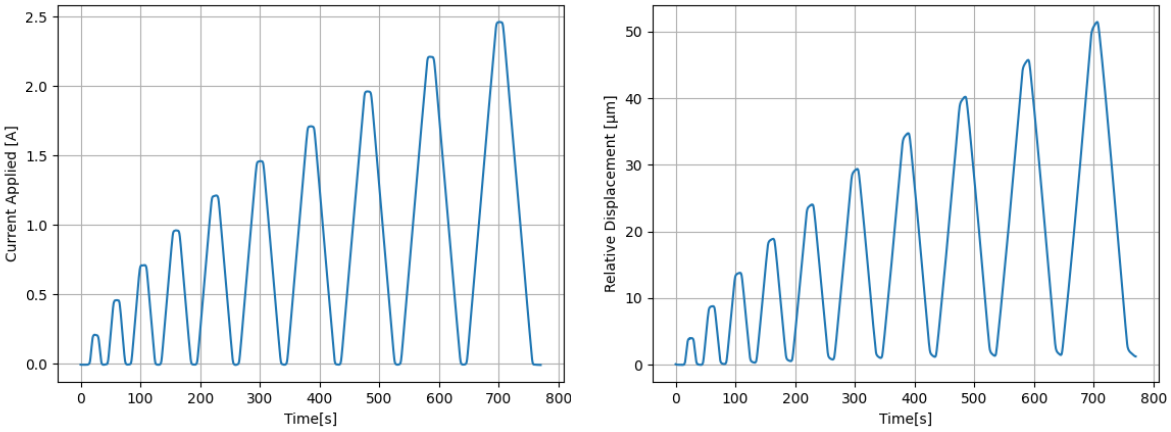

(a) Current vs time

(b) Displacement vs time

Figure 6.1: Current and displacement plots obtained during the post processing of the data from test #2.

A peak finding function was used in both plots, after which the current peaks were converted into force values using the actuator sensitivity found in the preceding section. Plotting the force peaks against the relative displacement peaks yielded Figure 6.2 below, where the slope gives the sensor sensitivity S_d. The results for the three tests performed, as well as the final average sensitivity and the uncertainty based on one sample standard deviation are found in Table 6.3

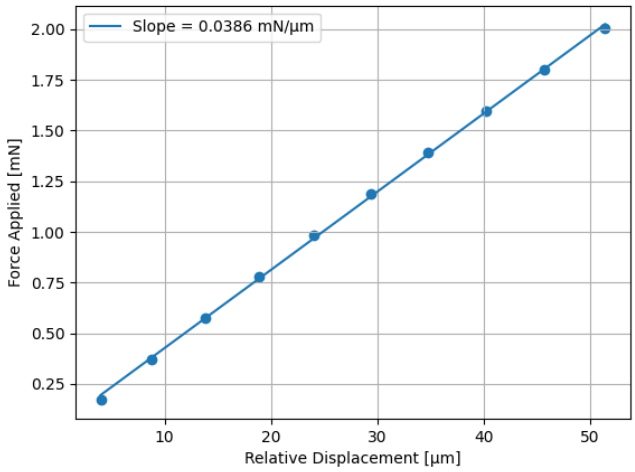

Figure 6.2: Force-displacement relation to calculate the sensor sensitivity S_d.

Table 6.3: Results for the three tests to find the CS2 displacement sensor sensitivity S_d.

Test	**S_d [mN/μm]**
1	0.03912
2	0.03856
3	0.03968
Mean	0.03912
$\boldsymbol{\sigma}$	0.0006

Upon completing the three calibration procedures required by the test bench, Equations (4.6) and (4.7) become Equations (6.3) and (6.4) for the displacement and the force methods, respectively:

$$F_{thr} = (0.03912 \pm 0.0006) \cdot (0.612 \pm 0.013) \cdot \Delta d \tag{6.3}$$

$$F_{thr} = (0.8134 \pm 0.0002) \cdot (0.612 \pm 0.013) \cdot \Delta I \tag{6.4}$$

6.2. Plenum Pressure Control

Upon assembling the setup described in Subsection 4.2.5 and testing whether all the sensors were operational prior to closing the vacuum chamber and turning on the pump, a small offset was observed in the HCLA12X5DU pressure sensor signal. As per is data sheet (TE Connectivity, 2021), a 0.25 V signal should be read by the PC for a differential pressure of 0 mbar, expected when the interface is at atmospheric pressure. However, an average signal of 0.272 V was read, which was directly corrected for in the LabVIEW code for all experiments. All other sensors were seen to be operating nominally, and hence the tests were started.

As the pressure has to be decreased by several orders of magnitude before it reaches the plenum, the smallest duty cycle attainable by the valve, 4%, was used as a starting point. The supply gas pressure was set at 1.2 bar, attainable by setting the high pressure regulator of the GPFS on the smallest mark. By looking at the results shown in Figure 6.3, it is clear that keeping a constant plenum pressure is no easy feat. An average plenum pressure of 1 mbar was obtained, however it is anything but stable, which is not acceptable specially when using a pendulum to measure the thrust of the LPM, where thrust bursts in the order of a few seconds at a constant pressure are desired. The bottom figure shows the resulting pressure profile using a duty cycle of 8%. As expected, the average plenum pressure increases with increasing duty cycle, however it also becomes more unstable, as larger deviations from the mean are observed. Note that the time frame in both charts is also smaller because, as expected, a higher plenum pressure requires a higher mass flow, which in turn increases the ambient pressure of the chamber in less amount of time.

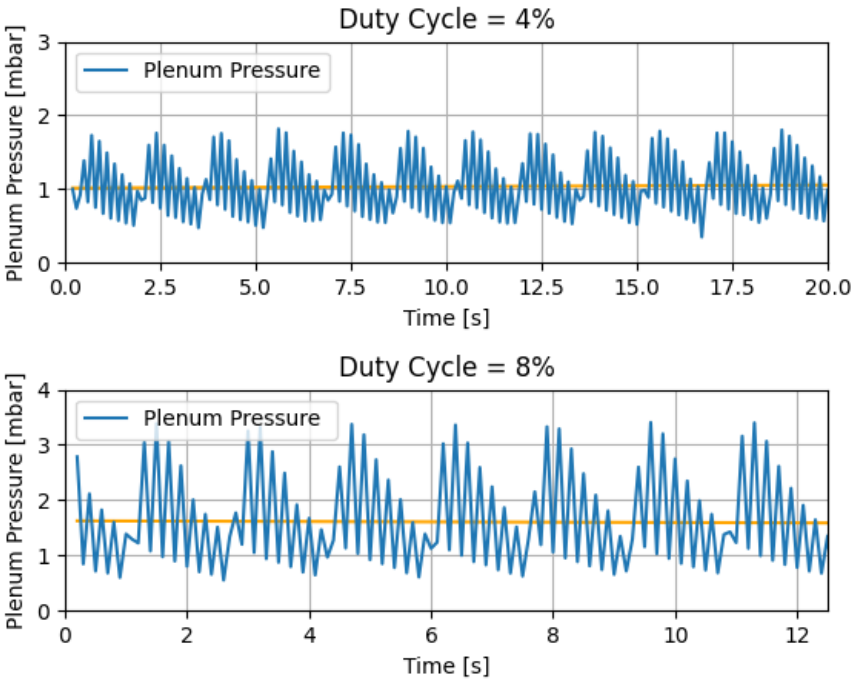

Figure 6.3: Resulting plenum pressure profiles using duty cycles of 4 and 8 % and a supply gas pressure of 1 bar.

Upon seeing these results, as well as the ones for several other duty cycles, it was logically concluded that controlling the plenum pressure with this setup was virtually impossible within the time available. It was then decided to switch the tubing in the setup, to allow for a longer tube between the solenoid valve and the LPM interface, hoping that the pressure would stabilise in this longer tube before reaching the plenum. The setup shown in Subsection 4.2.6 was assembled instead and the tests were repeated. Starting with the same supply pressure and duty cycle as before, it is immediately clear that the new setup allows for the pressure to stabilise before reaching the LPM. After several duty cycle tries, the final results can be seen in Figure 6.4.

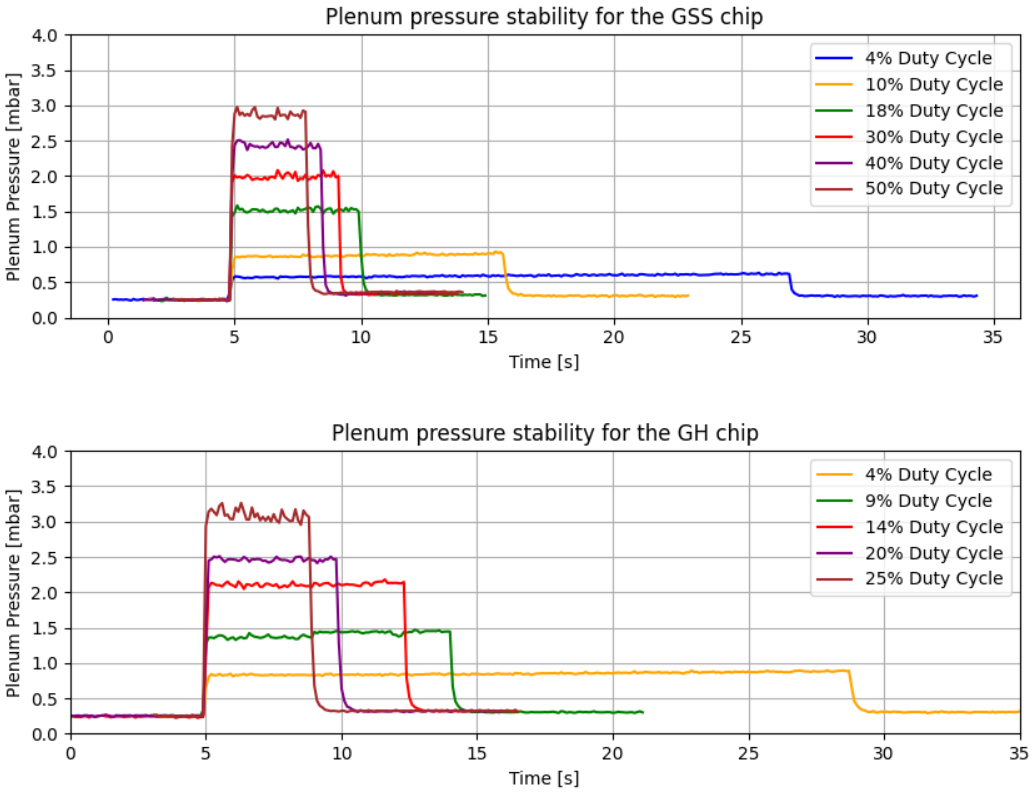

Figure 6.4: Valve duty cycles to achieve the stable plenum pressures required for thrust testing with a supply gas pressure of 1.2 bar.

As seen when comparing both figures, different duty cycles must be used for each chip. This was expected because, due to the smaller exit area and transmission coefficient of the GH chips, the same valve duty cycle leads to a larger build-up in plenum pressure. It can also be observed that the pressure stability decreases for increasing plenum pressure. Again, this was previously predicted as in the case of this setup, higher pressures require longer tubing to stabilise before reaching the plenum. Another logical conclusion is that the inverse proportionality between mass flow and the time it takes for the background pressure to increase by 5 Pa is made even more clear in these plots. As was mentioned in Subsection 4.2.5, the solenoid valve was left open until the background pressure increased by 5 Pa. For larger duty cycles, the mass flow is logically higher, and hence the time taken for the background pressure to increase by the given threshold is smaller. This can also be seen by comparing the time scale at each pressure profile between the GSS and GH chips, as again, the larger mass flow for each plenum pressure seen in the GSS chip leads to shorter times for the background pressure increase to be reached. Finally, in terms of the GH chips, these results show that, with the current setup and equipment, the GH cannot be tested with a plenum pressure lower than 80 Pa, as 4% is the lowest attainable duty cycle by the used solenoid valve, at least considering the current LabVIEW and Arduino setup. The duty cycles shown above were considered to yield acceptable pressure stability profiles and were therefore used for the thrust testing of both chips.

6.3. Cold Thrust Tests

Upon assembling the test setup shown in Figures 4.7 and 4.8, and checking for the correct functioning of the sensors present in the system, the vacuum chamber was closed and the pump was turned on. As mentioned in Subsection 4.2.6, the original idea was to perform the tests using both thrust measuring methods. However, after the first test run, it was quickly seen that thrust bursts of over 10 seconds were required for the force compensation method to work, as mentioned by Versteeg (2020). Since a constraint was put on the maximum allowable increase in background pressure (i.e. 5 Pa), this method was directly discarded as, for most plenum pressures, and hence mass flows, this threshold was met well before the 10 second mark. The reasons for selecting this background pressure increase threshold are given in Subsection 4.2.6. In summary, they relate to the time wasted between experiments (for the vacuum chamber to reach the low background pressures again after each test), the small effect this pressure change has in the thrust values (i.e. a maximum of 4%), and the fact that the only other test campaign performed on the LPM by Guerrieri, Silva, Zeijl, et al. (2017) uses the same background pressures, hence enabling a better comparison between the results obtained. The focus thus shifted to the displacement method of measuring thrust. As a means to show the repeatability of the results, hence increasing their reliability, three test runs were performed for each type of chip: two using the same pendulum equilibrium position, and another one with a different position to analyse its effect on the thrust results. This lead to a total of 45 thrust values for each type of chip, which are analysed in Subsection 6.3.1.

As mentioned in Subsection 4.2.6, three starting background pressures were chosen for the tests (20, 25 and 30 Pa). However, during each test, this pressure was allowed to increase by 5 Pa in order for the pendulum to have enough time to reach a new equilibrium position. This does mean that the resulting thrust values and curves do not belong to a single background pressure, but to three distinct ranges: 20-25 Pa, 25-30 Pa and 30-35 Pa. The reason for chosing this specific background pressure threshold is explained in Subsection 4.2.6.

As explained many times throughout this report, the thrust is calculated as a function of the displacement sensor sensitivity S_d, the force conversion factor λ, and the change in pendulum displacement Δd due to the opening of the solenoid valve in the propellant feed system. This relationship can expressed by Equation (6.3). The first two are constant for all experiments, as they are based on the performed calibration procedures and are not expected to change throughout the duration of the thrust test campaign. Therefore, the only variable for each test, with a constant background and plenum pressure, is the change in displacement. An example displacement-time relation for one of the tests performed is seen in Figure 6.5 below. The solenoid valve is opened at the 8 second mark and closed at the 10 second mark, as the background pressure reaches the 5 Pa increase threshold. The amplitude of the pendulum oscillations after the thrust burst are much larger than before, as expected, which will affect the error in the thrust calculations, as will be explained in Subsection 6.3.2. As seen in the raw data (i.e. the blue curve), the amplitude of the pendulum oscillations makes it challenging for the change in displacement to be discerned, especially for the lower plenum pressures. For this very same reason, a simple yet effective moving average filter is applied to smooth out the data. This smoothing is not only useful for visualisation purposes, as it also makes it much clearer when the thruster is operational, facilitating the calculation of the change in displacement from the raw experimental data. To complete the example, for a change in

displacement of d_1 - (d_0 + d_2)/2, the peak displacement d_1 is taken as the raw displacement data from seconds 8-10, whereas the trough displacements d_0 and d_2 are taken from seconds 0-7 and 12-20, respectively. All thrust points displayed in Subsection 6.3.1 are calculated following the same procedure.

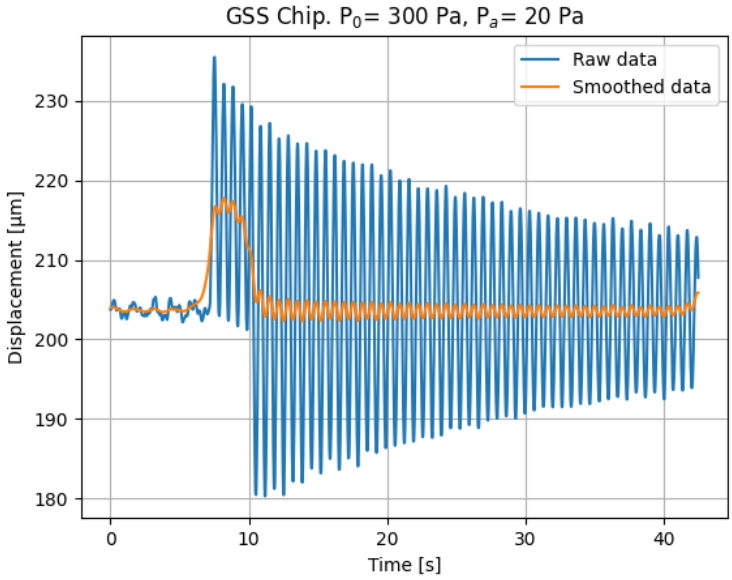

Figure 6.5: Pendulum displacement profile for one of the tests performed on the GSS chip.

Another common post processing step was correcting for the actual mass flow of propellant expelled by the chips. It was observed that the Brooks 5850S mass flow controller outputted certain mass flow values even though the valve was closed and the mass flow should be zero. This positive offset, which differed slightly from test to test, was consequently calculated and subtracted from the mass flow values read when the valve was opened during all tests. Furthermore, the mass flow values read by the controller were the total mass flow values of the system. However, the actual mass flow of propellant expelled by the chips is given by this total value multiplied by the transmission coefficient α of each chip which, using Equations (2.5) and (2.6) and the results from the mechanical characterisation presented in Chapter 5, was calculated to be 0.383 and 0.179 for the GSS and GH, respectively.

6.3.1. Test Results

The results for all 45 tests performed on the GSS and GH chips are shown in Figures 6.6 through 6.9. In terms of repeatability, as expected, the largest differences in thrust results are seen in the lowest plenum pressures tested. The reason for this is that the background pressure represents a higher percentage of the lower plenum pressures, making it harder to discern from the resulting pendulum oscillations as compared to the higher plenum pressures. Quantitatively, the average percentage difference between the 3 sets of tests performed for the GSS chip for the lower plenum pressure is 20%, whereas that for the highest plenum pressure is 7%. For the GH chip, these percentages increase as the thrust values are smaller, and are given as 18% and 4%, respectively. Upon calculating these percentage differences, no

trends were seen that pointed to the change in equilibrium position (i.e. the third test of each cluster) being the reason, hence this is concluded to not affect the thrust results. For example the percentage difference between the two first tests (using the same equilibrium position) was larger for some plenum pressures when compared to the third tests, and smaller in other pressure values. The most likely explanation for this rather random trend is the choice of the displacement peaks in each test. As these were chosen visually, it is entirely possible that some human errors were introduced, which were larger for some values. However, the low percentage differences seen for the larger plenum pressures still show a rather high degree of repeatability, and hence reliability, of the calculated thrust values.

As expected, the thrust provided by the chips increases with increasing plenum pressure, in line with the theory presented in Chapter 2, and likewise, the thrust provided by the GH chip is lower than that of the GSS chip. The curves also prove what was expected in terms of the background pressure. As this increases (i.e. from the blue to the green lines), the thrust decreases as the pressure thrust term in the thrust equation, Equation (2.10), decreases as well. Furthermore, it was hypothesized that the results for the three background pressure ranges would be much closer to each other for the lower plenum pressures than for the higher ones. This is proven by the results as the three plotted lines on each plot get further from each other as the plenum pressure increases. The reason for this is the same as explained in the paragraph above: for lower plenum pressures, it is harder to discern the pendulum peak displacements. An overlap between points belonging to two different curves is also observed in some cases, which is also logical given that the three background pressure ranges tested practically overlap with each other. Also note that, in line with the results for the plenum pressure stability of both chips presented in the section above, slightly different plenum pressures were tested for each chip. This is due to the fact that all pressure stability tests were performed at the same background pressure, hence using the same duty cycle for a different background pressure lead to slightly different plenum pressures than the ones presented previously.

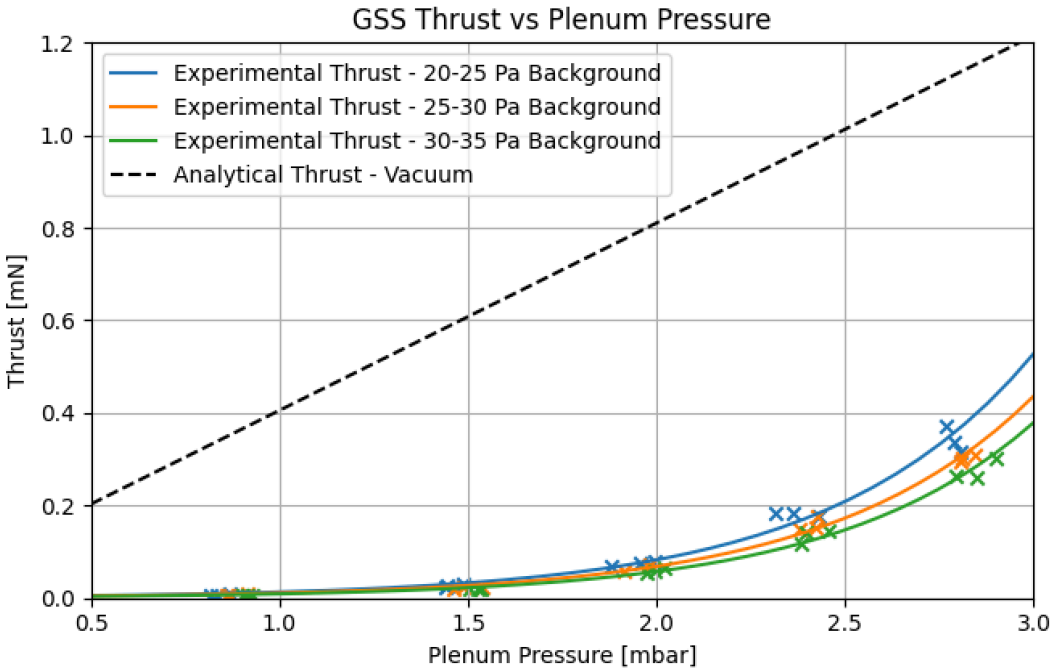

Figure 6.6: Thrust results for the GSS chip as a function of plenum pressure. Results of the analytical model described in Chapter 2 are shown for reference.

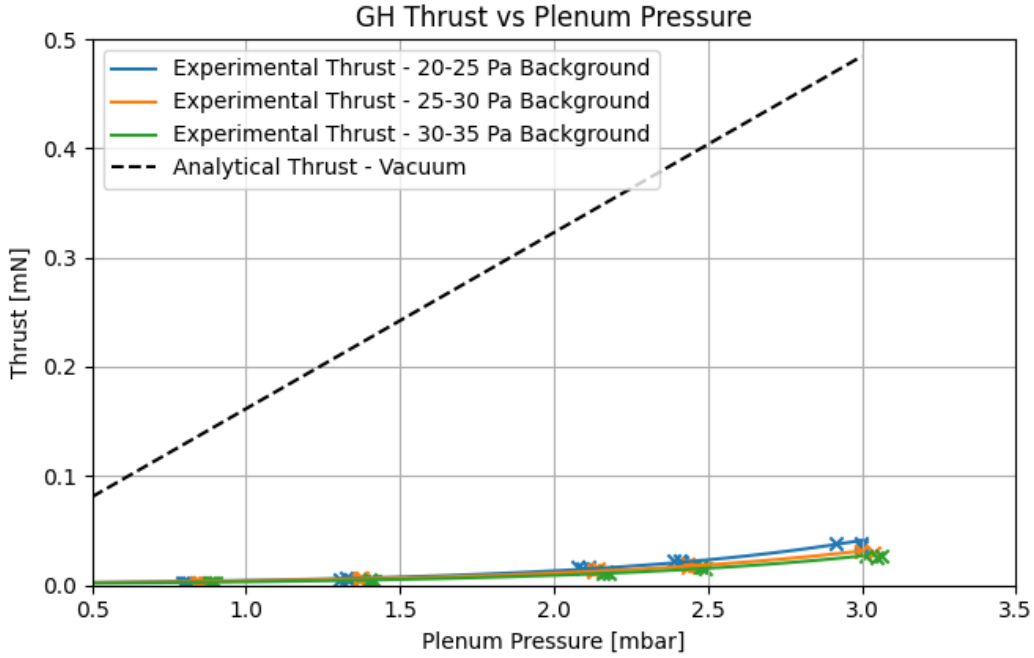

Figure 6.7: Thrust results for the GH chip as a function of plenum pressure. Results of the analytical model described in Chapter 2 are shown for reference.

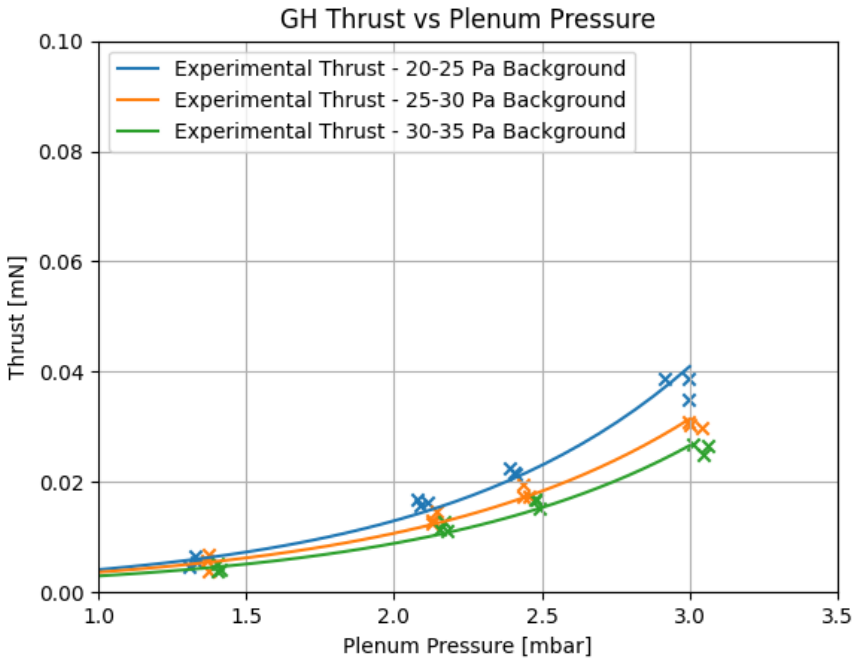

Figure 6.8: Close up of the thrust results for the GH chip, for easier visualisation

The mass flow plots also follow the expected trends with respect to the plenum pressure, as seen in Figures 6.9a and 6.9c. As predicted by the analytical model, these two parameters are proven to share a linear, direct proportionality. As expressed by Equation (2.9), the slope of the relationship between mass flow and plenum pressure is given by the term αA_e. Note that the term inside the square root is not discussed here as this is constant for both types of chip. Due to the smaller transmission coefficient and exit area of the GH chips, the slope of the plot was expected to be smaller than that of the GSS chips, which is indeed shown in the related figures. On the other hand, in terms of the specific impulse, calculated as the thrust divided by the product of the mass flow and the acceleration due to gravity, the same trend is observed when compared to the thrust plots, as predicted due to the way it is calculated. This calculation is also the reason why a larger deviation between the displayed I_{sp} points when compared to the thrust values is observed.

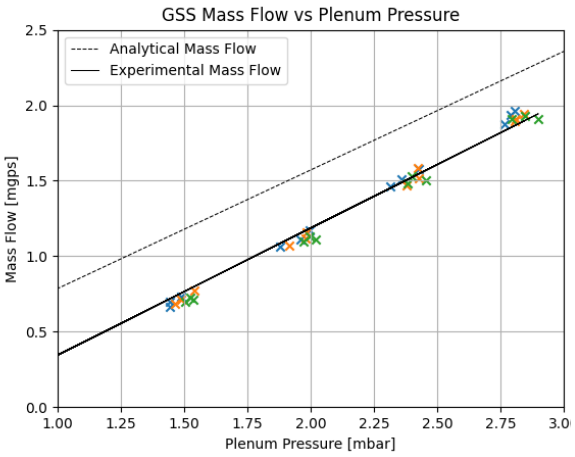

(a) GSS propellant mass flow.

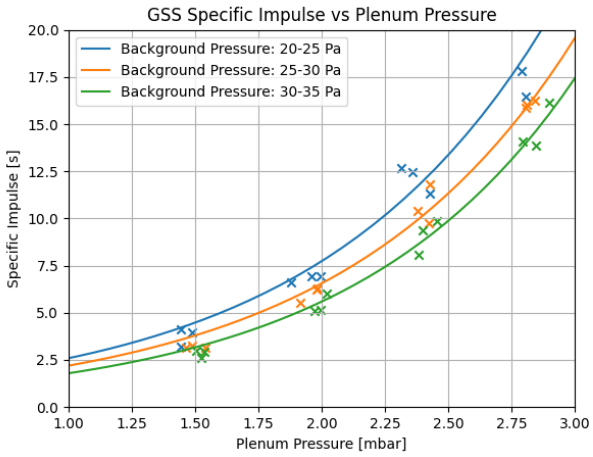

(b) GSS specific impulse.

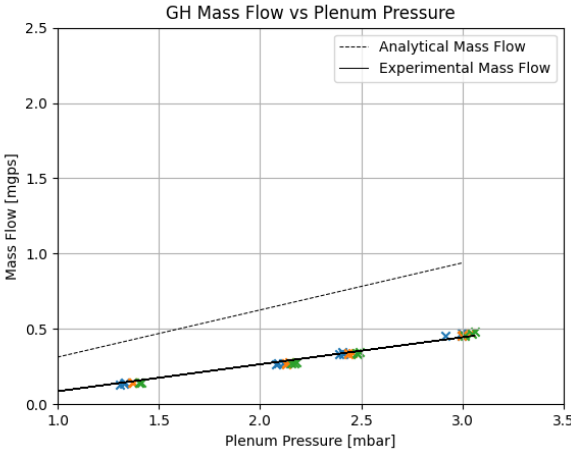

(c) GH propellant mass flow.

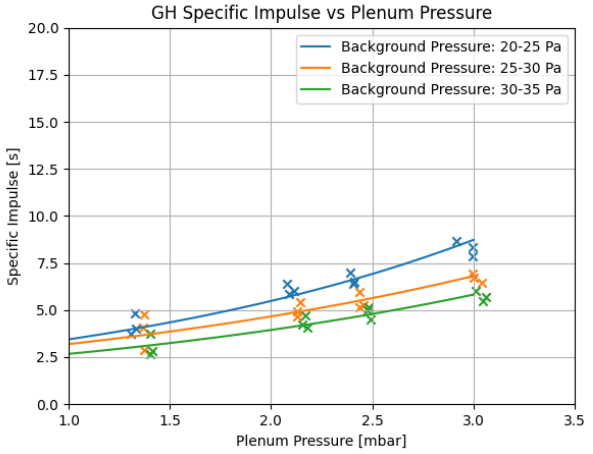

(d) GH specific impulse.

Figure 6.9: Experimental results for the mass flow and specific impulse of the GSS and the GH chips as a function of their plenum pressure. Note that the analytical result for the specific impulse is not plotted, as this is a constant, independent of the plenum pressure and type of chip, as shown by Equation (2.25).

6.3.2. Overview of Test Uncertainties

There are several sources of systematic errors that were taken into account when calculating the results presented above. In terms of the thrust results, calculated using Equation (6.3), the only error that was missing quantification was the one arising from the calculation of the change in displacement. The accuracy of the CS2 displacement sensor, when connected to the DT6220 demodulator, is 5.02 µm (Makhan, 2018). This value was included as the error for every displacement data point obtained from the sensor. Since average displacements were used to calculate the change in displacement caused by the thruster, the uncertainty of the average was also calculated. This was done using the same method as in Chapter 5: the square root of the sum of the errors squared, divided by the number of samples, Equation (5.1). Using this procedure, the uncertainty is expected to differ between thrust values arising from different plenum pressures, because the number of samples used to calculate them differs from case to case, as the time it takes to reach the 5 Pa background pressure threshold is also different for

each plenum pressure.

The experimental mass flow was calculated as the product of the transmission coefficient, from Equation (2.6), and the data from the Brooks 5850S mass flow controller. No manual could be found for this specific piece of equipment, however previous students note its accuracy as 0.7% of the measured mass flow value (Bijster, 2014)(Hutten, 2021). This value leads to errors in the calculated mass flow values that are at most two orders of magnitude lower than the nominal value, and are hence considered to be negligible.

Finally, two uncertainties related to the pressure were also taken into account: the background and the plenum pressures. The background pressure was measured by the Vacuubrand VSP 3000 pressure sensor, which has a listed error of 15% for pressures below 1000 Pa (VACUUBRAND, 2018). To put this error into perspective, 15% of 30 Pa is 4.5 Pa, almost the same as the threshold value chosen during the tests. This error sheds more light into why some thrust points shown in Figures 6.6 and 6.7 are closer to the curves of their neighbouring background pressure ranges. Last but not least, the HCLA12X5DU sensor used to measure the plenum pressure has an accuracy of 0.016 mbar (i.e. 1.6 Pa) (Guerrieri, Silva, Zeijl, et al., 2017). A summary of all errors discussed above is given in Table 6.4 below.

Table 6.4: Overview of sources of uncertainty in the propulsion characterisation results.

Sensor Name	**Parameter**	**Error**
CS2/DT6220	d	5.02 µm
Brooks 5850S	$\dot{m}$	0.7 %
VSP 3000	p_c	15 %
HCLA12X5DU	p_p	0.016 mbar

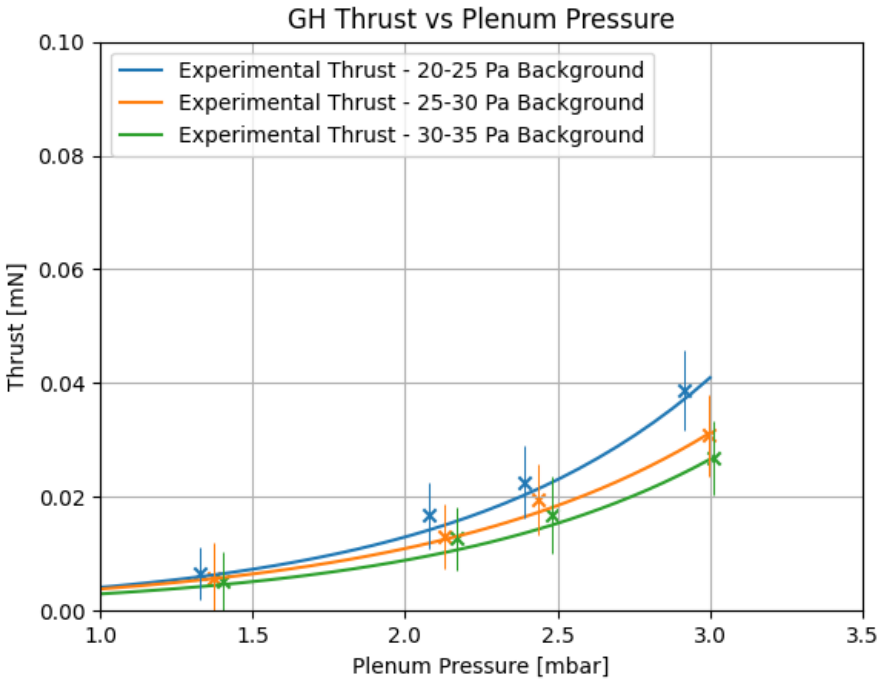

Figure 6.10: Thrust results including error bars for the GH chip. Note that only one of the test campaigns is shown, for visualisation purposes

An example thrust plot including the error bars for the GH chip, is given by Figure 6.10. The error related to the plenum pressure is also present in the plot, however it is too small to be discerned, and hence assumed to be negligible. The same can be said for the mass flow as the errors were calculated to be three significant figures smaller than their actual value. It can be observed that the error increases with increasing plenum pressure, which, by analysing Equation (5.1), is to be predicted. Let i be a tested plenum pressure, and $i+1$ be the subsequent tested pressure. Working out the ratio of errors $\frac{e_{i+1}}{e_i}$ leads to a factor of $\frac{\sqrt{N_i}}{\sqrt{N_{i+1}}}$, where N is the number of samples used to calculate the thrust values. As mentioned many times before, as the plenum pressure increases so does the mass flow, leading to a decrease in the time it takes for the 5 Pa threshold to be met, and hence a decrease in the number of samples used to calculate thrust. In other words, the number of samples used for a certain plenum pressure will always be larger than that of the next tested pressure (i.e. $N_i > N_{i+1}$), and hence the ratio of errors will always be larger than 1. Following the same line of thought, the errors of the thrust values of the GSS chip for the similar plenum pressures that were tested are larger than that of the GH chip, as the mass flow is also greater for each pressure. Please note that this conclusion can be made simply based on the systematic equipment errors present in the tests. If human and random errors are also taken into account, due to, for example, the visual selection of the peak displacements or environmental factors affecting the pendulum oscillations, it is expected that the total error will be larger for the lower plenum pressures instead. The final thrust results, including their systematic error, for the first test campaign of both chips are presented in Tables 6.5 and 6.6.

Table 6.5: Thrust results for the first test campaign with the GH chip.

GH Chip		
Background Pressure [Pa]	**Plenum Pressure [Pa]**	**Thrust [mN]**
20-25	133	0.0066 ± 0.0045
	208	0.0168 ± 0.0058
	239	0.0226 ± 0.0064
	292	0.0387 ± 0.0070
25-30	137	0.0059 ± 0.006
	213	0.0130 ± 0.0056
	244	0.0195 ± 0.0063
	299	0.0309 ± 0.0072
30-35	140	0.0052 ± 0.0050
	217	0.0127 ± 0.0055
	248	0.0168 ± 0.0065
	301	0.0268 ± 0.0067

Table 6.6: Thrust results for the first test campaign with the GSS chip.

GSS Chip		
Background Pressure [Pa]	**Plenum Pressure [Pa]**	**Thrust [mN]**
20-25	149	0.0284 ± 0.0104
	197	0.0794 ± 0.0084
	241	0.1750 ± 0.0106
	281	0.3172 ± 0.0125
25-30	152	0.0239 ± 0.0062
	199	0.0713 ± 0.0071
	243	0.1515 ± 0.0078
	284	0.3091 ± 0.0096
30-35	153	0.0204 ± 0.0097
	202	0.0655 ± 0.0099
	246	0.1449 ± 0.0099
	290	0.3018 ± 0.0104

6.3.3. Comparison with Analytical Model and Literature

It is clear by looking at the results that the analytical model created by Guerrieri, Silva, Zeijl, et al. (2017) highly overestimated the thrust produced by the GSS and, to a much larger extent, the GH chips. It must of course be mentioned that this model was essentially derived for the resistojet working conditions of the chips, under several assumptions regarding enthalpy changes and heat transfers from the chip to the propellant gas. Its ability to estimate the thruster's performance under cold gas conditions was therefore always in question. The

model does assume vacuum conditions, however this reason alone is not nearly enough to account for the differences seen in Figures 6.6 and 6.7. Another possible reason could be that some tests were actually performed under slip-flow conditions, rather than the transitional flow conditions assumed by the model. However, using Equation (2.1) and the results from the mechanical characterisation of the chips, it was proved that all tests were indeed performed under the transitional flow regime (i.e. $0.19 < Kn < 0.57$ for the GSS tests, and $0.22 < Kn < 0.66$ for the GH tests). Defining the model efficiency as the experimental thrust divided by the analytical thrust, a range of around 3-44 % is observed for the GSS, and 3-8 % for the GH chip. These efficiencies will logically increase if tests are performed under a total vacuum and the experiment errors are taken into account. They also show that, for higher plenum pressures, the model better approximates the experimental results. This was expected as the pendulum displacement method of calculating thrust is more reliable for larger displacements as, even though the systematic error increases with pressure, it is predicted that the overall error (i.e. including the random error) is larger for smaller pressures. Furthermore, FMMR literature shows linear relationships between thrust and mass flow/plenum pressure from similar experiments (Ketsdever, Lee, & Lilly, 2005)(Palmer et al., 2013), as predicted by the analytical model. However, both test campaigns on the LPM performed at the TU Delft, in this work and in that of Guerrieri, Silva, Zeijl, et al. (2017), present exponential relationships, the cause of which is also attributed to the test bench used. By looking at Figure 6.11, the same trends as described in the results analysis above can be observed: the thrust increases with plenum pressure and decreases with increasing background pressure. Please note that these tests were carried out using a LPM chip version that has since been discontinued, and hence the actual values should be taken lightly, unlike the trends observed.

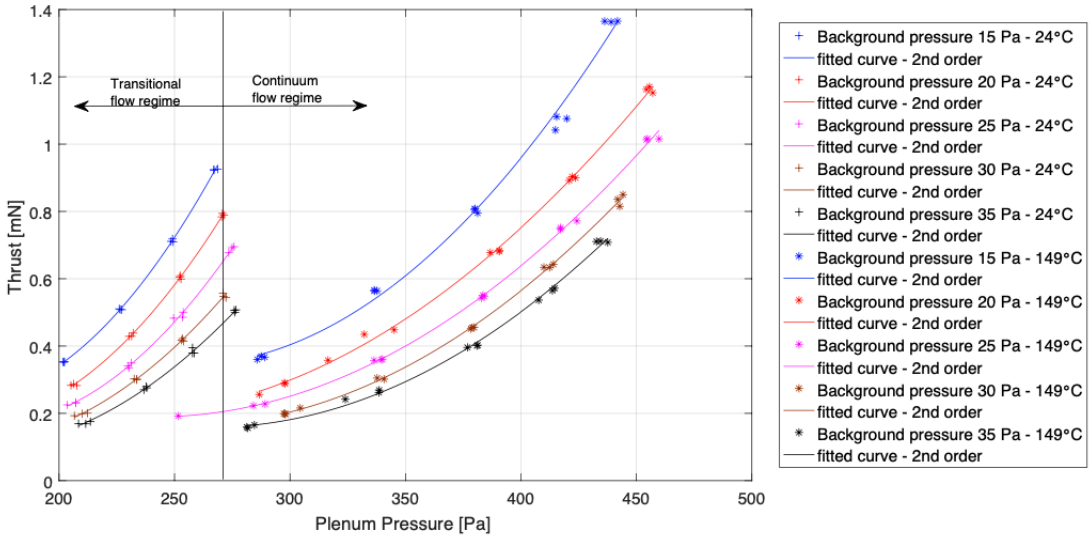

Figure 6.11: Thrust results obtained by Guerrieri, Silva, Zeijl, et al. (2017). Please note that, since the data set was not made available, a screenshot had to be taken, rather than remaking the plot with the style seen throughout the rest of the report.

On the other hand, the model is much more accurate at estimating the propellant mass flows. The model efficiencies for the GSS and the GH range from 43-85 % and 28-47 %, respectively. The same trend is observed as for the thrust in terms of the model being better at approximating

the experimental values obtained from the GSS chip. This can also be seen in terms of the slope of the experimental and analytical lines. For the GSS, the slopes are essentially the same, leading one to believe that the difference in results, which seems to be due to a constant factor, is more likely to be caused by how the mass flow rate was measured, rather than assuming the model is incorrect. For example, the Brooks 5850S mass flow sensor has not been calibrated in recent years. There was no time available to re-do the calibration, but this is certainly something that should be revisited by future students. Finally, the specific impulse was already expected to be much lower than predicted, as it is directly calculated from the thrust and mass flow. This was proven upon plotting the curves, as the analytical model predicts a constant I_{sp}, independent of the plenum pressure, of 53 s, which clearly isn't the case in the experimental results shown. Regrettably, no other source of experimental data is available regarding thruster chips such as the GSS and the GH to further validate any of the test results.

Finally, it is worth comparing the resulting performance of the LPM chips acting as cold gas thrusters with other, already established off-the-shelf (OTS) systems. The database of micropropulsion cold gas systems compiled by Cervone (2022) is used for this. A useful metric when it comes to comparing miniature propulsion systems is their thrust to mass ratio mN/g. It is clear that, in terms of this performance indicator, the LPM chips perform better than most of the examples shown in Table 6.7. Nevertheless, the most widely used value to compare such thrusters is the specific impulse. As shown in the table, the LPM thrusters clearly underperform in this aspect. This final conclusion means that using the LPM thruster as a cold gas, at least with its current design and chosen propellant, presents no clear advantage when compared to its OTS counterparts.

Table 6.7: Comparison between the performance of LPM chips and well-established OTS cold gas systems. (Cervone, 2022)

Company	Name	Isp [s]	Thrust-Mass Ratio [mN/g]
GOM Space	MEMS Cold Gas	50	0.003
GOM Space	NanoProp 6U	60	0.001
VACCO	MEPSI MiPS	65	0.116
VACCO	Palomar MiPS	50.1	0.039
Aerospace Co.	MEPSI	30	0.001
NanoSpace	CubeProp	75	0.001
TU Delft	**LPM-GSS**	20.2	0.052
TU Delft	**LPM-GH**	8.5	0.007

6.4. Post-testing Inventory

Upon completing all the tests planned in Chapter 4, several thruster chips remain inside the thesis box, labelled with the author's name, inside the SpE workshop. The LPM interface designed in Chapter 3, as well as all the required fluidic connections to perform both the cold and the resistojet testing are also present in the box.

Regarding the first fabricated wafers, those containing the offset described in Subsection 5.1.1, 2 chips with a stable glued electrical connection and another 2 that are wire bonded to PCBs are still available. The offset present in these wafers means that these should solely be used for mechanical and electrical characterisation purposes. They can of course also be used for thrust testing, however the decrease in exit area due to the offset shall be taken into account.

As mentioned in Subsection 5.1.1, one wafer of each type of chip has been fabricated at the time this report was written. Over 20 chips of each type remain in these wafers to be used for all sorts of testing. For resistojet testing, there are currently 2 chips, one of each type, that have been glued and have a stable electrical connection. Four more glued chips were delivered by the EKL, however it was noticed that some pins were not in proper contact with the thruster chips, and hence must be revisited. These all belong to the second wafer of each chip type, and are perfect in terms of size and position.

6.5. Conclusions

Based on the fourth and final research sub-question, the propulsion characteristics of the new LPM chips were explored in this chapter. The initial research plan regarding propulsion testing was clearly too extensive for the duration of this thesis, and the delays regarding chip manufacturing certainly did not help. Regrettably, there was no time to perform the resistojet tests, as well as the water vapour tests, and hence the research objective cannot be said to have been completely fulfilled. However, several cold thrust tests using nitrogen gas as propellant were performed on both chips, paving the way for further development of the LPM thruster within the TU Delft.

Three calibration procedures related to the chosen test bench, the AE-TB-5m were performed at the start of this characterisation campaign. First, a force conversion factor λ was found, which translates the force calculated at the location of the displacement sensor with that of the point in which the thruster is located. A value of 0.612 ± 0.001 was found. Secondly, to calibrate the displacement sensor itself (i.e. to find a relationship between displacement and force), a source that provided a known force was required. A Variable Turn Density Coil (VTDC) was hence calibrated as well to understand the force it generates as a function of the applied current. The resulting force-current relation was found to be 0.8134 ± 0.0002 mN/A, which lead to a value for the displacement sensor sensitivity of 0.03912 ± 0.0006 mN/µm. The thrust generated by the chips could now be calculated as $F_{thr} = (0.03912 \pm 0.0006) \cdot (0.612 \pm 0.001) \cdot \Delta d$, where Δd is the change in displacement caused by the chips. Lastly, as a final preparatory test before the cold gas test campaign, the ability of the PWM actuation of the used solenoid valve to produce stable plenum pressures was investigated. An initial setup was tried at first which completely failed at producing anything close to stable in terms of pressure, however a slight change in the tubing setup lead to the desired results. Due to differing transmission coefficients and hence mass flows between the two types of chip, different duty cycles were concluded to lead to the desired plenum pressures for testing. For a supply gas pressure of 1.2 bar, in terms of the GSS chip, for a range of plenum pressures of 100 to 300 Pa, the duty cycles tested were 10%, 18%, 30%, 40% and 50%. On the other hand, the duty cycles used for the GH chip were 4%, 9%, 14%, 20% and 25%.

Finally, the cold gas tests were performed. Due to the small size of the available vacuum

chamber and hence its inability to keep a constant background pressure during the thrust tests, three background pressure ranges were tested for each chip: 20-25 Pa, 25-30 Pa and 30-35 Pa. For each background pressure range, three test campaigns were performed, each at the five different plenum pressures resulting from the valve duty cycles described above. This was done for both types of chip, leading to a grand total of 90 test points to be analysed. The three tests at each pressure range were performed using different pendulum equilibrium distances, to show the repeatability of the results and to prove that this equilibrium distance has little to no effect on the thrust values. For both chips, all resulting trends were in line with the theory: the GSS provides more thrust than the GH for a given plenum pressure and hence mass flow, the thrust increases with plenum pressure and decreases with background pressure, and the mass flow and plenum pressure are positively and directly proportional. Thrust and I_{sp} values of up to 0.37 mN and 20 s were found for the GSS chip, and 0.04 mN and 9 s for the GH chip. Furthermore, it was found that the analytical model created by Guerrieri, Silva, Zeijl, et al. (2017) had a hard time predicting the performance of both chips in terms of their thrust (a maximum model efficiency of 44 % for the GSS and 8 % for the GH), however did a much better job in terms of mass flows, with minimum model efficiencies of 43 % and 28 %, respectively. To conclude, it was proven that the LPM chips, with a thrust to mass ratio of 0.052 for the GSS and 0.007 for the GH, are very competitive, if not better, than most of their industry counterparts in terms of one of the most commonly used comparative metric.

Regrettably, there was no time to perform the resistojet testing on the chips. This should be the first step in future research. To further approximate operational conditions, it is recommended to perform the thrust tests again under lower background temperatures as well. If possible, a larger vacuum chamber should be used to ensure a constant background temperature and more representative thrust results. This way, the force compensation method of measuring thrust can be used, which was proven to be more accurate by Pappadimitriou (2021), as there are much less unwanted oscillations in the system. It would also be ideal to control the PWM that controls the solenoid valve via the Arduino board itself, not relying on the PC clock which generates less stable pulses, as concluded by Silvestrini (2017). In order to do this, a new code must be written and uploaded to the Arduino board itself. In case this can be done, the GSS and GH chips can be tested at the exact same plenum pressures, which is always better if the objective is to compare the two. Last but not least, the Brooks 5850S mass flow sensor should be calibrated again, as this is assumed to be one of the main reasons for the difference between the experimental and analytical results obtained.

7

Conclusion & Recommendations

As a means to advance the development of the MEMS-based micro-resistojet satellite thruster designed by the TU Delft, this nine-month thesis project was started with an extensive literature study which concluded with the definition of the following research objective:

"*To characterise the newest version of the TU Delft LPM in terms of its mechanical, electrical, and propulsive performance by developing an appropriate thruster interface and performing the necessary testing efforts.*"

To aid in the completion of the aforementioned research goal, a total of four research questions were posed which shall be answered in this conclusion.

1. *How can a suitable interface be designed to aid in the propulsive characterisation of the LPM and to be used in the Delfi-PQ flight demonstration?*

Logically, the first step towards manufacturing the thruster interface was to generate a set of requirements. These requirements, ranging from the required physical dimensions to the type of fluidic and electrical connections, were of course generated while keeping in mind the desired application of the LPM thrusters: to provide a certain amount of thrust while minimising mass and power consumption to comply with the strict requirements set by the target satellites (i.e. Delfi-PQ and similar). Upon generating several CAD models and 3D printed prototypes, the TU Delft's DEMO workshop was contacted for the fabrication of the new thruster interface, made out of Teflon. This new interface is slightly larger than its required dimensions due to the fact that Teflon resists most types of glue and hence screws were added, however the flight model is intended to be fabricated using other gluable materials, complying with the volume requirement of 20x20x10 mm^3. The interface also includes an updated electrical connection with respect to its previous version. Instead of a 2-pin header simply touching the chip's contact pads, a 4-pin header design was introduced, glued to the chips using a conductive epoxy adhesive. Overall, this design update provides a sturdier electrical connection and allows for Kelvin resistance measurements, improving the future temperature control of the chip by allowing for more accurate live resistance measurements. The new interface, along with the Aluminium interface fabricated for connection with the chosen test bench, is seen in Figure 7.1.

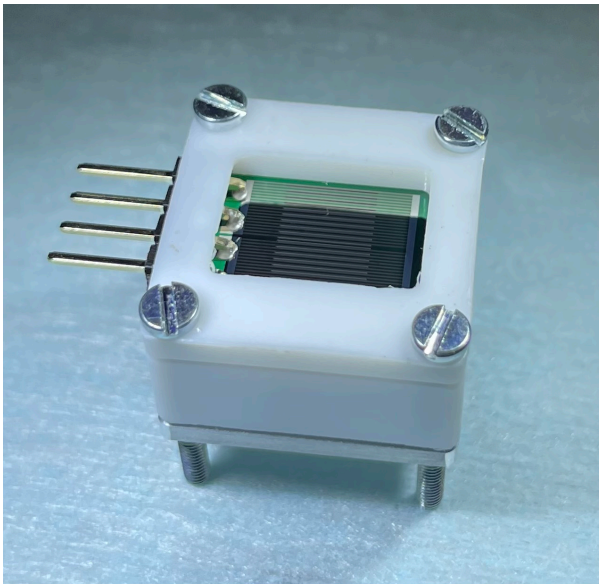

Figure 7.1: New LPM interface including a chip with the updated electrical connection.

2. *How accurately have the new LPM chips been manufactured?*

A more cost-effective process flow was introduced by Dr. Henk van Zeijl, the responsible scientist at the Else Kooi Laboratory in charge of fabricating the LPM chips. The material of the resistance lines was changed to Titanium, and spacing between them was decreased in such a way that one of the three types of chip could no longer be manufactured. A total of 10 wafers were paid for by the SpE department, which were divided into 5 wafers of the GSS chip, and 5 of the GH chip. The resistance design was common for the two types of chip: 2 sets in series of 19 resistances arranged in parallel, each resistance with a width of 120 µm, length of 11 mm, and thickness of 500 nm, arriving at a design resistance of 9.3 Ω. The GSS chips were designed with a slot length of 6.28 mm and width of 120 µm, where as the GH chip holes had a design diameter of 100 µm. Upon examining the fabricated chips using a laser scanning confocal microscope, different values were found for each type of chip. In terms of the GSS, the resistance lines were measured to have an average width of 123.9 $\pm$ 1.54 µm, a length of 10982 $\pm$ 0.11 µm and a height of 568 $\pm$ 0.2 nm. The slots were measured to be 6585 $\pm$ 0.18 µm long and 115 $\pm$ 1.23 µm wide. On the other hand, the resistance lines of the GH chip averaged 123 $\pm$ 2.31 µm wide, 10984 $\pm$ 0.11 µm long and 558 $\pm$ 0.2 nm high. The holes were measured to have an average diameter of 102 $\pm$ 2.89 µm. To conclude, the actual fabrication resistances of the GSS and GH chips were calculated to be 7.93 $\pm$ 0.1 Ω and 8.07 $\pm$ 0.15 Ω, respectively, meaning a 14.5 % and a 12.8 % decrease. In terms of the exit areas, values of 15.16 $\pm$ 1.6 mm^2 and 13 $\pm$ 7 mm^2 were calculated for the GSS and GH chips, a 0.5 % and 3.4 % increase, respectively.

3. *How have the changes made to the LPMs fabrication procedure affected its electrical characteristics?*

Two tests were performed to assess the electrical characteristics of the newly fabricated chips: the room temperature resistance measurement, and the temperature coefficient of resistance (TCR). The room temperature resistance was measured using the 2-pin electrical connection used in the previous version of the LPM interface, as well as using the Kelvin method to anal-

yse its effect. The 2-pin resistance measurements arrived at 15.898 $\pm$ 0.02 Ω and 14.664 $\pm$ 0.7 Ω for the GSS and GH chips. When using the Kelvin method, the values found were 11.959 $\pm$ 0.05 Ω and 12.135 $\pm$ 0.1 Ω, respectively. This difference in results, which can certainly not be overlooked, proved that updating the electrical connection was a good idea, specially since the resistance of the chip shall be measured as accurately as possible for it to also serve its intended secondary purpose, to act as a temperature sensor. This fulfil this secondary goal, the TCR was calculated experimentally by providing an increasing current to the chips, and measuring their resistance and temperature. The resulting TCR values were 0.00464 $\pm$ 2.5 $\cdot$ 10^{-4} °C^{-1} and 0.00438 $\pm$ 1.6 $\cdot$ 10^{-4} °C^{-1} for the GSS and GH chips. As expected, the calculated TCR was similar for the two different types. Problems were encountered while plotting the power/temperature relationship of the GSS chip, as the conductive glue properties was assumed to have changed with respect of the GH chip, and hence these tests are recommended to be repeated. The calculated chip temperature using the experimentally found TCR was plotted against the measured temperature using several thermocouples, as shown in Figure 7.2, and the GH chip was hence concluded to be calibrated as a temperature sensor for a range of 40-140 °C.

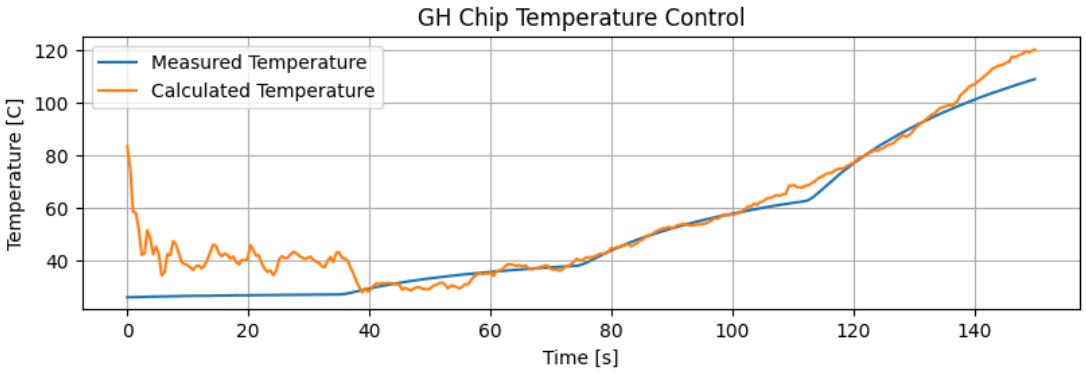

Figure 7.2: Calculated temperature using the TCR versus the measured chip temperature using thermocouples.

4. *How have the changes made to the LPMs fabrication procedure affected its propulsion capabilities in near-operational conditions?*

The thrust generated by the two LPM chips, operating as cold gas thrusters, was measured using the AE-TB-5m pendulum test bench available at the TU Delft. This test setup calculates thrust as a function of three variables: a force conversion factor λ, a displacement sensor sensitivity S_d, and a change in displacement Δd caused by the thruster. The first two were found by performing several calibration procedures to equal 0.612 $\pm$ 0.013 and 0.03912 $\pm$ 0.0006 mN/µm. The thrust tests were performed using nitrogen gas as propellant in near operational conditions: inside a vacuum chamber with three background pressure ranges, 20-25 Pa, 25-30 Pa and 30-35 Pa. The pressure inside the LPM plenum was varied from 100-300 Pa by means of a PWM controlled solenoid valve. A thrust range of 0.002-0.039 mN was found for the GH chip, with mass flow values ranging from 0.07-0.47 mgps, and 0.005-0.37 mN for the GSS chip, with mass flows of 0.27-1.96 mgps. It was found that the analytical model described at the beginning of this report has a hard time predicting the thrust performance of both chips, however it approximates the mass flow values observed to an acceptable extent. Furthermore, most results followed the expected trends: the thrust increased with increasing

plenum pressure and decreased with increasing background pressure, the mass flow increased with increasing plenum pressure, and the GSS provided more thrust than the GH for the same pressures and mass flows. The resulting thrust curves for both chips were the following:

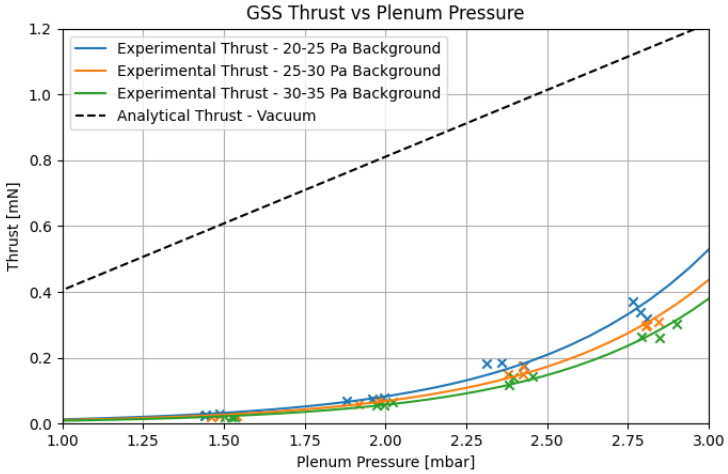

(a) Thrust results for the GSS chip.

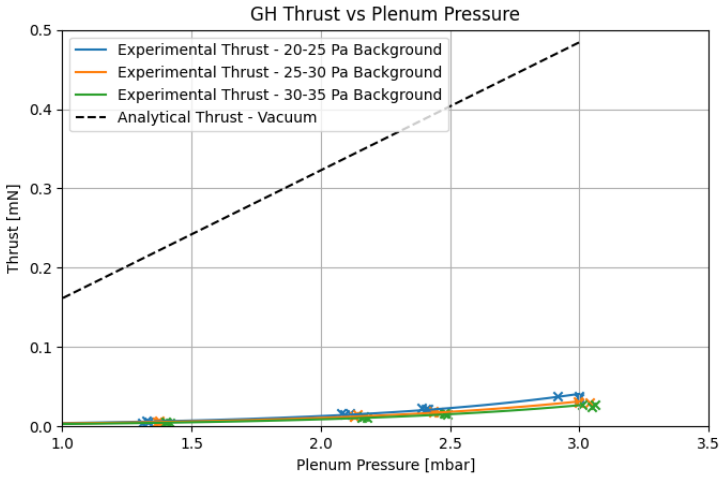

(b) Thrust results for the GH chip.

Figure 7.3: Experimental results for the thrust of the GSS chip as a function of its plenum pressure. Results of the analytical model described in Chapter 2 are shown for reference. Note the difference in the vertical axis scale.

7.1. Recommendations for Future Research

Several recommendations can be given to students and researchers aiming to further advance the design of the TU Delft's LPM thrusters. First and foremost, it is worth mentioning that, once production is complete, three more chip wafers of each type will be available do use, each containing 26 thruster chips, leaving plenty of thrusters to perform all sorts of tests on.

In terms of the electrical design of the thruster chips, various areas for improvement are identified. The first step should be to revisit the electrical connections of the LPM chips, as the

current connection highly depends on the type of conductive glue used and its curing schedule. In terms of electrical robustness, the PCB option would be best, however this can require a trade-off regarding the interface's overall volume. Furthermore, it would be good to perform the TCR tests again, using a more accurate method of measuring temperature. For example, the emissivity of the chip could be changed by means of a certain type of ink, allowing its temperature to be more accurately measured using an IR camera, or the chip could be placed on a hotplate or in an industrial oven while having its resistance measured at certain temperature intervals. Both these options would ensure more representative chip temperature measurements when compared to the three thermocouple process used in this report. Furthermore, an automatic control of the chip temperature should be implemented. Logically, this would be done by tuning a new PID to keep the temperature at the desired value by using the TCR to continuously calculate and adapt the chips temperature.

Regrettably, there was not enough time to perform the resistojet testing of the chips. The next logical step would be to indeed perform thrust tests with the chip connected to power. This would of course have to be done after creating the required temperature control PID mentioned above. Yes, the chip temperature could also be controlled by simply controlling the power provided to the chip by looking at Figure 5.6, however a properly tuned PID would definitely lead to more accurate control. The procedure, setup and equipment are already described in Subsection 4.2.7 and can be readily followed once the above recommendations have been applied. If possible, the thrust tests should be performed in a larger vacuum chamber in which the background pressure can be kept constant during the thrust firing, as well as under a lower background pressure, to further approximate operational conditions.

References

ASTM International. (2021). *Standard Test Method for Total Mass Loss and Collected Volatile Condensable Materials from Outgassing in a Vacuum Environment (ASTM E595-15)*. https://doi.org/10.1520/E0595-15R21

Bijster, R. J. F. (2014, January). *Design, Validation ad Verification of a Micropropulsion Thrust Stand* [Available at http://repository.tudelft.nl/].

Bird, G. A. (1963). Approach to Translational Equilibrium in a Rigid Sphere Gas. *The Physics of Fluids*, *6*(10), 1518–1519. https://doi.org/10.1063/1.1710976

Bird, G. A. (1994). *Molecular Gas Dynamics and the Direct Simulation of Gas Flows*. Clarendon Press - Oxford.

Cervone, A. (2022). AE4S07: Micro-Propulsion [Course Reader].

Cervone, A., Mancas, A., & Zandbergen, B. (2015). Conceptual design of a low-pressure micro-resistojet based on a sublimating solid propellant. *Acta Astronautica*, *108*, 30–39. https://doi.org/https://doi.org/10.1016/j.actaastro.2014.12.003

EKL. (2022). *Else Kooi Laboratory* [Accessed on 21-03-2024]. https://www.tudelft.nl/ewi/onderzoek/faciliteiten/else-kooi-lab

European Cooperation for Space Standardisation (ECSS). (2008). *Thermal vacuum outgassing test for the screening of space materials (ECSS-Q-ST-70-02C)*. https://ecss.nl/standard/ecss-q-st-70-02c-thermal-vacuum-outgassing-test-for-the-screening-of-space-materials/

Gad-el-Hak, M. (2002). Flow Physics. In M. Gad-el-Hak (Ed.), *The MEMS Handbook*. CRC Press LLC.

Giancoli, D. C. (2008). *Physics for Scientists Engineers with Modern Physics* (4th ed.). Pearson.

Guerrieri, D. C., Cervone, A., & Gill, E. (2016). Analysis of Nonisothermal Rarefied Gas Flow in Diverging Microchannels for Low- Pressure Microresistojets. *Journal of Heat Transfer*, *138*(11), 112403. https://doi.org/10.1115/1.4033955

Guerrieri, D. C., Silva, M. A. C., Cervone, A., & Gill, E. (2018a). Optimum Design of Low-Pressure Micro-Resistojet Applied to Nano- and Pico-Satellites. *In ESA Space Propulsion 2018 Conference, Seville, Spain*, Article SP2018_00108.

Guerrieri, D. C., Silva, M. A. C., Zeijl, H. V., Cervone, A., & Gill, E. (2017). Fabrication and characterization of low pressure micro-resistojets with integrated heater and temperature measurement. *Journal of Micromechanics and Microengineering*, *27*(12). https://doi.org/10.1088/1361-6439/aa90fb

Guerrieri, D. C., Silva, M. A., Cervone, A., & Gill, E. (2018b). An analytical model for characterizing the thrust performance of a Low-Pressure Micro-Resistojet. *Acta Astronautica*, *152*, 719–726. https://doi.org/https://doi.org/10.1016/j.actaastro.2018.09.008

Guerrieri, D., Silva, M. A. C., Cervone, A., & Gill, E. (2017). Selection and Characterization of Green Propellants for Micro-Resistojets. *Journal of Heat Transfer*, *139*(10), 102001. https://doi.org/10.1115/1.4036619

Guo, J. (2022). AE4S10: MicroSat Engineering. Lecture 1: Introduction [PowerPoint Slides].

Hutten, R. (2021, February). *Vaporizing Liquid Micro-resistojet experimentation* [Available at http://repository.tudelft.nl/].

Jansen, E. H. W. (2016, April). *Improvement and Validation of Test Stand Performance for Novel Micropropulsion Systems* [Available at http://repository.tudelft.nl/].

Ketsdever, A. D. (2002). Facility Effects on Performance Measurements of Micropropulsion Systems that Utilisze Gas Expansion. *Journal of Propulsion and Power*, *18*(4). https://doi.org/10.2514/2.6002

Ketsdever, A. D., Clabough, M. T., Gimelshein, S. F., & Alexeenko, A. (2005). Experimental and Numerical Determination of Micropropulsion Device Efficiencies at Low Reynolds Numbers. *AIAA Journal*, *43*(3). https://doi.org/10.2514/1.10284

Ketsdever, A. D., Lee, R. H., & Lilly, T. C. (2005). Performance testing of a microfabricated propulsion system for nanosatellite applications. *Journal of Micromechanics and Microengineering*, *15*(12), 2254. https://doi.org/10.1088/0960-1317/15/12/007

Ketsdever, A. D., Wadsworth, D., Vargo, S., & Muntz, E. (1998). The free molecule micro-resistojet - An interesting alternative to nozzle expansion. In *34th AIAA/ASME/SAE/ASEE Joint Propulsion Conference and Exhibit*. https://doi.org/10.2514/6.1998-3918

Keyence. (2015). *3D Laser Scanning Confocal Microscope* [Accessed on 22-08-2024]. https://sernia.ru/upload/pdf_files/VK-X250_X150_X120_C_611A29_GB_1035-1.pdf

Keysight. (2022). *34401A Digital Multimeter*. https://www.keysight.com/us/en/assets/7018-06774/data-sheets-archived/5968-0162.pdf

Lafferty, J. M. (1998). *Foundations of Vacuum Science and Technology*. Wiley.

Lide, D. R. (2004). *CRC Handbook of Chemistry and Physics* (85th ed.). CRC Press.

Loctite. (2014). *Technical Data Sheet Loctite Ablebond 84-1LMI*. https://datasheets.tdx.henkel.com/LOCTITE-ABLESTIK-84-1LMI-en_GL.pdf

Lurie Nanofabrication Faculty. (2020a). *Low-Pressure Chemical Vapor Deposition* [Accessed on 27-03-2024]. University of Michigan. https://lnf-wiki.eecs.umich.edu/wiki/Low_pressure_chemical_vapor_deposition

Lurie Nanofabrication Faculty. (2020b). *Plasma Enhanced Chemical Vapor Deposition* [Accessed on 27-03-2024]. University of Michigan. https://lnf-wiki.eecs.umich.edu/wiki/Plasma_enhanced_chemical_vapor_deposition

Lurie Nanofabrication Faculty. (2021). *Reactive Ion Etching* [Accessed on 27-03-2024]. University of Michigan. https://lnf-wiki.eecs.umich.edu/wiki/Reactive_ion_etching#Method_of_operation

Lurie Nanofabrication Faculty. (2023). *Sputter Deposition* [Accessed on 27-03-2024]. University of Michigan. https://lnf-wiki.eecs.umich.edu/wiki/Sputter_deposition

Lynn, T. W. (2002). *An Introduction to Experimental Uncertainties and Error Analysis for Physics 28*. Harvey Mudd College.

Makhan, R. (2018, December). *Performance of the MEMS Vapor- izing Liquid Microthruster using cold nitrogen gas as propellant - An experimental study* [Available at http://repository.tudelft.nl/].

Maxence, D., Guerrieri, D. C., & Cervone, A. (2017). Preliminary Results of a Sublimating Propellant Tank for Dedicated Micropropulsion System.

Melaika, A. (2019, July). *Design and Verification of DelfiPQ Satellite Propulsion Subsystem* [Available at http://repository.tudelft.nl/].

Mele, L., Santagata, F., Iervolino, E., Mihailovic, M., Rossi, T., Tran, A., Schellevis, H., Creemer, J., & Sarro, P. (2012). A molybdenum MEMS microhotplate for high-temperature

operation. *Sensors and Actuators A: Physical*, *188*(11), 173–180. https://doi.org/10.1016/j.sna.2011.11.023

Micro-Epsilon. (2015). *capaNCDT // Capacitive displacement sensors and systems* [Accessed on 19-09-2024]. https://www.micro-epsilon.com/fileadmin/download/products/cat--capaNCDT--en-us.pdf

Pallichadath, V. (2018). *Propulsion Subsystem Requirements for the Delfi-PQ Satellites* (tech. rep.). Delft University of Technology.

Palmer, K., Nguyen, H., & Thornell, G. (2013). Fabrication and evaluation of a free molecule micro-resistojet with thick silicon dioxide insulation and suspension. *Journal of Micromechanics and Microengineering*, *23*(6), 065006. https://doi.org/10.1088/0960-1317/23/6/065006

Pappadimitriou, A. (2021, March). *Performance Evaluation of a Vaporizing Liquid Microthruster Using Nitrogen and Water as Propellants* [Available at http://repository.tudelft.nl/].

PRIME Faraday Partnership. (2002). *An Introduction to MEMS (Micro-electromechanical Systems)*. Loughborough University. Loughborough, UK.

Silvestrini, S. (2017, July). *Closed-loop Thrust Magnitude Control System for Nano- and Pico-Satellite Applications* [Available at http://repository.tudelft.nl/].

Singh, S., Jejusaria, A., Singh, J., Vashishath, M., & Kumar, D. (2022). Comparative study of titanium, platinum, and titanium nitride thin films for micro-elecrto mechanical systems (MEMS) based micro-heaters. *AIP Advances*, *12*(9), 095202. https://doi.org/10.1063/6.0001892

Singh, S. I. (2023, November). *Design, Fabrication and Characterization of MEMS Micro-resistojet Thrusters* [Available at http://repository.tudelft.nl/].

Speretta, S., Soriano, T. P., Bouwmeester, J., Godínez, J. C., Menicucci, A., Watts, T., Sundaramoorthy, P., Guo, J., & Gill, E. (2016). Cubesats to pocketqubes: Opportunities and challenges. *In Proceedings of the 67th International Astronautical Congress (IAC): Guadalajara, Mexico*, Article IAC-16–B4.7.5_A IAF.

Sundqvist, B., & Tolpygo, V. (2018). Saturation and pressure effects on the resistivity of titanium and two ti-al alloys. *Journal of Physics and Chemistry of Solids*, *122*. https://doi.org/10.1016/j.jpcs.2018.05.046

TE Connectivity. (2021). *HCLA Series Miniature amplified low pressure sensors* [Available at https://www.farnell.com/datasheets/3926688.pdf?_gl=1*hg56zl*_gcl_au*MjEwNjk4OTMxOC4xNzI4MzgxNjU1].

Teflon PTFE Properties Handbook. (n.d.). Dupont.

Tew, J., Driessche, J. V. D., Lufty, F. M., Muntz, E. P., Wong, J., & Ketsdever, A. D. (2000). A Thrust Stand Designed for Performance Measurements of the Free Molecule Micro-Resistojet. *36th AIAA/ASME/SAE/ASEE Joint Propulsion Conference and Exhibit*. https://doi.org/10.2514/6.2000-3673

Turmaine, L. A. (2018, September). *A technology demonstration pay- load for micro-resistojet thrusters on Delfi-PQ* [Available at http://repository.tudelft.nl/].

VACUUBRAND. (2018). *Vacuum gauge Set DCP 3000 + VSP 3000*. https://www.%20vacuubrand.com/us/page936.html

Versteeg, H. S. E. (2020, May). *Novel Fabrication Method for a Hot-Gas Supersonic Microthruster* [Available at http://repository.tudelft.nl/].

Wagner, W., Saul, A., & Pruss, A. (1994). International Equations for the Pressure Along the Melting and Along the Sublimation Curve of Ordinary Water Substance. *Journal of*

Physical and Chemical Reference Data, *23*(3), 515–527. https://doi.org/10.1063/1.555947

A

Engineering Drawings

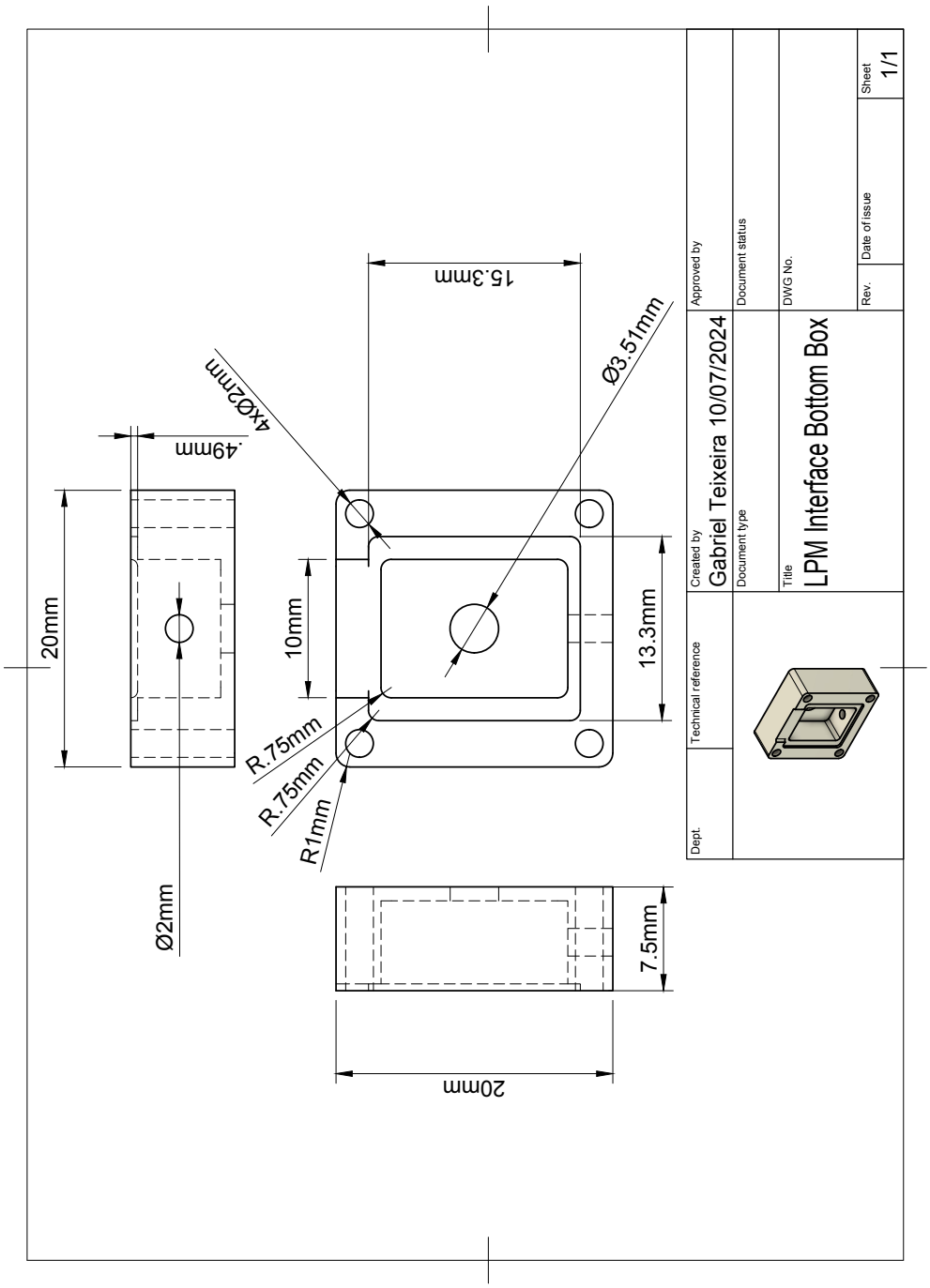

Figure A.1: Engineering drawing of the bottom box of the LPM interface.

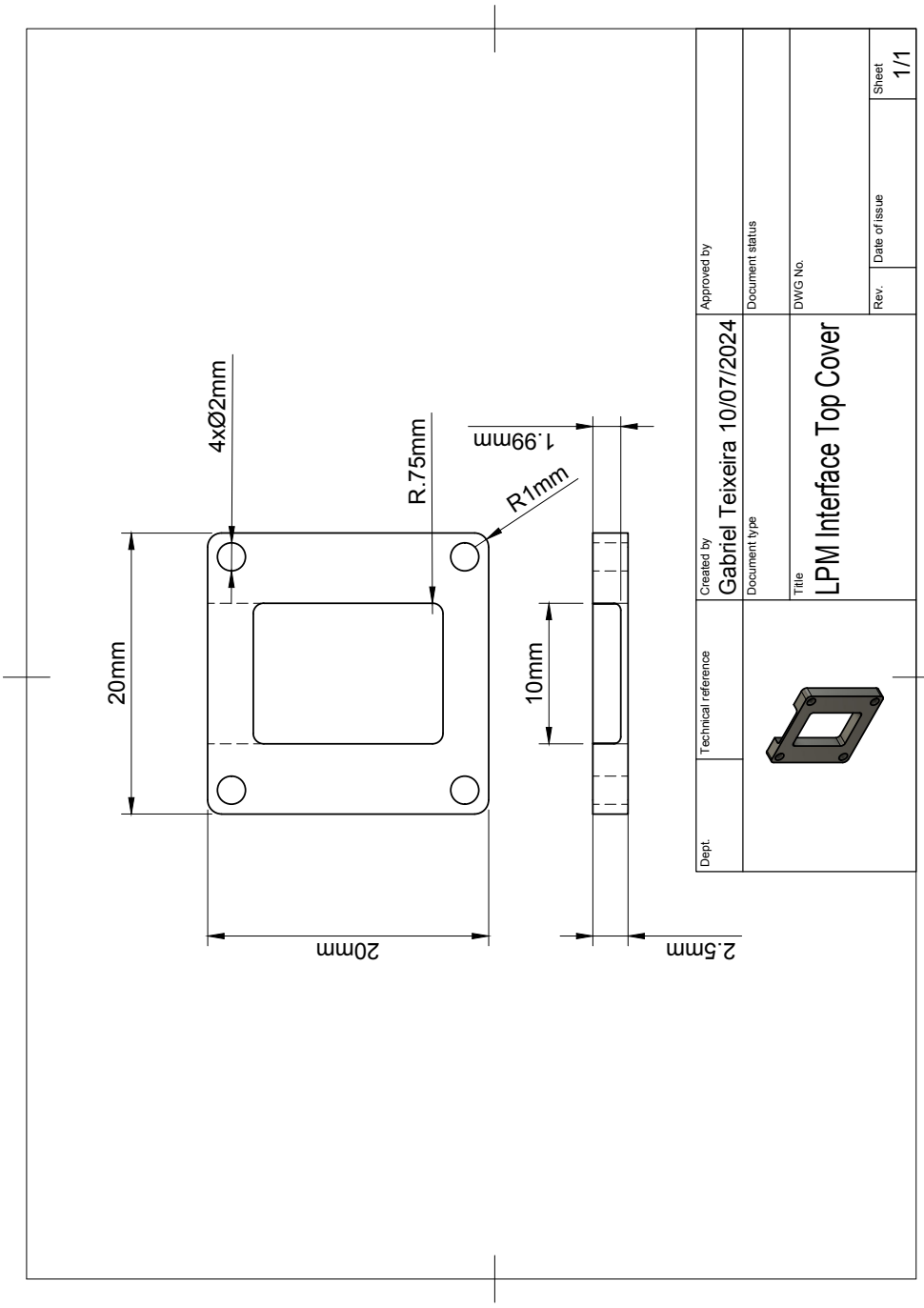

Figure A.2: Engineering drawing of the front cover of the LPM interface.

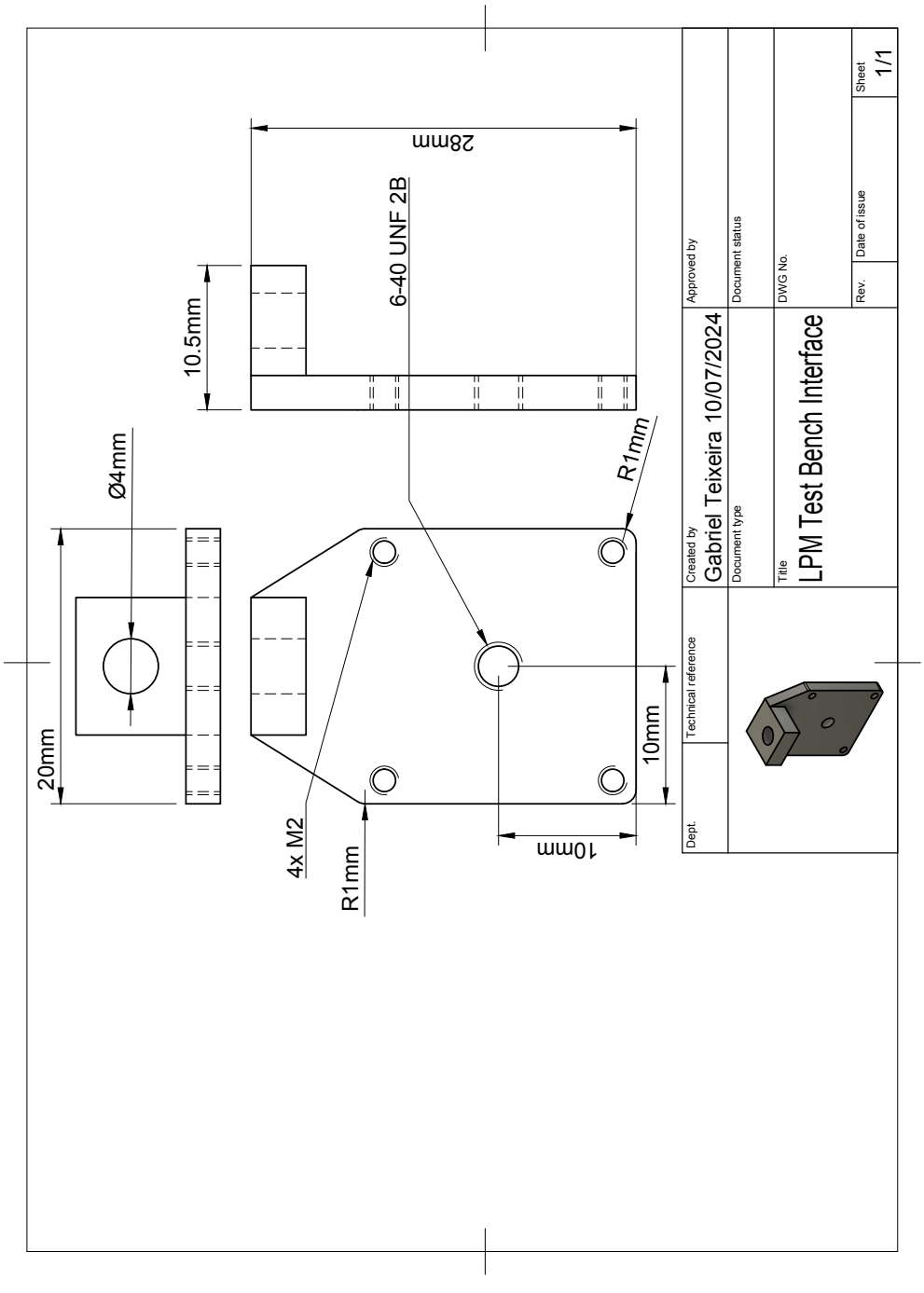

Figure A.3: Engineering drawing of the test bench interface.